Quantifying Wind Tunnel Effects on the Flying V

Antonio M. Jorge*
Delft University of Technology, Delft, 2629 HS, The Netherlands

This article presents an advanced wind tunnel correction method to be used on the Flying V in its experimental campaign in the Low Turbulence Wind Tunnel at TU Delft. Due to strong vortices formed over the leading edge of the Flying V, the classical method of images typically employed is not expected to accurately correct for wall and strut effects, potentially hampering the development of the aircraft. The proposed method involves comparing the Flying V's aerodynamic performance in wind tunnel; 1.8‰-scale, free-air; and full-scale, free-air conditions using RANS CFD. Simulations are conducted under sea-level conditions at an airspeed of 50 m/s. The wind tunnel model, mounted on a turntable, incorporates pivotal main struts and a circular aft strut. Sixteen equispaced combinations of angle of attack and sideslip are investigated between $[0°, 32°]$, and $[0°, 25°]$, respectively. Thin-plate splines are provided for data interpolation. The current procedure is validated using external experimental and numerical data from the F19 aircraft. The method was found to match the external data to an acceptable level of accuracy, with an RMSE in the lift coefficient of 0.111 relative to the experiment and 0.073 relative to the CFD data. Through integral force and moment polars, total pressure loss contours, surface pressure coefficients and surface streamlines, the investigation reveals a significant influence of walls on leading-edge vortices, causing premature vortex breakdown and lower stall angles in confined conditions compared to free-air scenarios. The full-scale model exhibits resilience against stall up to extreme angles of attack, emphasising the effect of the Reynolds number. The angle of sideslip profoundly affects the overall flow field, particularly the strength, coherence, and symmetry of leading-edge vortices. Classical corrections are identified as insufficient in capturing this nuanced behaviour. An improved thin-plate spline-based surrogate model for the corrections is presented using the current results.

Nomenclature

α = Angle of attack
$\bar{c}$ = Mean aerodynamic chord
β = Angle of sideslip
$\mathbf{a}$ = Vector of interpolation coefficients
$\mathbf{c}$ = Vector of interpolation centres
$\mathbf{x}$ = Attitude vector
μ_∞ = Freestream dynamic viscosity
Ψ = Radial basis function
ρ_∞ = Freestream density
b = Aircraft span
C_p = Pressure coefficient
$C_{[\,]}$ = Aerodynamic coefficient
D = Integral drag force
f = Thin-plate spline
L = Integral lift force
l = Integral rolling moment
m = Integral pitching moment
n = Integral yawing moment
p = Static pressure
S = Wing area
V_∞ = Freestream airspeed
Y = Integral sideforce
y^+ = Dimensionless wall distance

---

*MSc Student, Flight Performance and Propulsion Section, Faculty of Aerospace Engineering

I. Introduction

The Flying V is a novel aircraft configuration conceived at Airbus Future Projcts and actively being developed by TU Delft. By completely changing the aircraft architecture, the Flying V aims to provide a platform for significant efficiency gains, in contrast to conventional designs which have only seen improvements in the order of 3% a year over the past decade and a half[1]. Unlike traditional aircraft designs with a fuselage and separate wings, this effort integrates the wing and fuselage into a single structure. The Flying V also incorporates a crescent wing shape, seen in Fig. 1. By reducing fuel consumption and emissions, this innovative design could help to mitigate the impact of aviation on the environment, while also providing a more comfortable and efficient passenger experience [1]. As research on the Flying V progresses, the Faculty of Aerospace Engineering at TU Delft is preparing for an experimental campaign at the Low Turbulence Wind Tunnel (LTT). The data from this experiment will help refine the understanding of the aerodynamic performance of the aircraft, and elucidate the complex flow phenomena around the Flying V.

The presence of the wind tunnel walls and support struts may heavily influence the flow around the test article, leading to altered data measurements. The difference in results can vary greatly depending on the geometry of the test article and wind tunnel, as well as the testing conditions. To overcome this interference, comprehensive wind tunnel corrections have been developed which are successful in accounting for these effects over a large range of scenarios. Typically, the LTT employs the method of images for its corrections, which is not valid for the flow around the Flying V since it does not account for the influence of the dominant flow phenomenon at high angles of attack: leading edge vortices. In an effort to advance the accuracy of the corrections and simultaneously gain insights into the Flying V's aerodynamic behaviour, this investigation uses computational fluid dynamics (CFD) to identify the wind tunnel effects on the Flying V. Unlike the method of images, this approach should resolve the leading edge vortices which are formed over the suction side of the aircraft and account for their influence on the flow field.

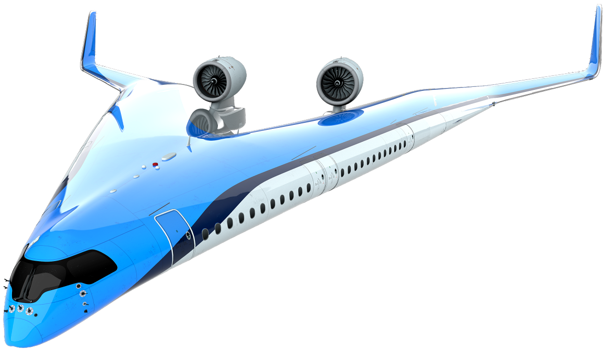

Figure 1. Artistic rendition of the Flying V

The article is structured as follows: in Section II, the numerical methodology is reported along with a description of both the test article and wind tunnel. In Section III, the overarching method is validated using experimental and numerical data from external investigations of the F19. In Section IV, the corrections are shown, alongside an interpretation which makes use of the integral forces, moments, and predicted flow field around the Flying V. These are compared against the classical method. Subsequently, the quality of the thin-plate spline interpolation is evaluated, and the surrogate correction model is introduced. Finally, in Section V, the conclusions are drawn, including limitations, recommendations, and future work. Supporting work can be found in Appendices A to K.

---

[1] `http://bit.ly/3MwSqu0`, accessed on 7 Nov. 2023

II. Methodology

To identify the wind tunnel effects, three scenarios are compared, namely: the wind tunnel scenario, including walls and struts; the sub-scale, free-air scenario, where the aircraft features the same 1.8%-scale as the wind tunnel model; and finally the full-scale, free-air scenario. This arrangement allows for an independent comparison of the effect of the walls and struts, and the effect of increasing the Reynolds number by a factor of 54. Reynolds-Averaged Navier-Stokes (RANS) simulations are used to calculate the flow field around the Flying V. Integral forces and moments are presented for a range of angles of attack, α, between 0° and 32° in increments of 10.66°, and a range of angles of sideslip, β, between 0° and 25° in increments of 8.33°, both at a chord-based Reynolds number of 1.16×10^6 and 62.7×10^6. Due to the limited number of runs, thin-plate spline interpolation is applied to increase the resolution of the force and moment data.

A. Model Description

The current iteration of the Flying V geometry stands as the most recent update, aggregating developments in aerodynamics, structures, flight dynamics and even interior design. Changes at this step of the design process are expected but should not lead to any large changes in the performance of the aircraft - it can be assumed that analyses of this iteration will capture the effects of the walls, struts and Reynolds number accurately, even for future design revisions. Thus, the full-scale geometry illustrated in Fig. 2, should be representative of the final test article. In Fig. 2b, the main and aft struts are visible. The mean aerodynamic chord ($\bar{c}$) of the Flying V is referenced from previous investigations and measures 18.3 m [2]. All moments are calculated about the model's centre of volume, indicated as the moment reference point (MRP) in Fig. 2a.

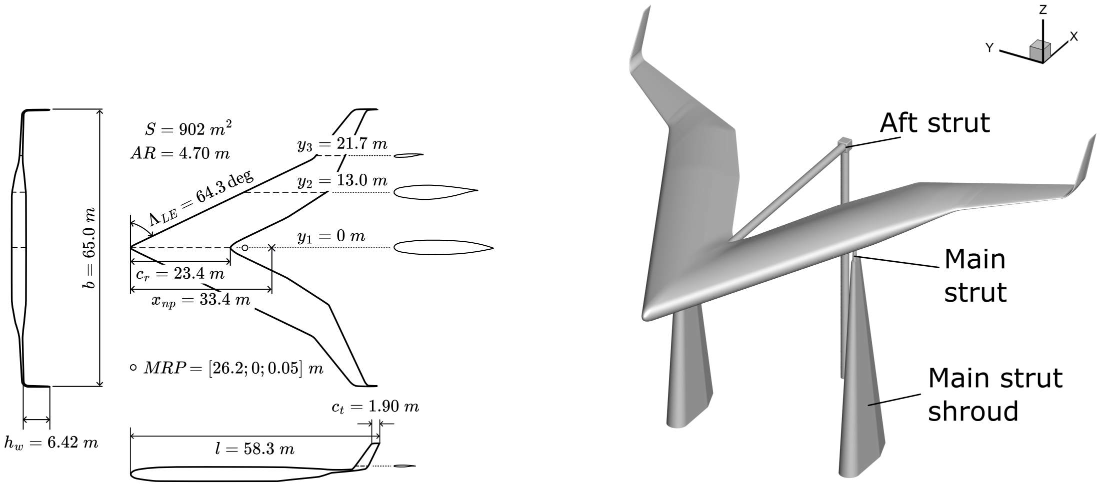

(a) Schematic view including dimensions

(b) Isometric view including support struts

Figure 2. Geometry of the Flying V

The main struts are reused from previous LTT experiments, with the tapered shroud extended upwards such that there is a clearance of around 5 cm between them and the aircraft to minimise interference on the balance measurements. These are fixed on the aircraft 23.2 cm outboard of the root, and 58.5 cm aft of the nose - slightly ahead of the aircraft's neutral point (x_{np}), calculated by Laar [3], to ensure that the assembly is stable. Two cylindrical rods of 2 cm diameter comprise the aft rod which serve to pitch the aircraft. Their circular cross-section is intended to minimise the frontal area, and hence sideforce under the sideslip, at the cost of increased vortex-shedding. The fork joint between the vertical and horizontal members of the aft strut is modelled as a cube with rounded corners of 2.5 cm radius. The horizontal member of the aft strut is rigidly connected to the aircraft at the trailing edge of the root. Future developments of the Flying V geometry are expected to feature a small tail at this location which forms a natural connection point for a strut. While it may not be ideal for this iteration of the Flying V, the struts are configured for the most likely design at the time of the experiment.

Lastly, the LTT geometry is taken from existing sources [4] and is summarised in Fig. 3a. This atmospheric, closed-throat, single-return type tunnel features an octagonal test section measuring 1.80 m wide, 1.25 m tall, and 2.60 m long. For RANS simulations, it is known that both the inlet and outlet should be placed at a significant distance from the aerodynamic body, typically at least ten body lengths from the outlet, and slightly less from the inlet [5]. Using the test section as the domain breaks this convention and would very likely introduce inaccuracies or artefacts into the solution. In order to obtain a sufficiently long domain, both the contraction chamber and diffuser are included, as seen in Fig. 3b. The LTT's test section is slightly diverging, such that the area in the throat excluding the boundary layer is constant along its length. This taper is carefully designed to ensure that no buoyancy corrections are needed. In the numerical simulations, the walls are treated as inviscid and the test section walls can be made parallel to emulate this behaviour [6].

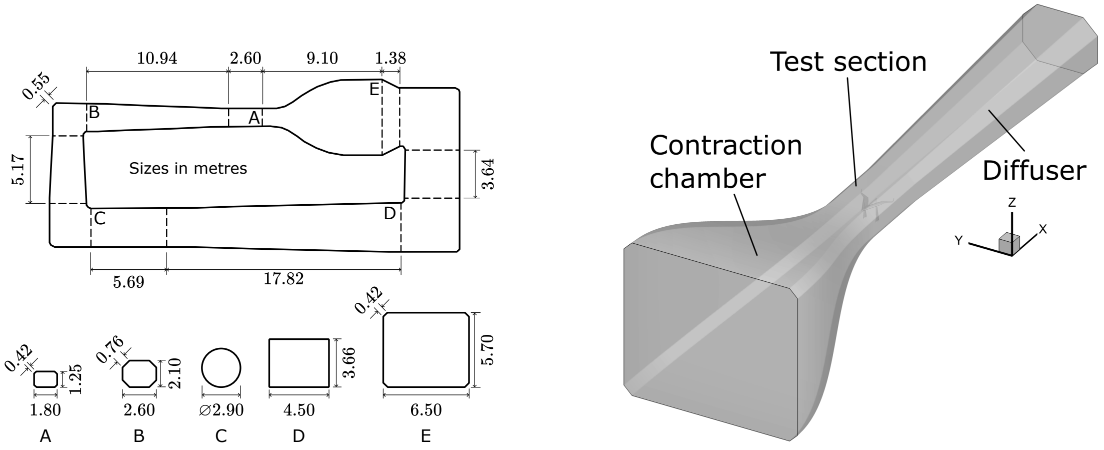

(a) Schematic view including dimensions **(b) Isometric view including support struts**

Figure 3. Geometry of the LTT

B. Computational Setup and Strategy

ANSYS Fluent® 2021R2, an unstructured finite-volume cell-centred solver, is used to perform the simulations. Across all simulations, the flow is prescribed to be fully turbulent; while it may be laminar in the wind tunnel in certain cases, it is assumed that the flow will be adequately tripped over the surfaces since this more closely mimics the boundary layer behaviour at larger Reynolds numbers. The *curvature correction* option is enabled to prevent the erroneous build-up of turbulence viscosity in the vortex cores [7, 8]. Due to a limitation in the meshing software, the y^+ value is maintained under 10, rather than the ideal limit of 1. The effectiveness of this method's y^+ insensitive wall treatment is evaluated in Section III. First-order spatial discretisation schemes are used for density, momentum, turbulence kinetic energy, specific rate of dissipation, and temperature over the first 2 000 iterations, or until the solution stabilises, after which point all spatial discretisation schemes are changed to second-order. These are paired with the PRESTO! pressure interpolation scheme due to its higher stability under the presence of highly rotating flows, such as those in vortex cores[2]. For the equation of state, the fluid is assumed to be an ideal gas using Sutherland's three-coefficient method to calculate the dynamic viscosity as a function of temperature. Gradients are calculated using the Least Squares Cell-Based method. Lastly, Fluent's hybrid initialisation is used for the free-air simulations, while full multigrid (FMG)

---

[2] www.afs.enea.it/project/neptunius/docs/fluent/html/ug/node331.htm, accessed on 28 Sept. 2023

initialisation is used for the wind tunnel tests. These settings enable the simulations to be run on the available hardware at a reasonable compromise of speed, robustness and accuracy. A data-driven approach is taken towards choosing the turbulence model and pressure-velocity coupling which is detailed in Section III.

The domains and boundary conditions for the confined and free-air simulations differ substantially. The free-air simulations feature a cubical domain which extends ten times the largest dimension of the Flying V in all directions. A velocity inlet is defined on five faces, with a pressure outlet on the rear face. The velocity is set to 50 m/s at sea-level conditions. On the other hand, the wind tunnel domain features a pressure inlet, slip walls, a pressure outlet and no-slip aircraft and strut walls. The total pressure and temperature at the inlet are set to 102 856 Pa and 289.94 K respectively, while the static pressure at the outlet is set to 102 623 Pa. Assuming constant mass flow, an empty tunnel and standard sea-level conditions at the throat yields an airspeed of 2.8 m/s, 50 m/s and 19.5 m/s at the inlet, throat and outlet, respectively. Both domains are shown in Fig. 4. The turbulence level is taken as 0.06% in the wind tunnel, slightly below its maximum level of 0.07% at 75 m/s. The free-air scenarios, on the other hand, assume a turbulence level of 0.1% [5]. Across all simulations, a non-zero operating pressure of 101 325 Pa is used to avoid round-off errors since at these Mach numbers ($M \approx 0.15$), the changes in pressure induced by the model are small relative to the freestream static pressure[3].

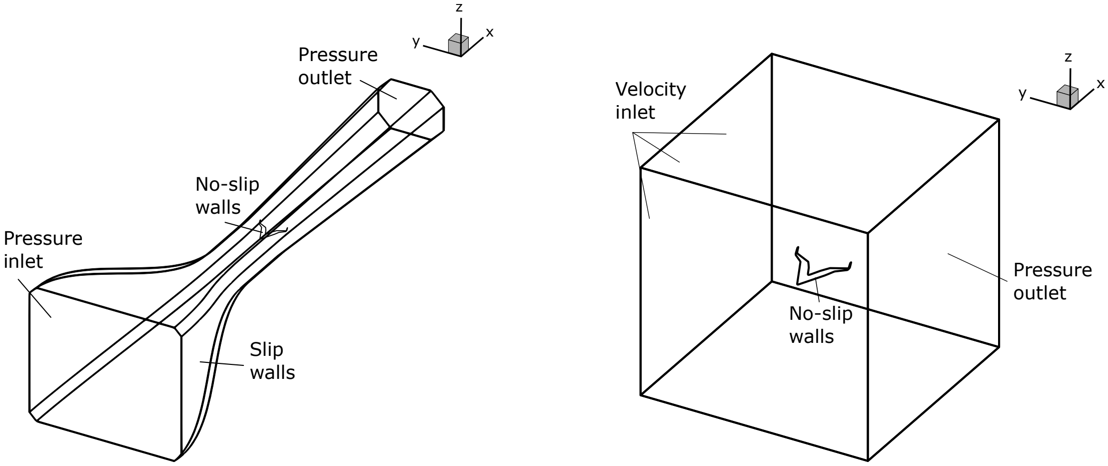

(a) Wind tunnel **(b) Free-air**

Figure 4. Schematic view of simulation domains

C. Classical Corrections

The high-fidelity wind tunnel corrections in this article are benchmarked against the classical corrections currently in place at the LTT, which are calculated using the method of images. This method involves emulating the true conditions inside the wind tunnel using the Laplace equation for irrotational flow. This is done through the rigorous use of singularities (e.g., sources, sinks, doublets), with their exact distribution in the domain being a function of the model geometry, wind tunnel geometry, and flow conditions. It is then assumed that the solution to this system is a sufficiently close approximation of an equivalent solution to the Navier-Stokes equations. The direct solution of the Navier-Stokes equations is not used because it is often too expensive to obtain. Barlow et al. summarised the results from several sources using the data to present various correction models that take as inputs the aircraft performance and geometry as well as the

---

[3] `www.afs.enea.it/project/neptunius/docs/fluent/html/ug/node331.htm`, accessed on 2 Oct. 2023

test section shape and output the changes in forces and moments [9]. This allows for the corrections to be calculated without having to model the wind tunnel numerically with the method of images. The accuracy of the aforementioned models pivots on two fundamental assumptions:

1) There is a large volume of irrotational flow between the rotational flows at the test article and the walls for which the Laplace equation is a satisfactory model.
2) The boundary conditions are imposed in such a way that the solution is indeed representative of the equivalent Navier-Stokes solution.

It is not immediately clear that both assumptions are satisfied in these wind tunnel tests. Foremost, at certain conditions, the Flying V generates strong vortices over its leading edge, which flow downstream. This implies there is a large volume of rotational flow in the domain, in between the rotational flows past the walls and the aircraft. While it can be argued that this phenomenon can be modelled with vortex singularities, Barlow et al.'s implementation of the method of images does not account for this additional vorticity. Secondly, the Flying V features a very complex geometry, which similarly is not accounted for in Barlow et al's implementation. Examples include the kink between the inboard and outboard sections of the wing, the large sweep angle, and the curved winglets. Only panel methods can take into account such complex geometries but these do not offer superior accuracy to Navier-Stokes codes while still requiring a significant time and skill investment, albeit at a lower computational cost [9]. RANS has the advantage of not only providing high-fidelity insights into wind tunnel effects but, in doing so, also offering insights into the test article's performance and surrounding flow field. The effectiveness of the classical corrections is evaluated in Section IV.

D. Data Extraction

In Eqs. (1) to (6), the equations for the force and moment coefficients are shown. They are defined as positive in the forward direction relative to the airspeed axes - these are obtained by rotating the aircraft body reference axes seen in Fig. 2b around the z axis by β, followed by a rotation around the y axis by α. The moments follow the same convention using the right-hand rule.

$$D = C_D \frac{1}{2} \rho_\infty V_\infty^2 S \quad (1) \qquad Y = C_Y \frac{1}{2} \rho_\infty V_\infty^2 S \quad (2) \qquad L = C_L \frac{1}{2} \rho_\infty V_\infty^2 S \quad (3)$$

$$l = C_l \frac{1}{2} \rho_\infty V_\infty^2 b S \quad (4) \qquad m = C_m \frac{1}{2} \rho_\infty V_\infty^2 \bar{c} S \quad (5) \qquad n = C_n \frac{1}{2} \rho_\infty V_\infty^2 b S \quad (6)$$

In Eqs. (1) to (6), ρ and V, relate to the density and airspeed, respectively, with the '∞' subscript denoting freestream conditions. The integral drag, sideforce, lift, rolling moment, pitching moment and yawing moment are denoted by D, Y, L, l, m, n, respectively. In addition to this, the pressure coefficient is also presented over the aircraft using the relation given in Eq. (7). The Reynolds number is calculated with respect to the mean aerodynamic chord - its formula is shown in Eq. (8), where μ_∞ is the freestream dynamic viscosity of air. The aircraft parameters used for non-dimensionalisation are summarised in Table 1. Standard sea-level conditions are used for the density, pressure, temperature and viscosity. At an airspeed of 50 m/s, this yields a freestream Mach number of 0.147.

$$C_p = \frac{p - p_\infty}{\frac{1}{2} \rho_\infty V_\infty^2} \quad (7) \qquad Re = \frac{\rho_\infty V_\infty \bar{c}}{\mu_\infty} \quad (8)$$

Table 1. Sub- and full-scale Flying V parameters

Parameter	Symbol	Scaled value	Full-scale value	Units
Mean aerodynamic chord	$\bar{c}$	0.338	18.3	m
Aircraft span	b	1.20	65.0	m
Wing area	S	0.307	902	m^2
Reynolds number	Re	1.16×10^6	62.7×10^6	-

E. Interpolation Method

The test matrix for this investigation is relatively coarse; it features four points in both α and β, including every combination of the two for a total of 16 points. Across all 16 combinations, 6 different coefficients are calculated. Interpolation is used to obtain refinements in the coefficients within the equispaced intervals. *Thin-plate splines* can accommodate the non-linearity of the results in a portable format, with minimal artefacting.

A thin-plate spline is constructed by placing radial basis functions (RBFs) at various combinations of the input variables. For instance, every combination of β and α. A bilinear polynomial may be superimposed with these basis functions to improve the quality of the interpolation. The surface is mathematically described by the sum of these basis functions with the polynomial, each multiplied by a coefficient which can be tuned. The coefficients are obtained by forcing the surface to lie on an arbitrary set of input data. In the case of interpolating a coefficient of the Flying V, using as input the predicted values at the 16 combinations of α and β, it takes 16 coefficients to describe the basis functions, with another three coefficients being used for a bilinear polynomial component. With these coefficients, the model can easily be rebuilt retroactively. MATLAB®, for instance, features a built-in function which takes as input these coefficients and the basis function centres and outputs the interpolation function (see `stmak`)[4].

The equation of a surface, f, obtained with thin-plate spline interpolation with 19 coefficients is shown in Eq. (9), where $\mathbf{x}$ is the attitude vector, $[\beta, \alpha]$; $|\mathbf{x}|$ is the Euclidean norm of a vector $\mathbf{x}$; $\Psi(r)$ is the radial basis function, $\Psi(r) = r \log r$; $\mathbf{a}$ is the vector of interpolation coefficients; and $\mathbf{c}$ is the vector of interpolation centres, taken as the combinations of β and α. The coefficients are calculated using MATLAB®'s `tpaps`[5].

$$f(\mathbf{x}) = \underbrace{\sum_{j=1}^{n=16} \mathbf{a}_j \cdot \Psi\left(|\mathbf{x} - \mathbf{c}_j|^2\right)}_{\textit{Scaled radial basis functions}} + \overbrace{\mathbf{a}_{17} \cdot \beta + \mathbf{a}_{18} \cdot \alpha + \mathbf{a}_{19}}^{\textit{Bilinear polynomial}} \tag{9}$$

---

[4] https://nl.mathworks.com/help/curvefit/stmak.html, accessed on 23 Oct. 2023

[5] https://nl.mathworks.com/help/curvefit/tpaps.html, accessed on 17 Nov 2023

III. Validation

To establish the accuracy of the current method, and to gain confidence in the quality of the results, the current procedure is validated using external experimental and numerical data from the DLR F-19, also known as the Stability and Control Configuration (SACCON). This particular aircraft was chosen for its geometrical similarities with the Flying V, namely, its large leading edge sweep angle. This entails that both form strong vortices over the leading edge at moderate to high angles of attack. This validation is intended to provide a data-based approach towards tuning the mesh refinement and solver settings while also quantifying the current method's ability to predict highly vortical flows.

A. Meshing Strategy

Due to the complexity of the flow around the Flying V, the meshing strategy must be carefully considered. RANS's ability to predict nuanced flow structures, such as vortices, is highly dependent on the mesh resolution and quality [10]. The DLR F19, whose geometry is shown in Fig. 5, is used as a test bench to identify the most appropriate meshing strategy in terms of accuracy and performance.

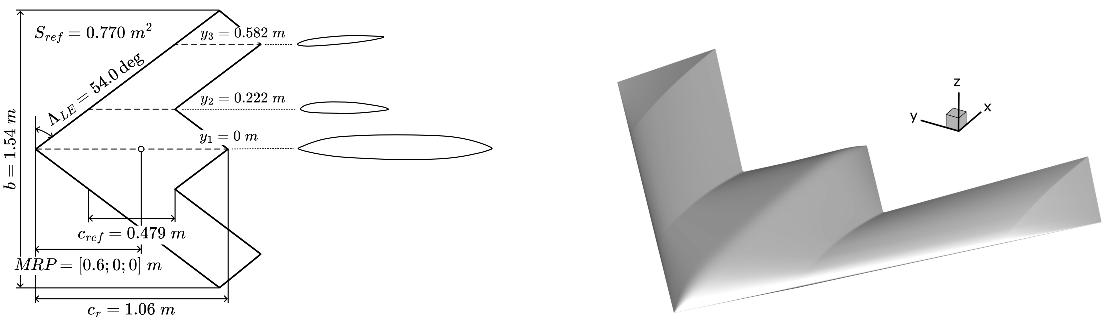

(a) Schematic view including dimensions **(b) Isometric view**

Figure 5. Geometry of the DLR F19

The current version of the F19 features a truncated trailing edge which was discretised into four cells along its width for the baseline mesh. This avoids the formation of poor-quality elements around this region, such as highly skewed cells, or excessive volume ratios. A local sizing is added to the aircraft, such that the maximum curvature allowed is 5°, with a maximum size of 1.5 mm and a minimum size of 0.2 mm. A body of influence (BOI) with a local cell size of 20 mm encases the aircraft to enhance the prediction of off-body phenomena such as flow separation or vortices. The cell size at the inlet and outlet of the domain is fixed at 5 m. The aircraft features 30 inflation layers with a first-layer height of 7 μm. For the mesh refinement study, the surface grid is coarsened by a factor of 2 for the coarse mesh, and refined by a factor of 1.5 for the fine mesh. This yields a coarse mesh with 16.3×10^6 elements, a baseline mesh with 41.0×10^6 elements, and a fine mesh with 94.9×10^6 elements. The lift, drag and pitching moment polars for each variation are compared against the baseline alongside experimental and numerical data from Frink et al. [11] in Fig. 6. The latter employs EDGE's[6] implementation of Detached Eddy Simulations (DES) with the Spalart-Allmaras turbulence model and a static mesh. The inclusion of external numerical data allows for an evaluation of the method's implementation (verification), while the experimental data allows for an evaluation of the method's accuracy (validation). The exact simulation conditions for the validation study can be found in Table 5.

---

[6] `https://www.foi.se/rest-api/report/FOI-R--0298--SE`, accessed on 7 Dec. 2023

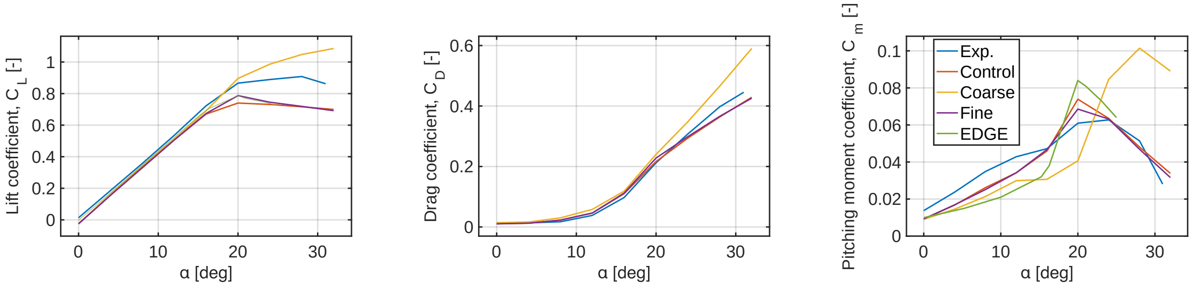

(a) Lift **(b) Drag** **(c) Pitching moment**

Figure 6. F19 polars for different mesh refinement levels

B. Solver Tuning

In addition to the mesh refinement study, the influence of the turbulence model, pressure-velocity coupling scheme, and y^+ value are also investigated. For the latter, the baseline mesh is adapted to feature a y^+ value no greater than ten versus the default value of one. This comparison is necessary due to the meshing software's inability to produce elements of sufficient quality at very low first-layer heights over highly curved surfaces, which is the case for the Flying V at high Reynolds numbers. The turbulence model and pressure-velocity coupling scheme are investigated to identify a compromise between speed and accuracy. The baseline case consists of a mesh with 41.0×10^6 elements, the $k - \omega$ turbulence model, the SIMPLE pressure-velocity coupling scheme, and a y^+ value no greater than one across the surface of the aircraft. The comparisons to the experimental and numerical results are shown in Figs. 7 to 9.

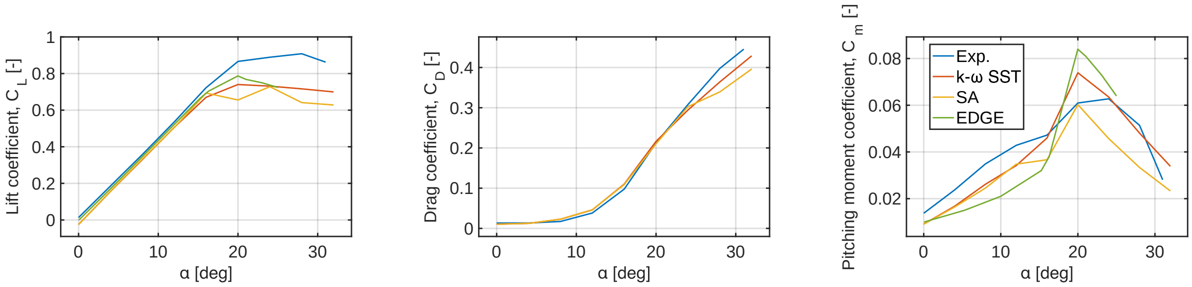

(a) Lift **(b) Drag** **(c) Pitching moment**

Figure 7. F19 polars for different turbulence models

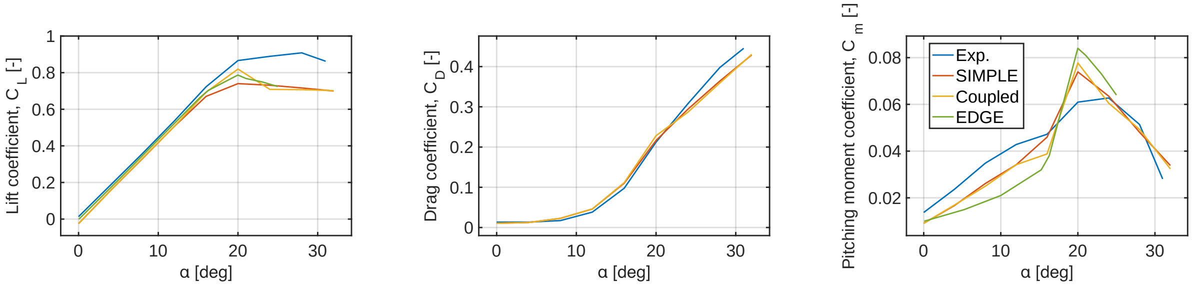

(a) Lift **(b) Drag** **(c) Pitching moment**

Figure 8. F19 polars for different pressure-velocity coupling schemes

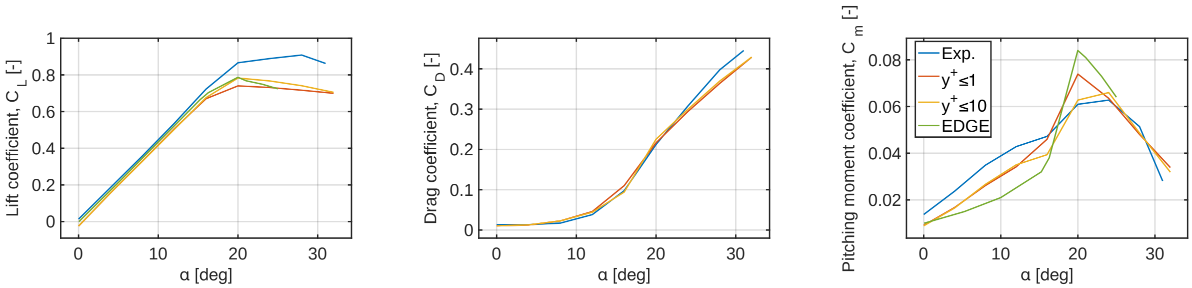

(a) Lift **(b) Drag** **(c) Pitching moment**

Figure 9. F19 polars for varying levels of maximum y^+

C. Chosen Settings

The solver settings must strike a balance between performance, accuracy and robustness. The CPU time is calculated for the entire angle of attack sweep, with each variant being benchmarked against the control configuration. Both the CPU time and the root-mean-square error (RMSE) relative to external data are shown in Table 2.

Naturally, there is a large sensitivity to the mesh refinement level. The coarse mesh, despite featuring roughly 60% fewer elements, takes only a staggering 6% of the time to run. Similarly, the fine mesh features 131% more elements yet takes 193% longer to run. The coarse mesh does not yield sufficiently accurate results, while the fine mesh almost perfectly matches the numerical work of Frink et al. Yet it still does not perfectly replicate the experimental data despite the enormous cost. Given that the flow over the Flying V should not be as challenging to simulate, the baseline mesh emerges as the strongest choice. Furthermore, the Spalart-Allmaras turbulence model does not offer either a convincing performance increase or improved data agreement with the experiment. The coupled pressure-velocity scheme yields virtually identical results to the SIMPLE algorithm at a significantly higher cost, while the lower y^+ value offers comparable results with a reduction of over a third in computational cost. Given the meshing software's limited ability to generate thin elements at the wall, the latter is considered an acceptable compromise taking into account the scope and hardware availability of the current work. Taking all of the above in mind, the baseline configuration appears as the best choice in terms of speed, accuracy and robustness - concerning the latter, none of the simulations show significant differences in convergence stability.

Table 2. Summary of F19 simulation performance and accuracy

Variant	Nodes	CPU hours	Difference	RMSE in lift coefficient	
				wrt. exp. [11]	wrt. EDGE [11]
Control	384	326	-	0.111	0.0730
Spalart–Allmaras	384	347	+6.40%	0.149	0.0949
Coarse mesh	384	19.0	-94.2%	0.0963	0.188
Fine mesh	384	955	+193%	0.104	0.0704
Coupled scheme	576	610	+87.1%	0.108	0.0733
$y^+ \leq 10$	384	209	-35.9%	0.0949	0.0701

D. Method Evaluation

In general, the results show reasonable agreement with the experimental data, with the drag predictions being particularly accurate. The moment predictions are the least accurate as to be expected, since it is well known that RANS approaches tend to struggle in this regard [11, 12]. These conclusions practically mirror those presented by Frink et al. In fact, their numerical results show excellent agreement with the current work, particularly the results from the finest mesh. Frink et al. found that it was 'extremely difficult' to model the vortical flow over the round leading edge of the F19 [11], with the methodologies of the time (2011). Even the same discrepancies were found in the moment coefficient predictions. Upon closer inspection of the flow field, it seems as though the same vortical structures are present in both the experimental and numerical results, although the dynamics of the numerical system show a very high sensitivity to changes in turbulence model, and grid refinement. This is particularly true at high angles of attack, where the correlation between the models is the weakest. Figure 10 shows the surface streamlines, or friction lines, over the F19's upper surface overlaid with the local pressure coefficient. The comparison is made between the current work, which uses ANSYS Fluent® with the $k - \omega$ turbulence model, and NASA's USM3D[7] which in this case, implements the Spalart-Allmaras turbulence model. The figure illustrates how even the numerical methods can feature significant discrepancies in the triple vortex system, despite the agreement in forces and moments. It then follows that the triple vortex system should be examined in more detail.

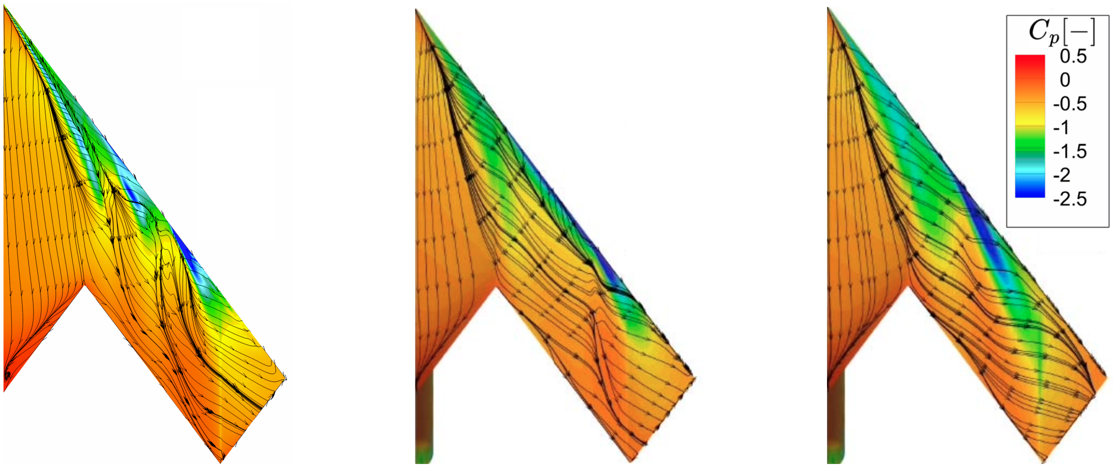

(a) Current work ($\alpha = 16.0°$) **(b) USM3D-SA** ($\alpha = 16.83°$) **[11]** **(c) USM3D-SA** ($\alpha = 17.89°$) **[11]**

Figure 10. F19 pressure coefficient contours and surface streamlines

Figure 11 shows the vorticity contours at various slices of constant x along the aircraft's length. Particle image velocimetry (PIV) data is available from Loeser et al. [13], while reference RANS CFD data is available from Frink et al. [11]. Two important conclusions can be drawn. The first of which is that both CFD approaches overestimate the vorticity at the vortex cores. While the work of Frink et al. overestimates the values at the cores and further off-body, the current work seems to overestimate at the vortex cores and within the boundary layer. The current work features a higher flow resolution, which presumably leads to the clear development of the triple vortex system, albeit to an exaggerated degree compared to the PIV data. The vortex system consists of an 'apex vortex', formed at the apex due to the local sharpness of the leading edge; a 'thickness vortex' formed further outboard due to the separation over the wing which forms near the transition from a sharp to a round leading edge; and a 'tip vortex' slightly inboard of the wingtip. The challenge of predicting these vortical flows correctly lies in accurately predicting the location of these vortices as their interaction will largely dictate the pressure field over the leeside of the wing [14].

---

[7] `https://software.nasa.gov/software/LAR-16670-GS`, accessed on 11 Oct. 2023

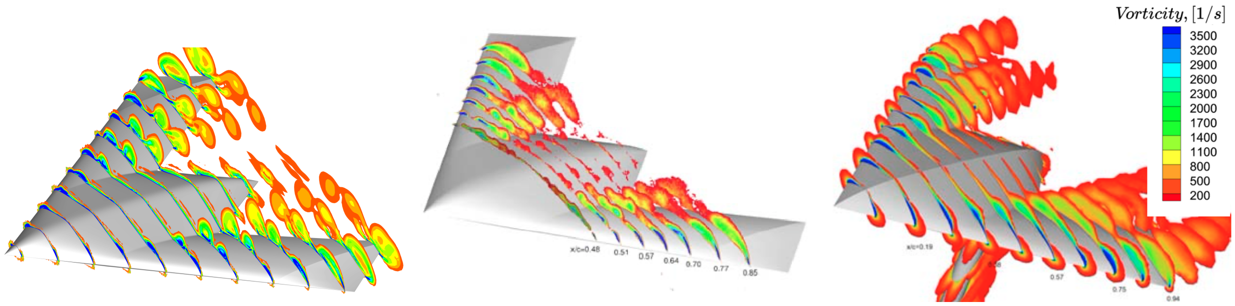

(a) Current work (α = 16.0°) **(b) PIV** (α = 16.9°) [13] **(c) USM3D-SA** (α = 16.83°) [11]

Figure 11. F19 off-body vorticity at slices of constant x

To conclude, this section should elucidate the difficulty of predicting highly vortical flows. Despite the underwhelming agreement with the experiment, the results show that the method is correctly implemented, with the data in line with that of Frink et al. This should inspire confidence in the quality of the data since the reference work coalesces efforts from the National Aeronautics and Space Administration (NASA), the Swedish Defence Research Agency (FOI) and the Defence Science and Technology Group (DSTO). While the flow over the Flying V is also highly vortical, the same challenges should not arise, at least not to the same degree, in simulating its flow field. In part, this is due to the simpler geometry of the Flying V - the vortex locations are fixed at the apex and at the wing kink. The F19 features a nuanced leading edge and upper surface which make for a more complicated flow field. With this in mind, the results from the current work should still be considered with some reservations, as it has been proven that RANS approaches with static meshes are not always able to exactly model highly vortical flows. For a higher degree of confidence in the results, it is recommended that DES are considered since they apply more detailed physics fundamentally, and also yield a time-dependent solution, which may capture vortex breakdown more accurately. It is also suggested that this is paired with a dynamically refining mesh - with this approach the mesh at the vortex cores can be automatically refined based on the local solution gradients. This ensures better resolution of the vortices at a non-prohibitive cost. Neither of these recommendations was possible to implement due to the scale of the investigation, hardware availability and software restrictions.

IV. Results

In this section, the meshing process for the Flying V is described, followed by a discussion on the convergence and performance of the simulations. Once the quality of the simulations is assured, the wall and strut corrections are introduced - these are defined as the delta between the confined and free-air, sub-scale simulations. These results are followed by the Reynolds number corrections, which similarly are defined as the delta between the full- and sub-scale simulations, both in free-air. Following this, the classical corrections are introduced and their accuracy is evaluated. Subsequently, the thin-plate spline interpolation applied to the Flying V polars is discussed, including how these are used to build surrogate models for the wall and strut, and Reynolds number corrections, respectively. Finally, the interpolation is validated with additional scaled Flying V runs.

A. Mesh Description

The meshing process incorporates the insights from Section III. Similarly to the F19, the CAD model of the scaled Flying V used for simulations features a truncated trailing edge. It measures 0.2 mm or approximately 0.059% of the mean aerodynamic chord. The trailing edge of the scaled aircraft is meshed such that there are always four elements along its width. A local sizing is added to the aircraft, such that the maximum curvature allowed is 5°, with a maximum size of 1.5 mm and a minimum size of 0.05 mm. A body of influence (BOI) with a local cell size of 15 mm encases the aircraft to enhance the prediction of off-body phenomena such as flow separation or vortices. The cell size at the walls, inlet and outlet of the LTT is fixed at 1 000 times the smallest cell size, i.e., 50 mm. Another local sizing condition is applied to the struts such that the maximum curvature is 5° and the smallest and largest sizes allowed are 0.1 mm and 1.5 mm, respectively. The surface mesh of the scaled Flying V is shown in Fig. 12a - the grid for the full-scale aircraft is identical but refined by a factor of 2.5. The struts and aircraft are modelled as no-slip walls. Therefore, 30 inflation layers are added with a first-layer height of 70 μm for the scaled scenarios, and 100 μm for the full-scale scenario. Due to the larger domain of the free-air simulations, these feature a cell size at the domain walls of 10^4 times the smallest element, i.e., 5 m and 150 m for the scaled and full-scale scenarios, respectively. The volume mesh is then populated with poly-hex cells for all scenarios, producing a scaled mesh with 35.3×10^6 cells, wind tunnel meshes with 54.5×10^6 cells on average, and a full-scale mesh with 144×10^6 cells. For a visual inspection of the meshes, refer to Appendix B. Each configuration in the wind tunnel required a separate mesh meaning that, in total, 18 meshes were used. All 18 meshes used feature an average inverse orthogonality greater than 0.8 and a minimum value no smaller than 0.05.

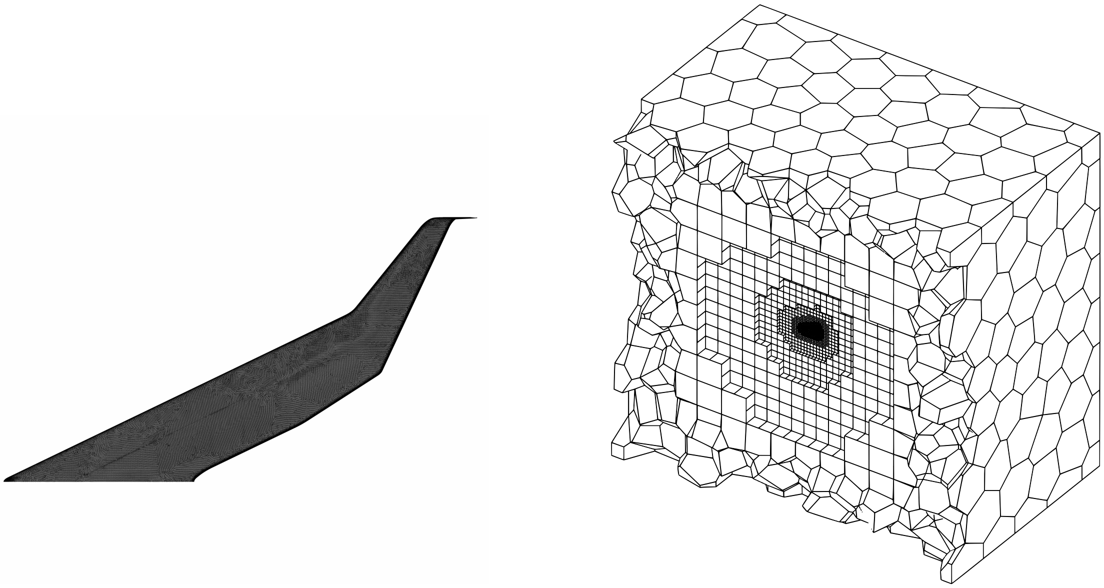

(a) Surface mesh **(b) Cut volume mesh**

Figure 12. Scaled Flying V mesh showcase

B. Simulation Convergence

The forces at each iteration are shown in Fig. 96. The total forces are included in Figs. 96a to 96c, with their normalised counterparts in Figs. 96d to 96f. The normalisation is done with respect to the final, or *converged* value. As a result of vortex shedding on the circular struts, oscillations are present in the normalised solution of the wind tunnel simulations. Their amplitude is never concerning, reaching a maximum of 6% of the converged value at an angle of attack of 0°, where the absolute value is small, and around 0.1% of the solution for the remaining simulations. Across all simulations, the amplitudes are too small to be considered relevant and therefore are not shown in the data.

The effect of changing the order of the discretisation scheme is very apparent. This change can be seen when the solution jumps violently within the first 2 000 iterations. Upon inspection of the last 100 iterations using the first- and second-order discretisation, it is clear that the solution stabilises at significantly different values - the difference at times is in the order of 20%. Not only is there a large delta in the forces between the discretisation schemes, but the first-order schemes often do not appear to predict any vortex shedding, which is a major phenomenon of the flow field. This dual-scheme method successfully accelerates convergence without compromising accuracy.

With the above information, it can be concluded with a high degree of confidence that the simulations are indeed converged. The residuals - see Fig. 95 - and solution variables are all stable during at least the last 100 iterations, with any changes remaining below 0.1% of the converged value and the flow field exhibiting no non-physical artefacts.

C. Simulation Performance

All simulations were run on AMD EPYC™ 7643 processors featuring 48 cores and DDR4 memory, which was allocated proportionally to the total number of nodes used. For each scenario, Table 3 shows the total CPU hours taken for each full test matrix, as well as the average time taken per iteration and per run in seconds. Naturally, the full-scale simulations are the most expensive due to the large grid size, followed by the wind tunnel and scaled scenarios.

Table 3. Simulation performance for Flying V runs

Scenario	CPU hours	Seconds/iteration	Seconds/run	Nodes
Scaled	4 860	2.98	5 690	192
Wind tunnel	18 600	2.17	8 700	480
Full-scale	36 000	5.48	14 100	576

D. Wall and Strut Effects

The walls and struts act to confine the flow, artificially increasing the airspeed the test article encounters relative to the free-air condition. This in effect means the model appears to produce more lift and drag than expected as evidenced by the corrections in Fig. 13: both the lift and drag corrections at low to moderate angles of attack are negative. At high angles of attack, the leading edge vortices dominate the flow field. The walls confine their vorticity and increase their suction. As these flow downstream and their pressure normalises back to the freestream pressure, they encounter a higher adverse pressure gradient than the free-air scenario. Under the current conditions, this higher adverse pressure gradient causes the vortices to break down. Since these vortices tend to stabilise the flow over the leeside of the wing, their absence causes most of the outboard wing to stall, advancing the onset of separation and stall to a lower angle of attack. From Fig. 13, it can be seen that the highest angles of attack generally do not follow the same trend as the rest of the data points. Furthermore, this change to the vortex system has a vast impact on the moments felt by the model. Since the vortices have a strong stabilising effect on the pressure over the leeside, any disturbance to them will change the pressure distribution over the aircraft. Small changes in the distribution may not affect the forces greatly, but they may shift the location of the resultant aerodynamic force, thus greatly affecting the moments experienced by the aircraft. This is clearly visible in Fig. 13e, where the difference in pitching moment between the confined and free-air simulations is highly irregular, with no clear pattern emerging presumably due to unstable vortices.

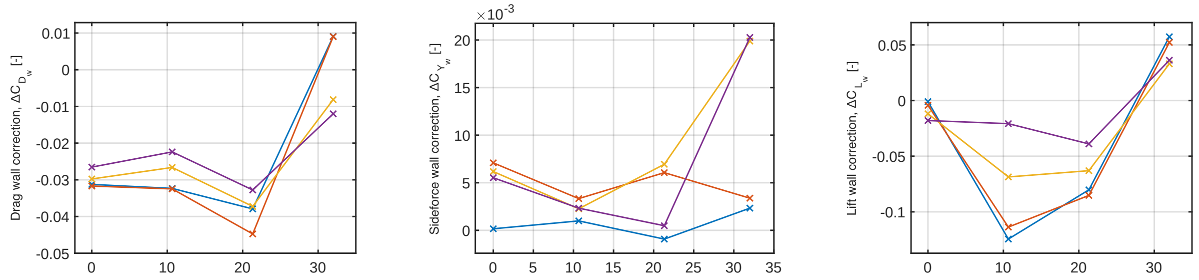

(a) Drag **(b) Sideforce** **(c) Lift**

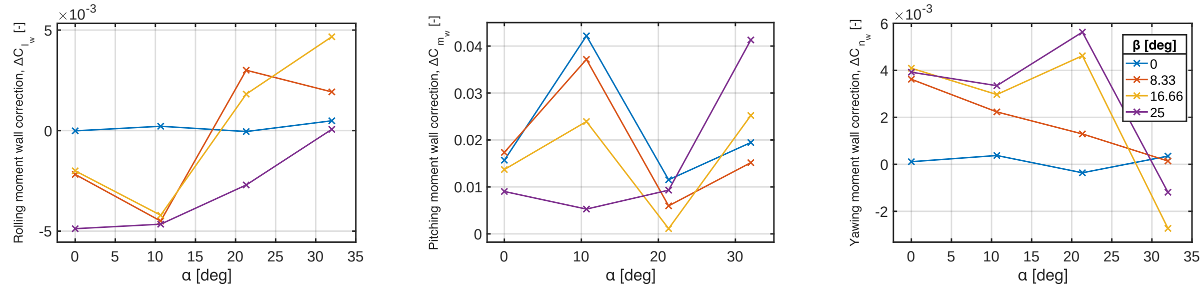

(d) Rolling moment **(e) Pitching moment** **(f) Yawing moment**

Figure 13. Corrections for wall and strut effects

Consider the leading edge vortices over the Flying V in symmetric conditions. In free-air, these travel downstream over the aircraft, creating a 'streak' of low pressure on the upper surface, e.g. in Fig. 46. In the wind tunnel, the presence of the walls decreases the pressure at their cores and promotes premature breakdown, thereby generating higher pressures near the aft of the aircraft. One may not expect this new distribution to yield a substantially different magnitude of the resultant force, but its location would very likely shift. This is the underlying mechanism that is dominating the moments, despite relatively small changes to the forces.

The angle of sideslip has a profound impact on the performance of the Flying V. It appears as though sideslip inversely affects the strength and coherence of the left and right leading edge vortices. With the flow reaching the wing from the right, the right wing effectively features less sweep, with the opposite being true for the left wing. This, in turn, reduces the strength of the right vortex. Without this stabilising factor, the flow over this section of the wing is more susceptible to stall, as evidenced by the pressure loss contours in Appendix G. The right wing at times is completely stalled, while the left wing features mostly attached flow. Under high angles of sideslip, the left vortex appears stronger and to flow further downstream often showing few signs of breakdown. The data shows a small separation region just aft of the left leading edge which is subsequently controlled by the left vortex. This is true across all three conditions, which contributes to a significant reduction in drag coefficient at high angles of attack. Due to the severe stall on the right wing across all conditions, the lift generation at high angles of sideslip is moderately hampered. For the full-scale aircraft, the stall is concentrated towards the outboard wing only. Due to the higher Reynolds number, this is also the only condition which does not show signs of stall in the sideforce polars. Due to the asymmetric stall, the moments are all greatly affected by the angle of sideslip, although to different degrees between the three conditions. While the scaled and full-scale predictions suggest that the pitching and yawing moments are still increasing beyond an angle of attack of 32°, the wind tunnel moment predictions appear to reach a maximum at 21.33°. The exact mechanism behind this discrepancy is unclear.

E. Reynolds Number Effects

At the full-scale Reynolds number, there is a large discrepancy in the data sets at high angles of attack and sideslip. The mechanism behind the discrepancy is relatively simple, but its effect is profound. The full-scale aircraft features a proportionally thinner boundary layer, with an increased level of turbulence and higher resistance to adverse pressure gradients. As evidenced by the pressure loss contours such as Fig. 62, the onset of separation is significantly delayed in the full-scale aircraft. This is clearly visible in Fig. 14, where the corrections suggest that the aircraft should, in fact, reach substantially higher maximum forces and moments at a lower drag penalty.

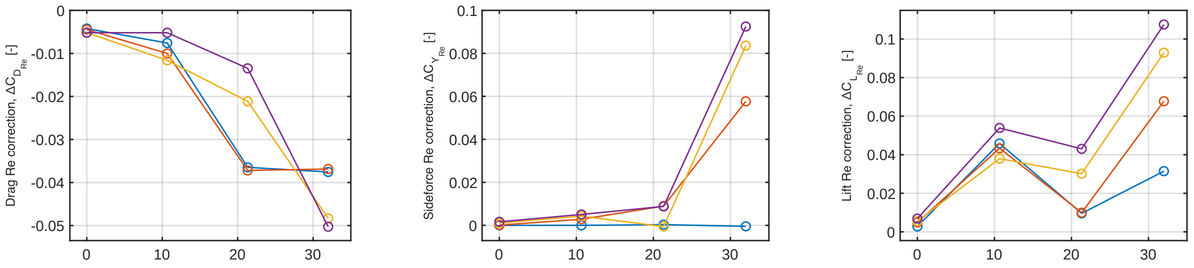

(a) Drag **(b) Sideforce** **(c) Lift**

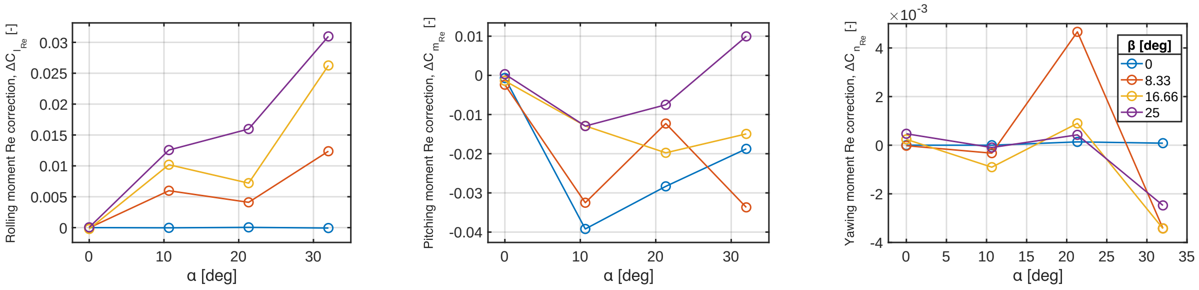

(d) Rolling moment **(e) Pitching moment** **(f) Yawing moment**

Figure 14. Corrections for Reynolds number effects

A consequence of the higher turbulence levels within the boundary layer is higher pressure loss under attached conditions. Take for instance Fig. 62: there is a visible wake over most of the wing in both of the sub-scale scenarios, while this is only true for the outboard wing of the full-scale aircraft. The pressure loss over the leading edge of the full-scale aircraft is also noticeably higher. The same logic applies to the vertical tail, hence the delayed stall in sideforce in Fig. 37. This is also confirmed by the pressure coefficient contours and the surface streamlines in Fig. 45. The full-scale aircraft maintains a strong pressure peak along its right leading edge, while in both sub-scale models, the pressure is close to ambient - an indication of stall. The conclusion that can be drawn from the data is unsurprising - the full-scale aircraft is more resistant to stall.

F. Comparison with Classical Corrections

The classical corrections shown in Fig. 15 do not reflect the findings of the numerical results from Fig. 13 to an acceptable level of accuracy. Foremost, the classical corrections are not able to account for the non-linearities arising at extreme attitudes. Since the corrections are a function of the lift generated by the confined aircraft, among other variables, they assume that the same phenomena are taking place in the wind tunnel as in free-air. As a result, both the general shape of the correction curves and the magnitudes are remarkably incorrect. The results are only comparable in trivial scenarios, such as the rolling moment, yawing moment and sideforce coefficients at symmetric conditions. It can therefore be deduced that the classical corrections cannot accurately account for the complex flow phenomena over the Flying V to a sufficient degree of accuracy, likely because the underlying assumptions are not valid.

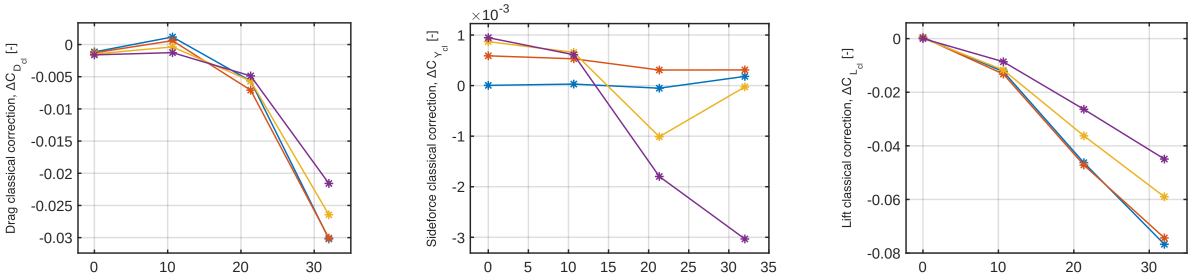

(a) Drag **(b) Sideforce** **(c) Lift**

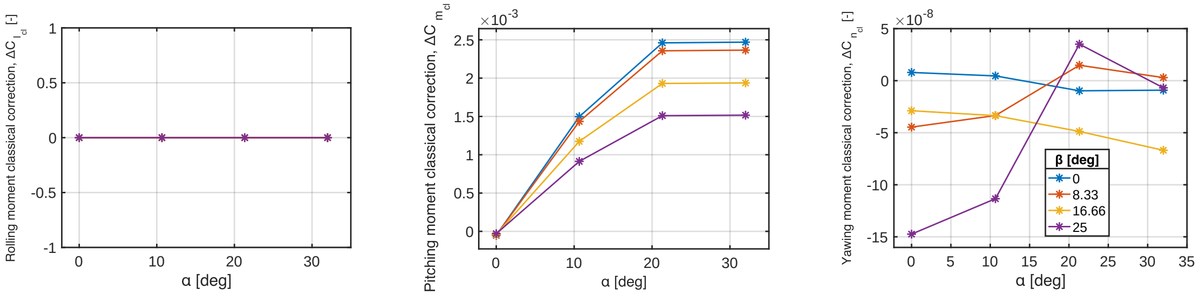

(d) Rolling moment **(e) Pitching moment** **(f) Yawing moment**

Figure 15. Classical corrections

G. Data Interpolation

As discussed in Section II, thin-plate spline interpolation is applied to the results in order to overcome the relative sparsity of the test matrix. This method is applied to the forces and moments rather than to the correction factors because the latter is highly scattered, meaning that any interpolation attempts would likely return invalid results. Across the three scenarios, for each of the six force and moment coefficient polars, all 19 interpolation coefficients, **a**, are documented in Appendix D, for parties interested in reproducing the results retroactively. An example of the interpolation is shown for the sub-scale drag coefficient in Fig. 16.

Take, as an example, the free-air, sub-scale and wind tunnel drag coefficients. Subtracting the latter from the former yields the correction factors in terms of α and β for the effect of the walls and struts. Applying the same logic to the full- and sub-scale coefficients would yield a correction contribution for the influence of the Reynolds number.

$$C_{D_{\textit{free-air, full-scale}}} = \underbrace{C_{D_{\textit{wind tunnel}}} + \Delta C_{D_{\textit{walls}}}}_{C_{D_{\textit{free-air,sub-scale}}}} + \Delta C_{D_{Re}} \tag{10}$$

By using the splines for the coefficients, this approach effectively provides a surrogate model for the wind tunnel corrections for any combination of β and α, requiring only three inputs: the angle of attack, the angle of sideslip and the measured coefficient of interest. Both correction contributions - for the effect of the walls and struts and for the effect of the Reynolds number - can be accounted for independently. The interpolation centres, **c**, are the same as for the coefficient interpolations, while the interpolation coefficients, **a**, are shown in Appendix E.

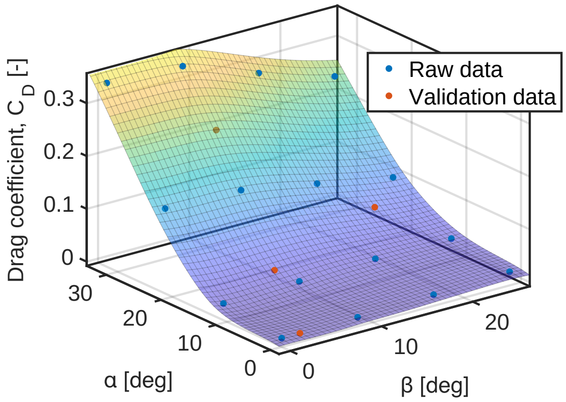

Figure 16. Thin-plate spline surface for sub-scale drag coefficient including validation points

To evaluate the accuracy of the interpolation, four additional runs are carried out on the scaled aircraft. The four attitudes are randomly distributed while avoiding proximity to existing data points. The validation attitudes are shown in Table 4a. The thin-plate splines for the scaled conditions are evaluated at these attitudes and are compared to the RANS simulations. The RMSE across all four simulations is documented in Table 4b for each coefficient. The interpolation errors can also be visualised in Appendix I.

While the interpolation shows excellent agreement at low angles of attack and sideslip, the non-linearities at high angles become hard to predict with such coarse data and consequently, the accuracy of the data fitting suffers. The surfaces for the full-scale aircraft, for instance, feature a much simpler topology with less curvature, since there are no signs of stall. This makes them much better candidates for interpolation. Generally speaking, the interpolation yielded the best results for the drag, lift and yawing moment. Their splines may be used with a high degree of confidence across the entire test matrix. Since the remaining coefficients are much more sensitive to stall, their interpolation should be considered with caution, particularly close to extreme attitudes.

Table 4. Summary of interpolation validation

(a) Attitude combinations for validation

Run	Angle of sideslip	Angle of attack
1	9°	27°
2	2°	0°
3	21°	18°
4	7°	13°

(b) Interpolation error

Coefficient	RMSE
Drag	0.00549
Sideforce	0.00400
Lift	0.00897
Rolling moment	9.22×10^{-4}
Pitching moment	0.00862
Yawing moment	4.37×10^{-4}

V. Conclusion

The current work presents high-fidelity corrections for wind tunnel effects over the Flying V through the use of state-of-the-art RANS codes. The analyses elucidate the complex vortical flow structures around the aircraft at high angles of attack and provide insights into their sensitivities to the presence of the walls and struts, as well as Reynolds number. Namely, the presence of the walls confines the vorticity at the vortex cores, creating stronger suction and a consequently more abrupt adverse pressure gradient near the aft of the aircraft. This, in turn, is reflected in the force polars to a moderate degree: the onset of stall is advanced under confined conditions. The moments are significantly and chaotically affected, with the corrections featuring large magnitudes with no clear trend. The increase in Reynolds number has the opposite effect: it stabilises the boundary layer over the aircraft, making it more resilient to stall. The flow remains attached over most of the aircraft across the entire attitude range in full-scale conditions, with the vortices being more concentrated. Presumably due to higher levels of turbulence in the boundary layer, higher pressure loss is also observed over the surface. Lastly, the angle of sideslip acts to increase the severity of stall, when present, on the right wing (for positive angles), while greatly stabilising the flow on the left wing. The left vortex becomes smaller in diameter but extends further downstream to cover more of the wing. As a result, even at extreme attitudes the flow over the left wing has a strong tendency to remain attached, leading to decreased drag and lift at high angles of attack relative to the low sideslip conditions. The moments show a high sensitivity to the sideslip due to the significant changes to the pressure distribution. The free-air predictions suggest that the moments have not reached a maximum value at 32° of angle of attack, unlike the confined simulations. The classical corrections cannot, to any capacity, predict any of the complex interactions described above. These corrections did not match either the sign or the order of magnitude of the CFD corrections across most of the test matrix, thereby motivating such an involved procedure for the prediction of corrections for wind tunnel effects. As an alternative to the classical method, a thin-plate spline-based surrogate model of the corrections is presented which returns corrections within the equispaced points provided by the simulations.

The main limitations of the current work are primarily concerned with hardware and software constraints. Foremost, the software suite available strongly restricted the maximum aspect ratio at the walls, thereby constraining the dimensionless wall distance. This parameter has been proven to have a significant impact on the prediction of separated flows. While the validation suggests that this effect is minimal, it is strongly recommended that future RANS analyses of the Flying V revise the meshing procedure. On a hardware-related note, the accuracy of the results would have benefited from both finer discretisation and more accurate physics modelling. More specifically, DES and dynamic mesh refinement appear as strong candidates to improve the fidelity of the data. The former uses a different approach towards solving turbulence which should capture more subtleties in the flow field, and its unsteady approach should more accurately predict vortex breakdown and its effect on the rest of the flow. The latter ensures that the mesh is refined and coarsened locally, based on solution gradients such that the resources can be allocated more efficiently, making the most out of the available hardware. In both cases, more hardware power is required, and dynamic mesh refinement was not available at the time of writing. Finally, the thin-plate spline interpolation showed good agreement with the validation data, however, the highly non-linear nature of the flow over the Flying V at high angles calls for more data points to be collected. No interpolation method is suggested to improve the quality of the interpolation.

This article puts forth convincing evidence that RANS not only gives a better understanding of a test article's aerodynamic performance, both in confined and free-air conditions, but also gives higher confidence in the understanding of wall, strut and Reynolds number effects at a significant, yet reasonable computational cost. Such an approach is strongly recommended for similar investigations provided that similar or more powerful hardware is available.

References

[1] Benad, J., and Vos, R., "Design of a Flying V Subsonic Transport," *33rd Congress of the International Council of the Aeronautical Sciences*, 2022.

[2] Siemonsma, K., "Aerodynamic model identification of the Flying-V using flight data," , 2022. Unpublished TU Delft MSc thesis.

[3] Laar, Y., "Aerodynamic Design of a Flying V Aircraft in Transonic Conditions," , 2023. Unpublished TU Delft MSc thesis.

[4] Timmer, W., "Two-dimensional low-Reynolds number wind tunnel results for airfoil NACA 0018," *Wind Engineering*, 2008.

[5] Goetten, F., Finger, D. F., Marino, M., Bil, C., Havermann, M., and Braun, C., "A review of guidelines and best practices for subsonic aerodynamic simulations using RANS CFD," *Asia-Pacific International Symposium on Aerospace Technology-APSIAT 2019*, 2019.

[6] van Arnhem, N., de Vries, R., Vos, R., and Veldhuis, L. L., "Aerodynamic performance of an aircraft equipped with Horizontal Tail mounted propellers," *AIAA Aviation 2019 Forum*, 2019, p. 3036.

[7] Stokkermans, T. C., Van Arnhem, N., Sinnige, T., and Veldhuis, L. L., "Validation and comparison of RANS propeller modelling methods for tip-mounted applications," *AIAA journal*, 2019.

[8] Dacles-Mariani, J., Zilliac, G. G., Chow, J. S., and Bradshaw, P., "Numerical/experimental study of a wingtip vortex in the near field," *AIAA journal*, 1995.

[9] Barlow, J. B., Rae, W. H., and Pope, A., *Low-speed wind tunnel testing*, John Wiley & sons, 1999, Chap. 10.

[10] Mozaffari, S., Guilmineau, E., Visonneau, M., and Wackers, J., "Average-based mesh adaptation for hybrid RANS/LES simulation of complex flows," *Computers & Fluids*, 2022.

[11] Frink, N. T., Tormalm, M., and Schmidt, S., "Unstructured CFD Aerodynamic Analysis of a Generic UCAV Configuration," *NATO RTO AVT-189 Specialist Meeting*, 2011, p. 38.

[12] Konishi, K., Kojima, Y., Hashimoto, A., and Kameda, M., "Prediction Accuracy of RANS-based Analysis for Aerodynamic Forces and Moments of a Civil Aircraft Model," *AIAA SCITECH 2023 Forum*, 2023, p. 1758.

[13] Loeser, T., Vicroy, D., and Schuette, A., "SACCON static wind tunnel tests at DNW-NWB and 14 x22 NASA LaRC," *28th AIAA applied aerodynamics conference*, 2010, p. 4393.

[14] Schütte, A., Hummel, D., and Hitzel, S. M., "Flow physics analyses of a generic unmanned combat aerial vehicle configuration," *Journal of Aircraft*, 2012.

Appendix

A. F19 Validation Data

Table 5. F19 simulation conditions

Variable	Symbol	Value	Units
Density	ρ_∞	1.1698	kg/m^3
Airspeed	V_∞	50.8	m/s
Pressure	p_∞	97 767	Pa
Temperature	T_∞	291.2	K
Dynamic viscosity	μ_∞	18.03×10^{-6}	Pa · s
Reference chord	c_{ref}	0.479	m
Reference area	S_{ref}	0.77	m^2
Reynolds number	Re	1.58×10^6	-
Mach number	M	0.149	-

B. Flying V Meshes

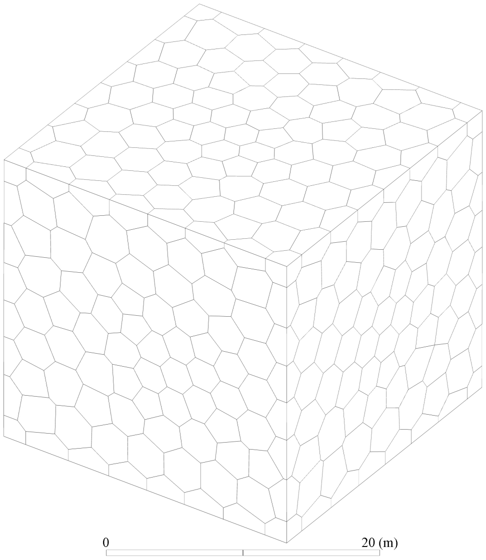

Figure 17. Overview of scaled volume mesh

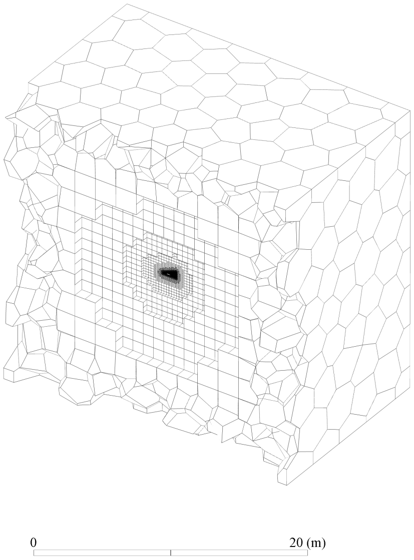

Figure 18. Overview of scaled volume mesh - cut along symmetry plane

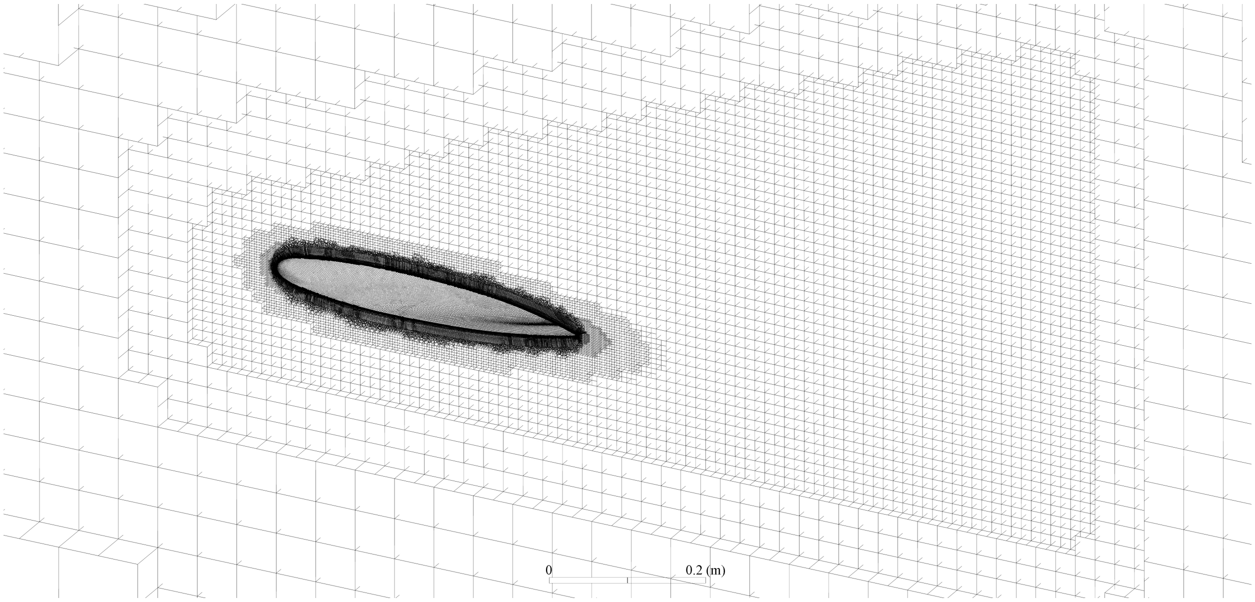

Figure 19. Overview of scaled volume mesh - zoom on body of influence

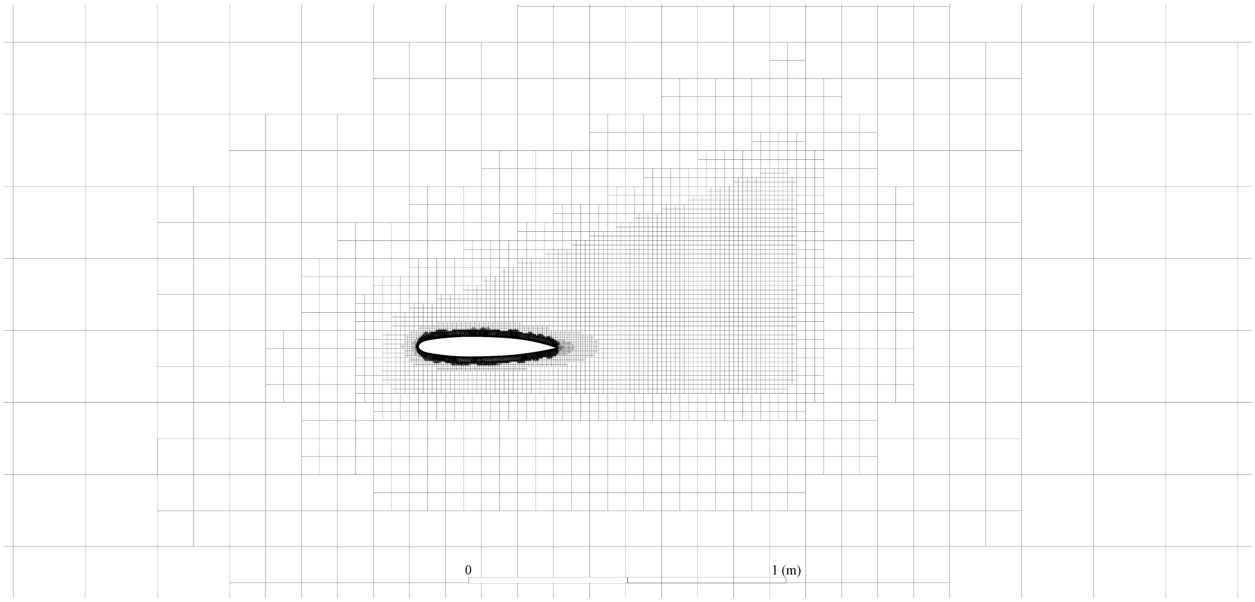

Figure 20. Perpendicular view of scaled volume mesh cut along symmetry plane - far zoom

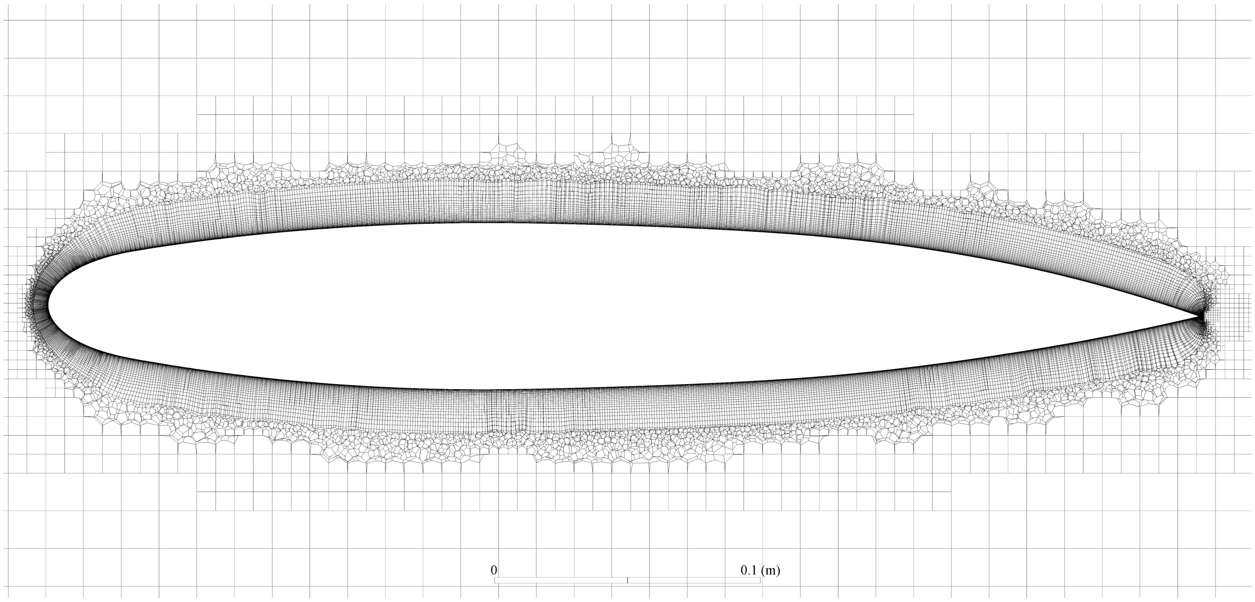

Figure 21. Perpendicular view of scaled volume mesh cut along symmetry plane - close zoom

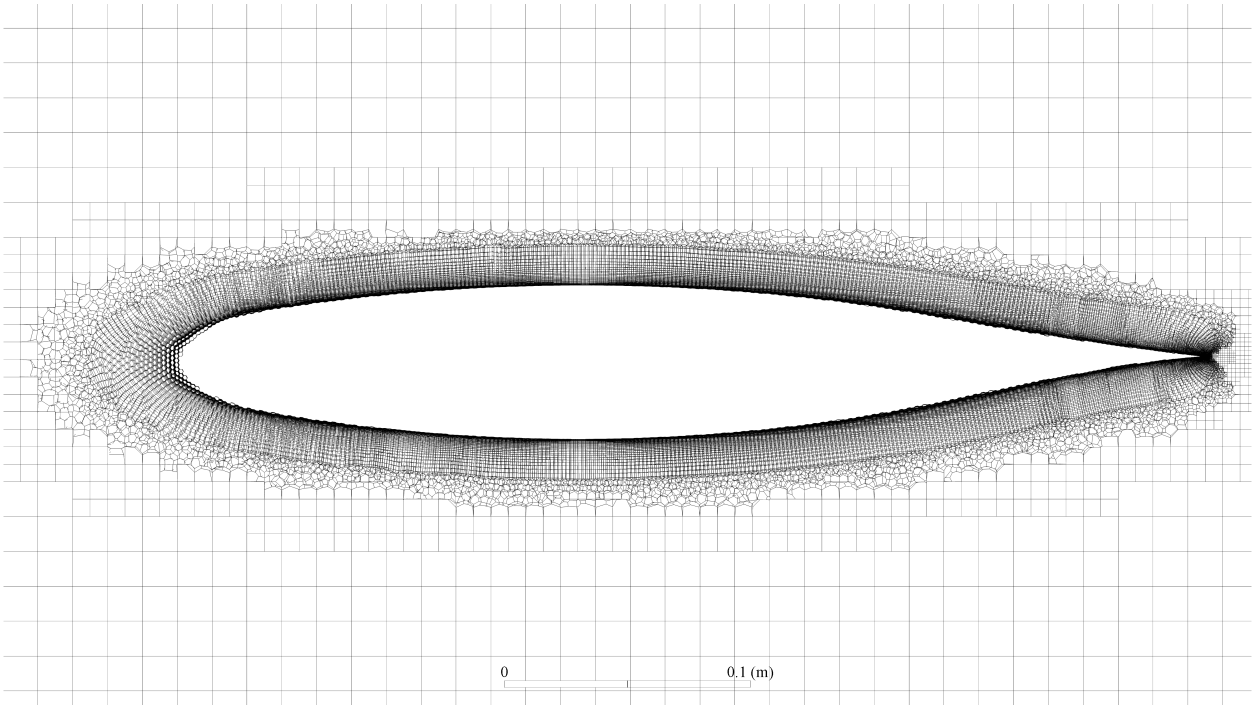

Figure 22. Perpendicular view of scaled volume mesh cut at outer wing - close zoom

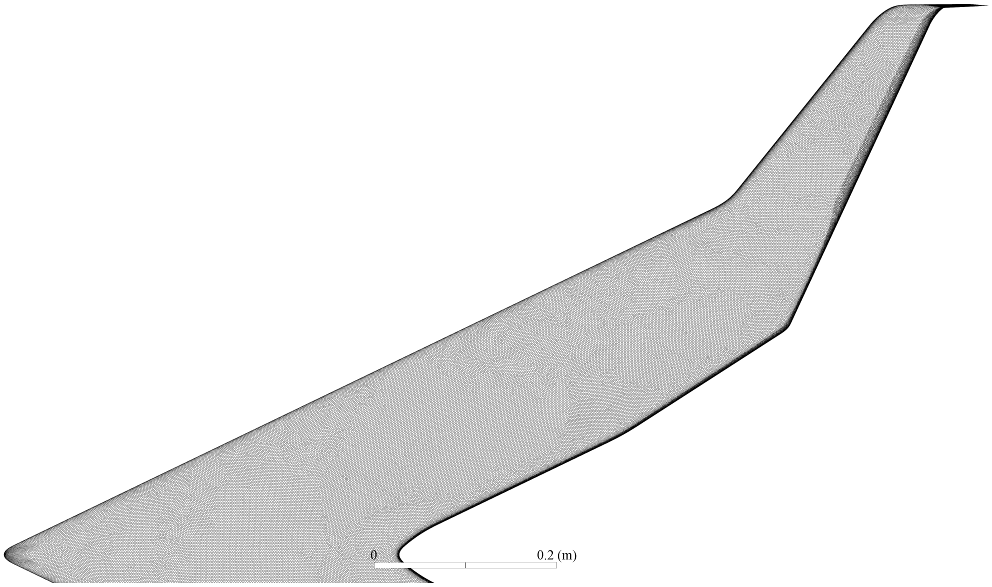

Figure 23. Overview of scaled and wind tunnel surface mesh

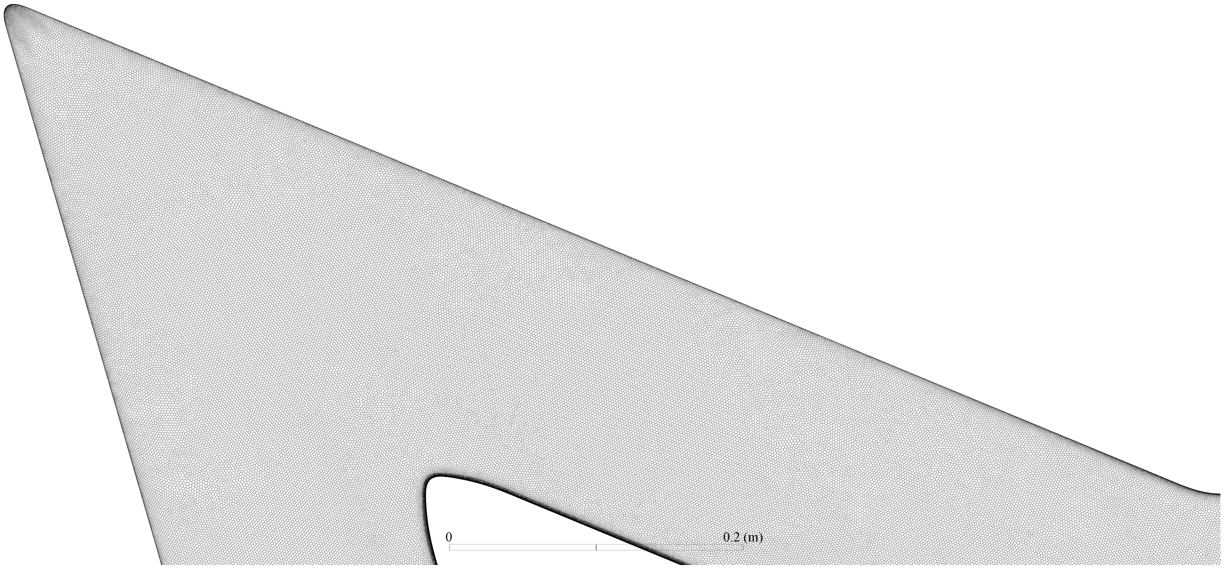

Figure 24. Overview of scaled and wind tunnel surface mesh - zoom on forward section

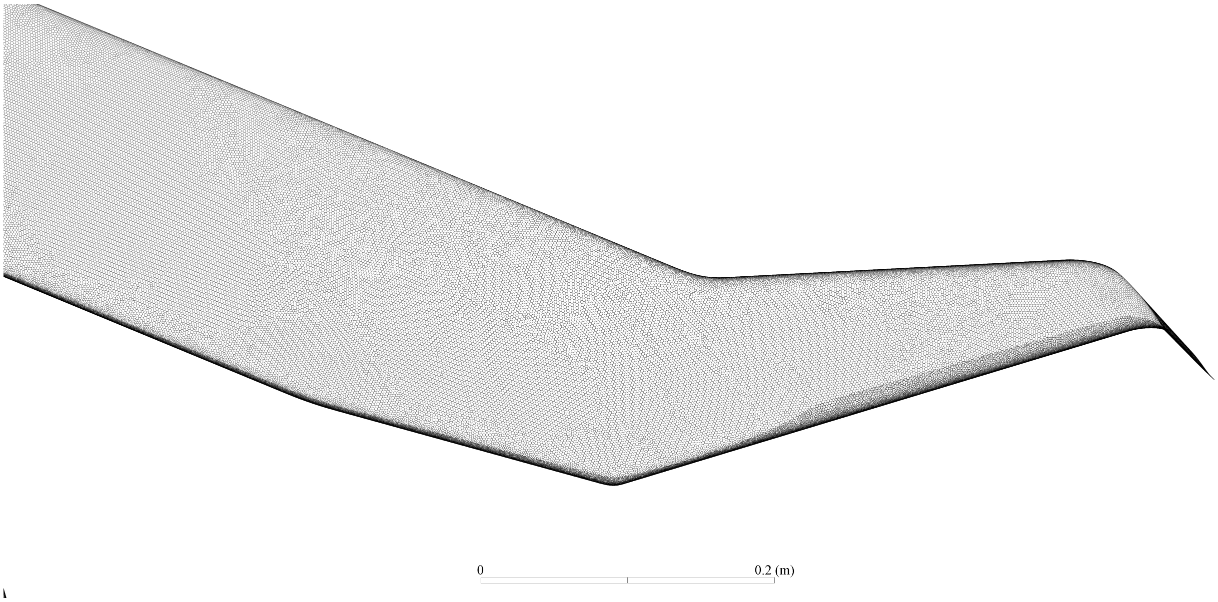

Figure 25. Overview of scaled and wind tunnel surface mesh - zoom on aft section

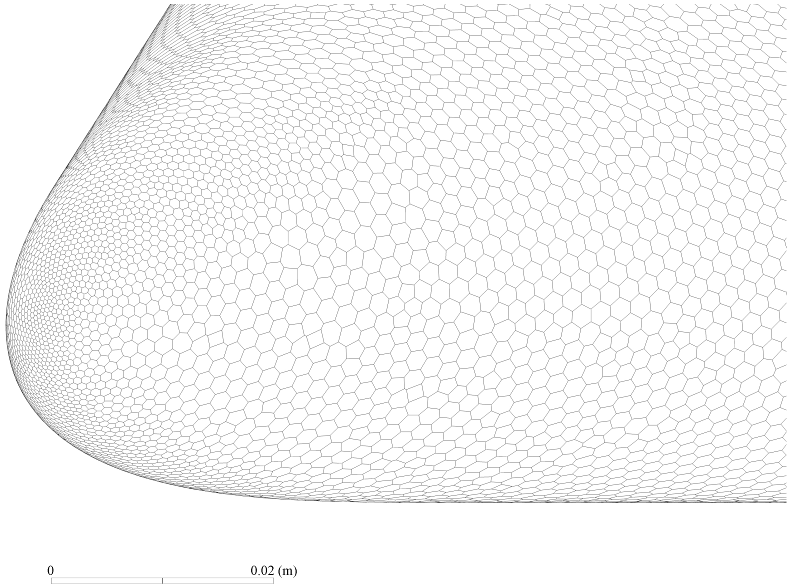

Figure 26. Overview of scaled and wind tunnel surface mesh - zoom on nose

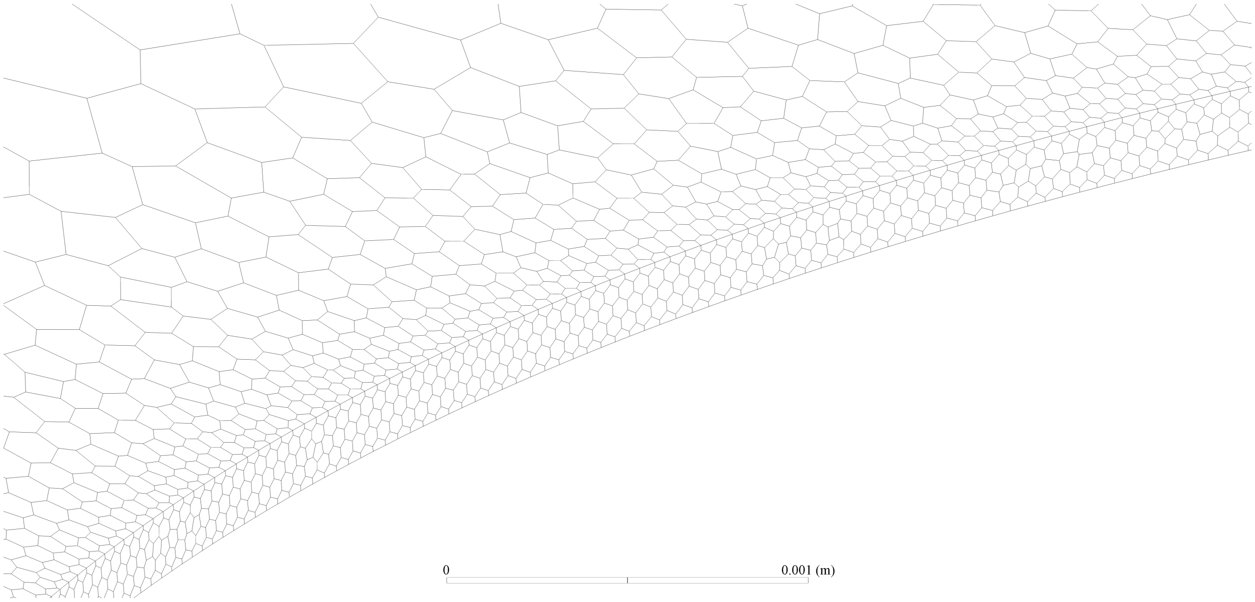

Figure 27. Overview of scaled and wind tunnel surface mesh - zoom on tail

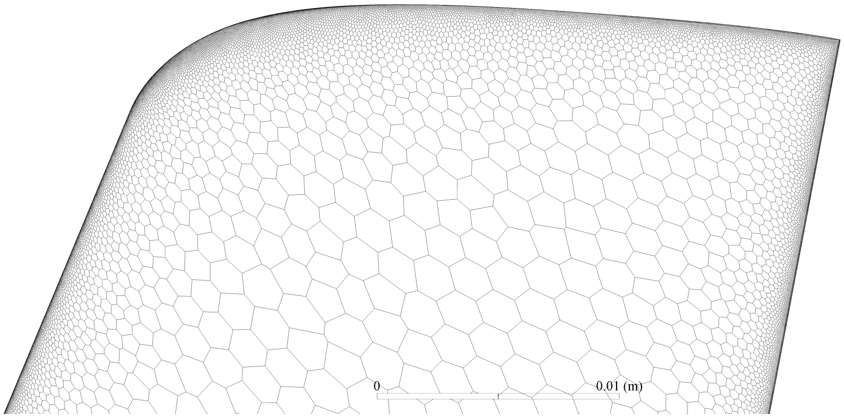

Figure 28. Overview of scaled and wind tunnel surface mesh - zoom on wingtip

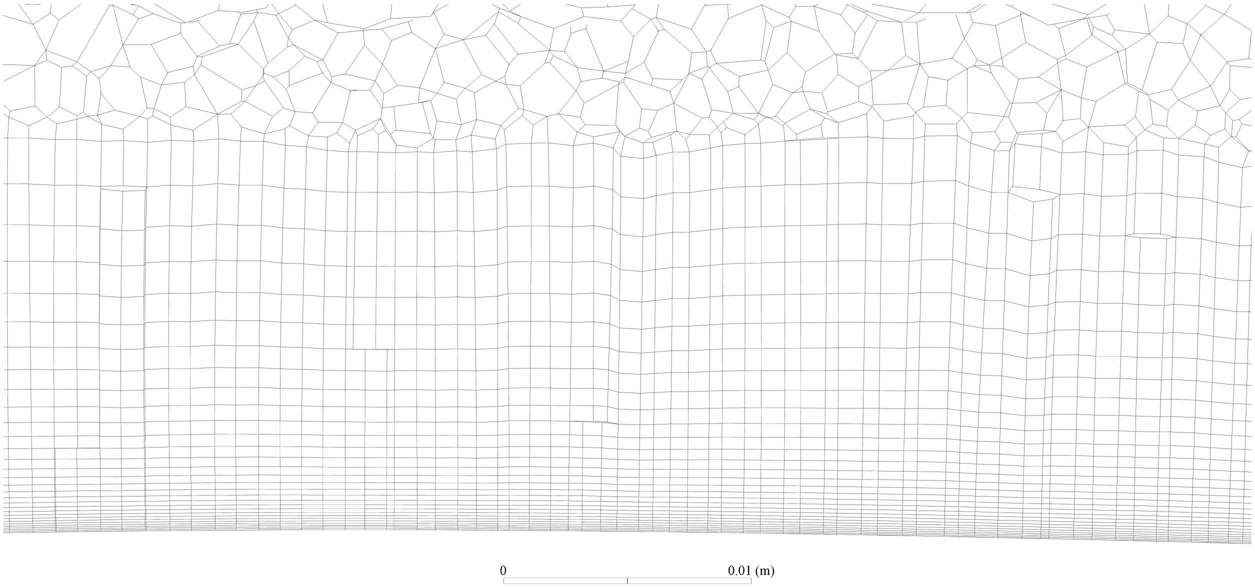

Figure 29. Perpendicular view of scaled mesh inflation layers at centreline

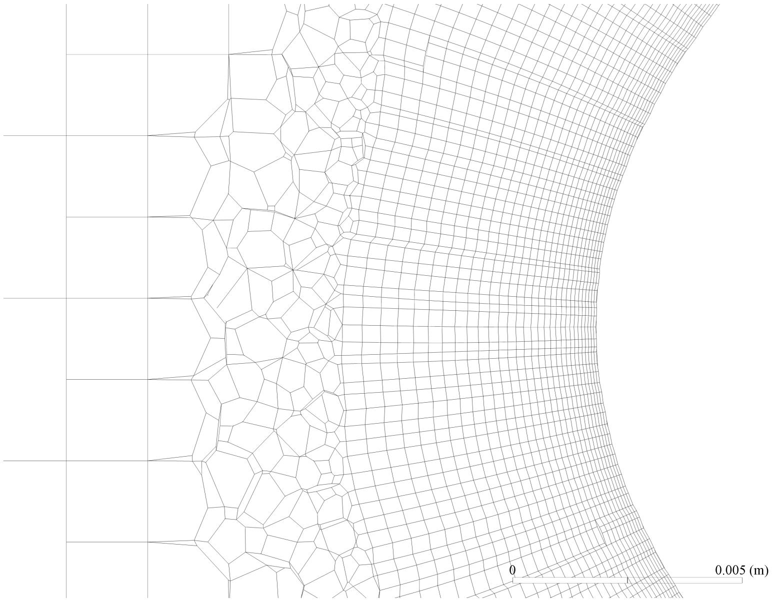

Figure 30. Perpendicular view of scaled mesh inflation layers at centreline - zoom on leading edge

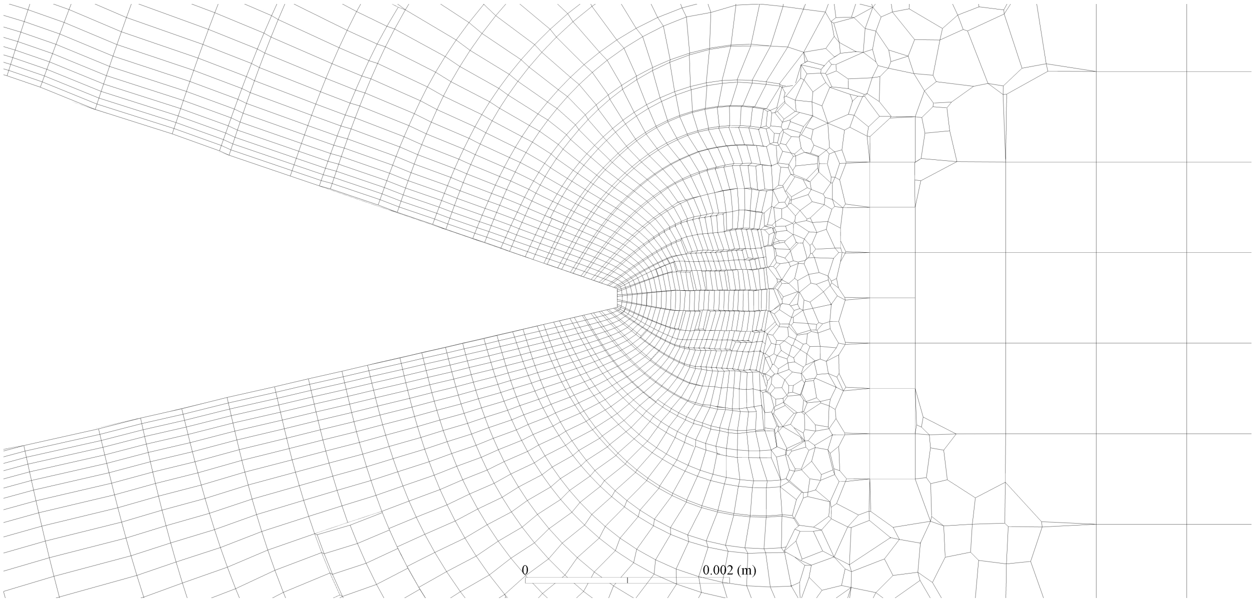

Figure 31. Perpendicular view of scaled mesh inflation layers at centreline - zoom on trailing edge

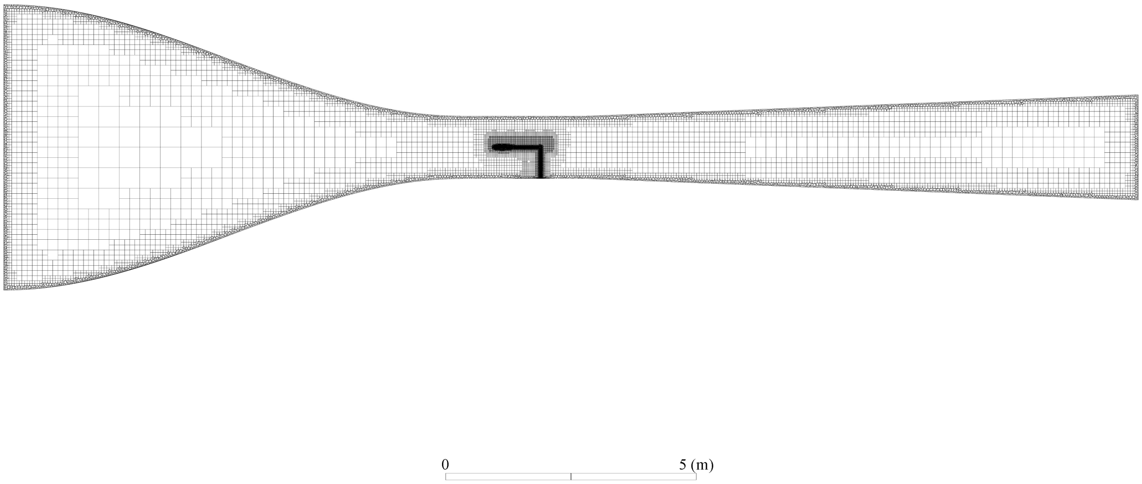

Figure 32. Perpendicular view of wind tunnel volume mesh ($\alpha = 0°, \beta = 0°$) cut along symmetry plane

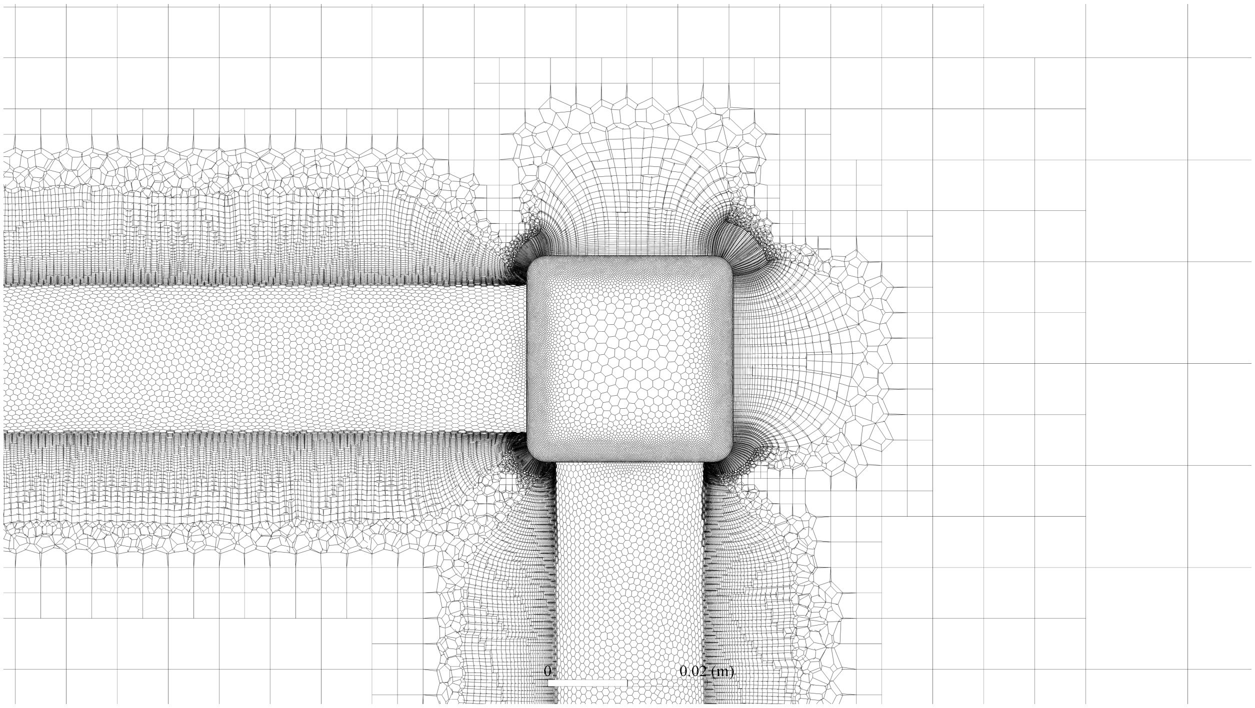

Figure 33. Perpendicular view of wind tunnel volume mesh ($\alpha = 0°, \beta = 0°$) cut along symmetry plane - zoom on aft strut

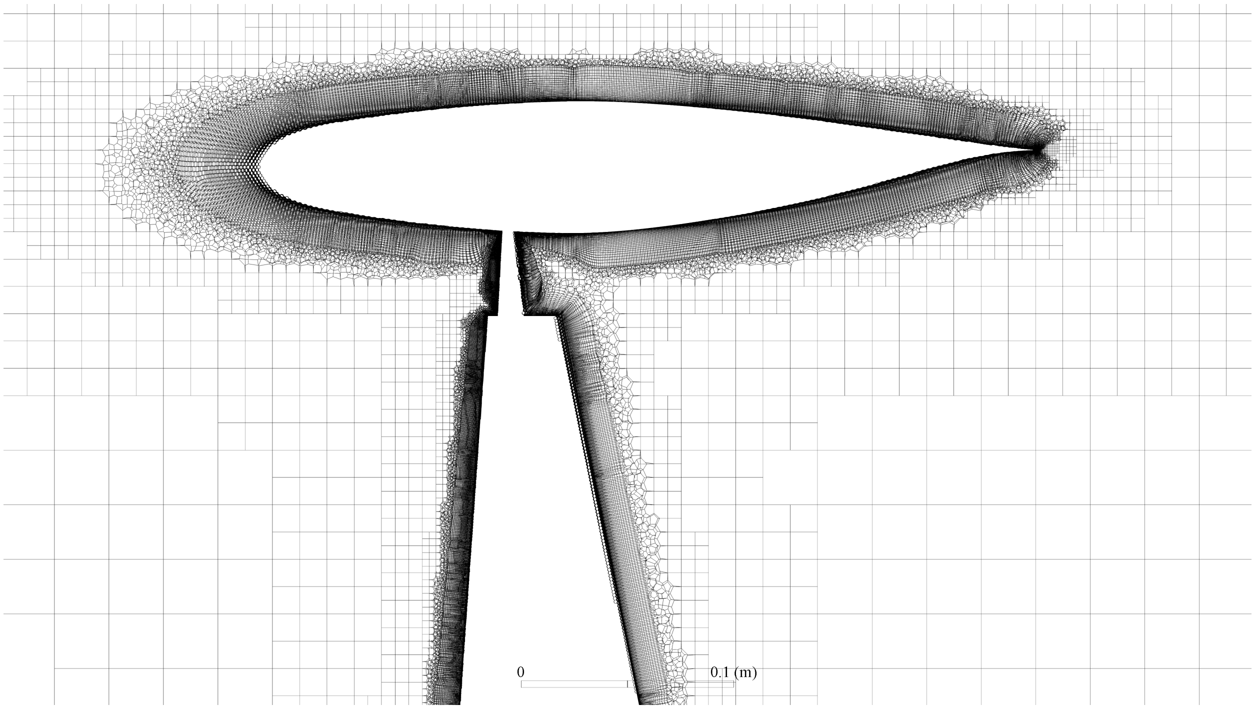

Figure 34. Perpendicular view of wind tunnel volume mesh ($\alpha = 0°, \beta = 0°$) cut along symmetry plane - zoom on upper section of right main strut

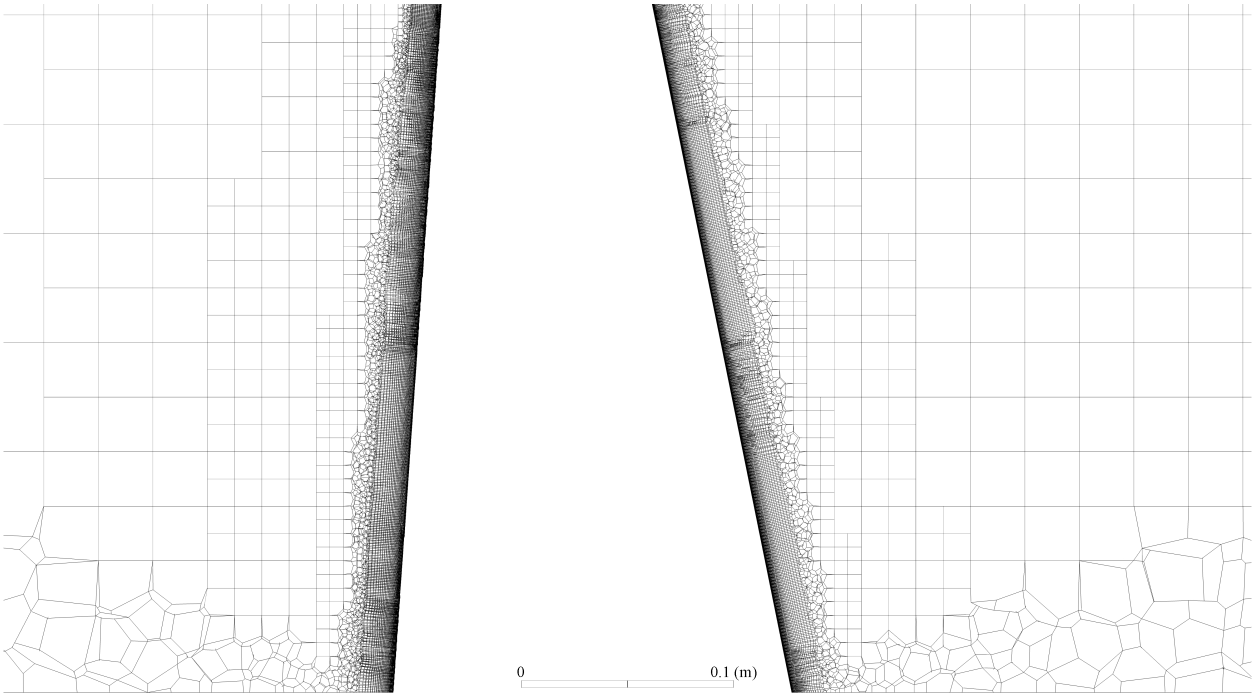

Figure 35. Perpendicular view of wind tunnel volume mesh ($\alpha = 0°, \beta = 0°$) cut along symmetry plane - zoom on lower section of right main strut

C. Force and Moment Polars

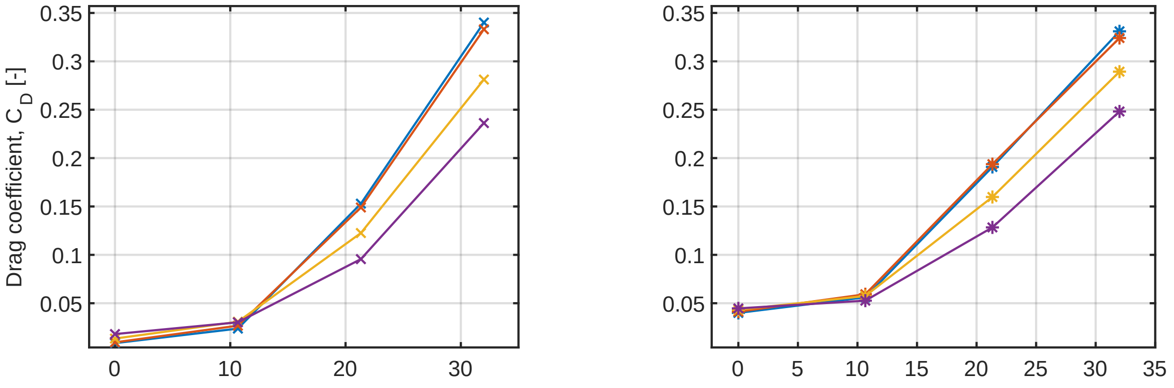

(a) Scaled **(b) Wind tunnel**

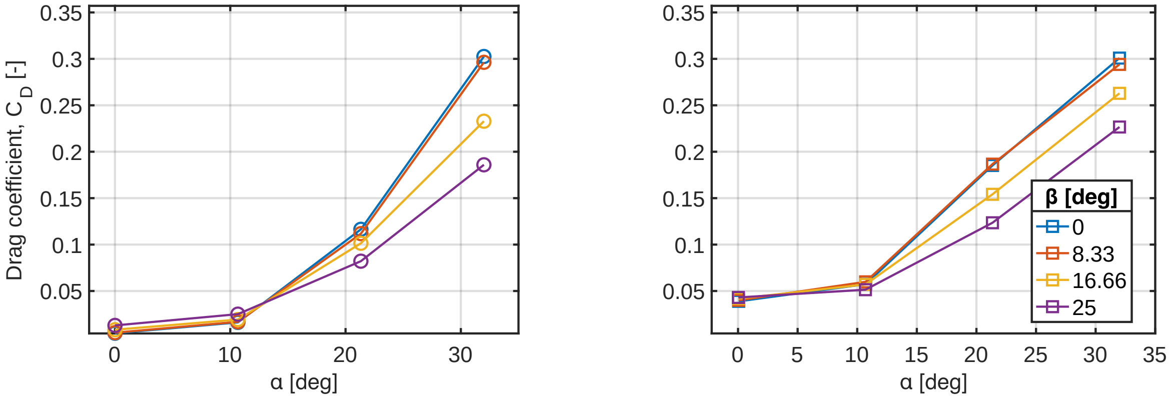

(c) Full-scale **(d) Wind tunnel (corrected)**

Figure 36. Flying V drag coefficient polars

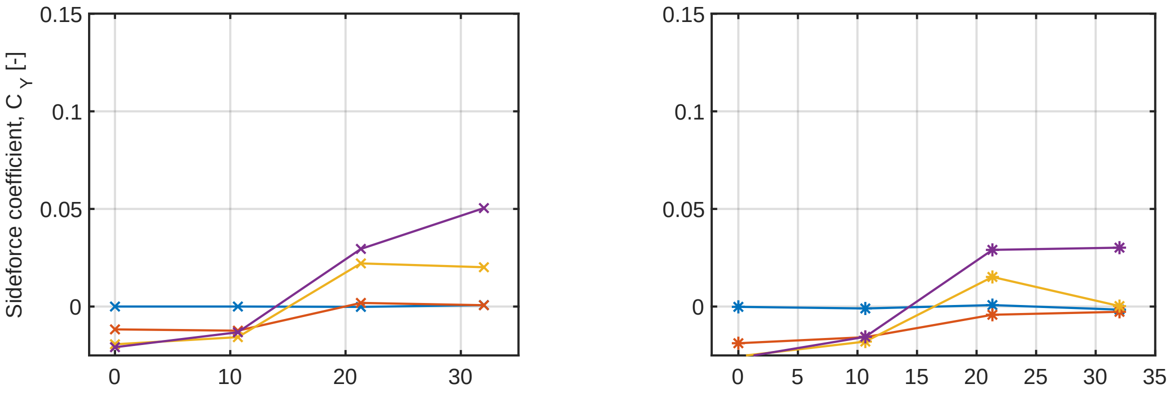

(a) Scaled

(b) Wind tunnel

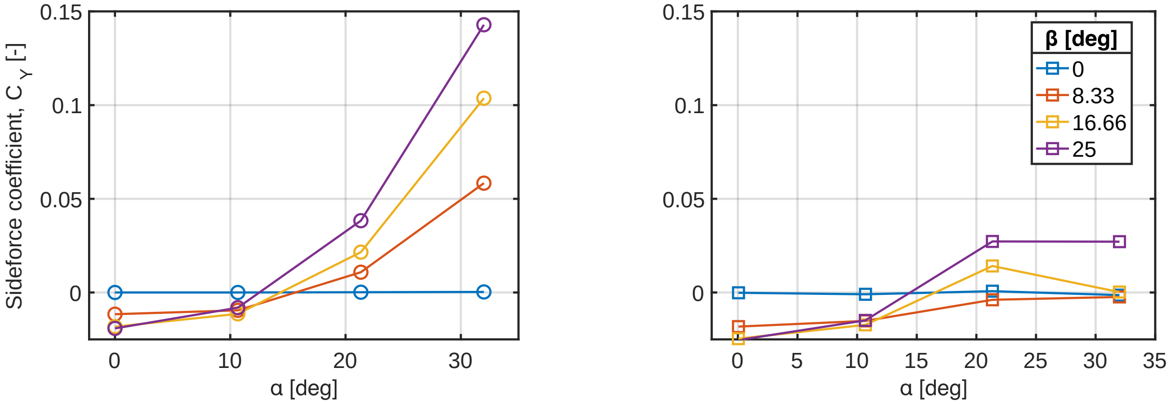

(c) Full-scale

(d) Wind tunnel (corrected)

Figure 37. Flying V sideforce coefficient polars

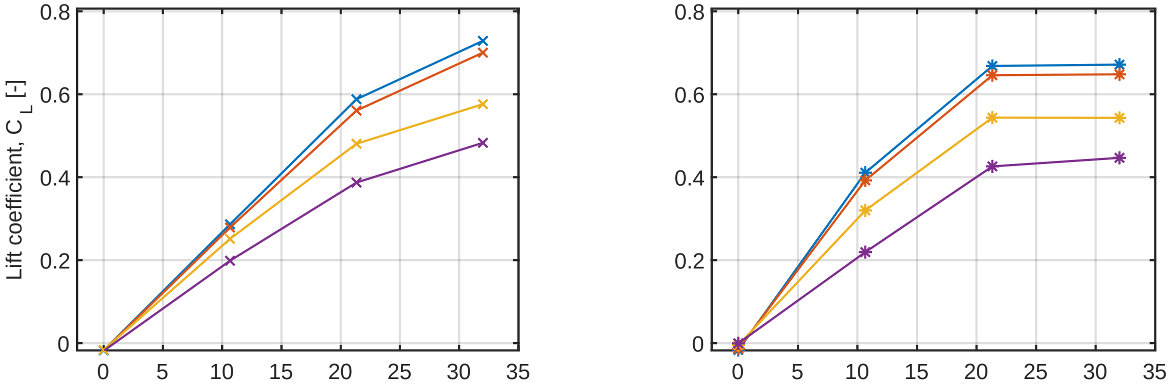

(a) Scaled

(b) Wind tunnel

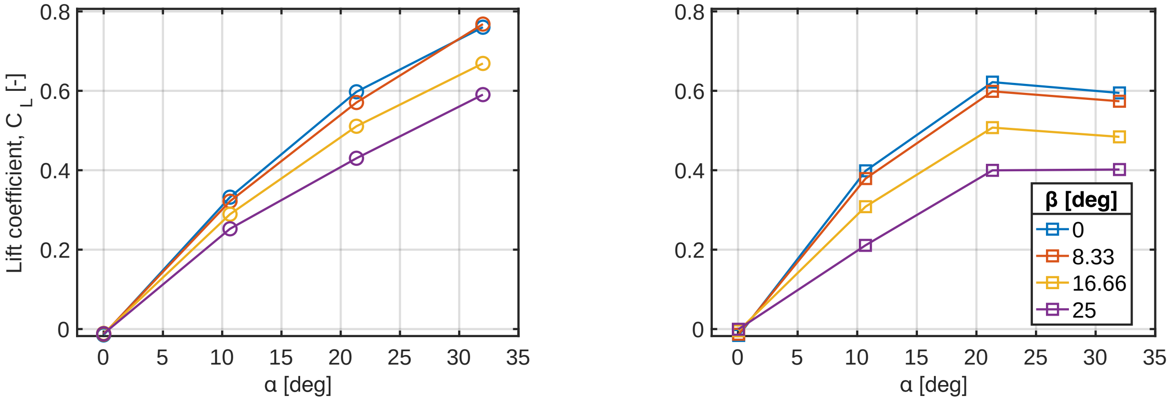

(c) Full-scale

(d) Wind tunnel (corrected)

Figure 38. Flying V lift coefficient polars

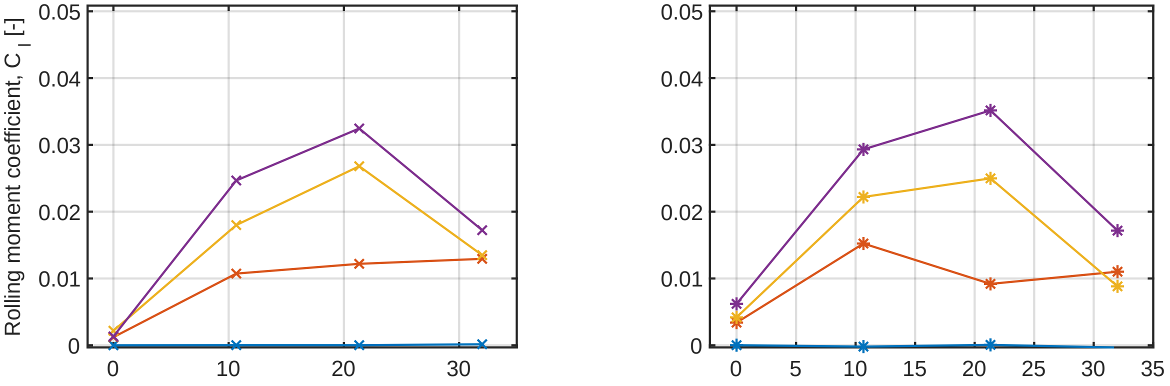

(a) Scaled

(b) Wind tunnel

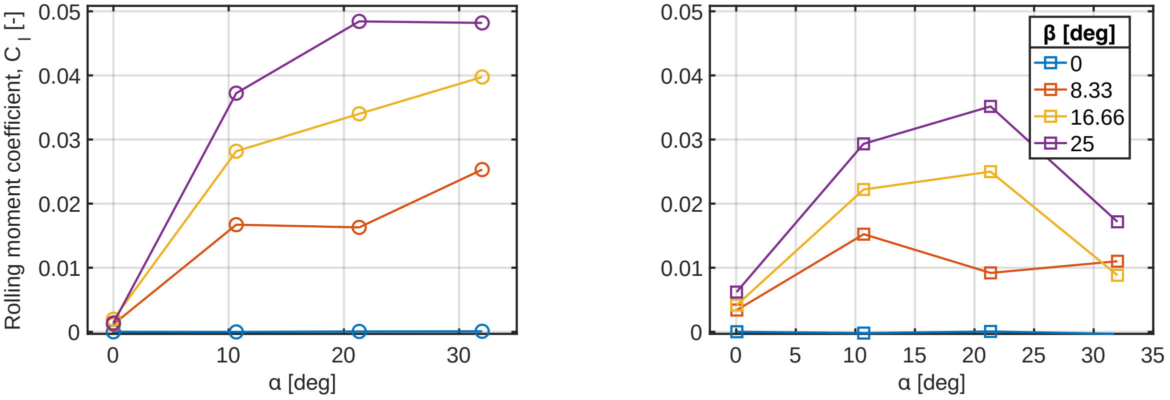

(c) Full-scale

(d) Wind tunnel (corrected)

Figure 39. Flying V rolling moment coefficient polars

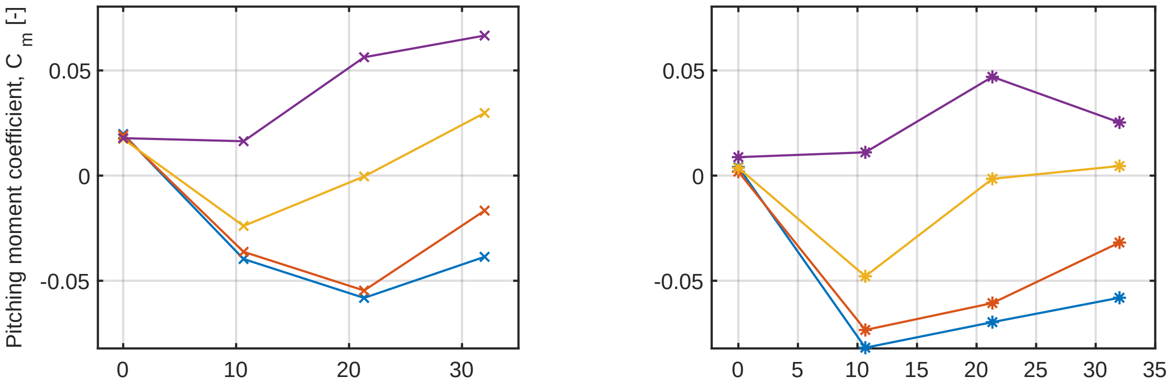

(a) Scaled

(b) Wind tunnel

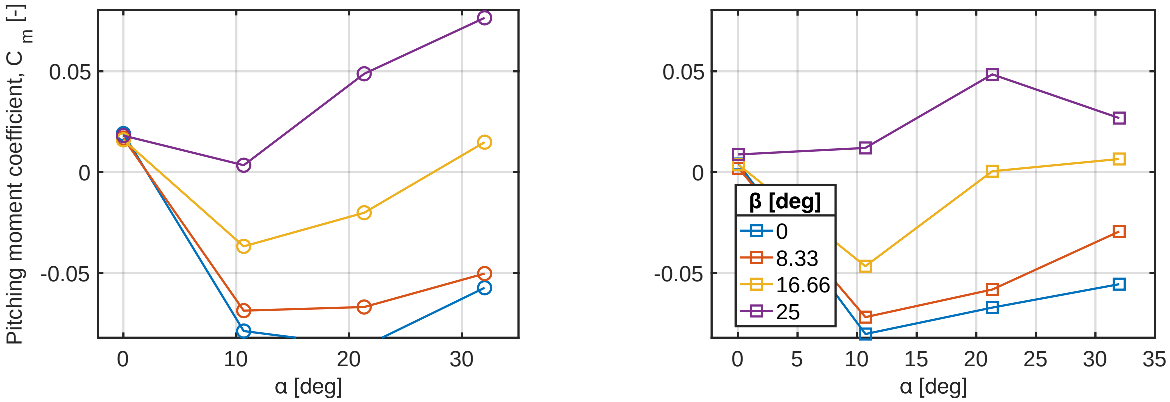

(c) Full-scale

(d) Wind tunnel (corrected)

Figure 40. Flying V pitching moment coefficient polars

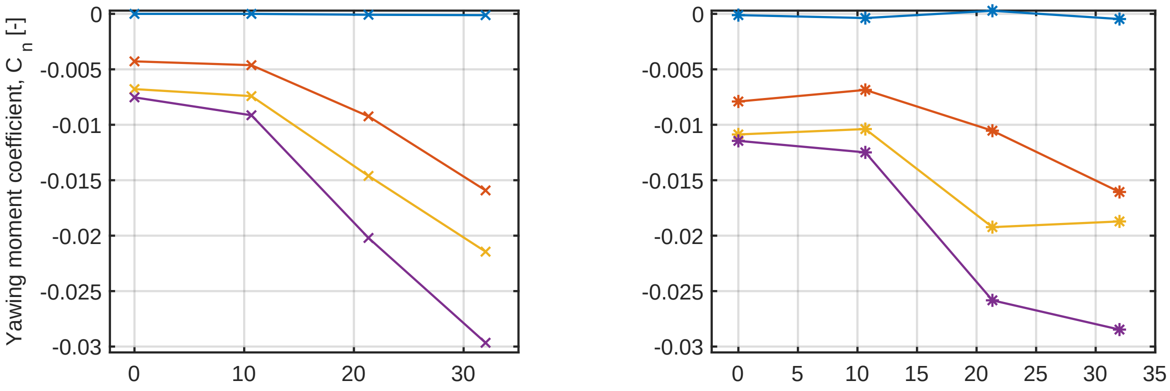

(a) Scaled

(b) Wind tunnel

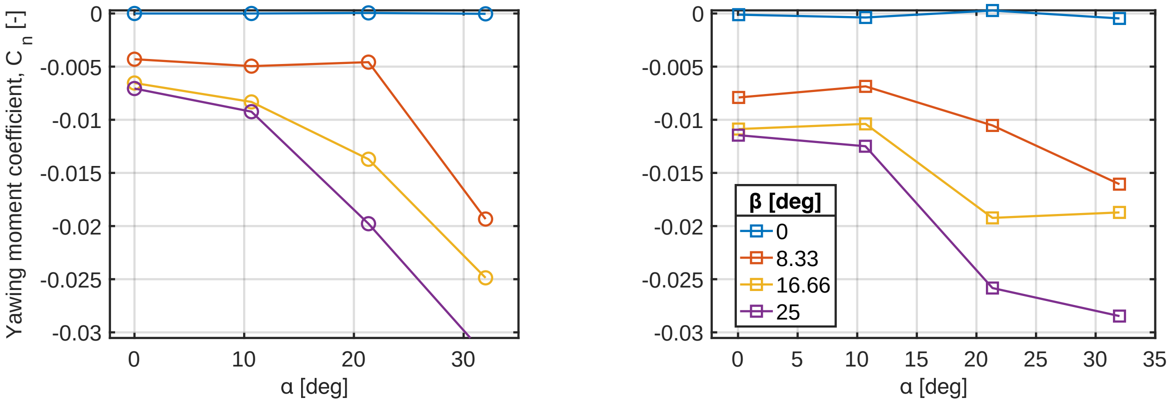

(c) Full-scale

(d) Wind tunnel (corrected)

Figure 41. Flying V yawing moment coefficient polars

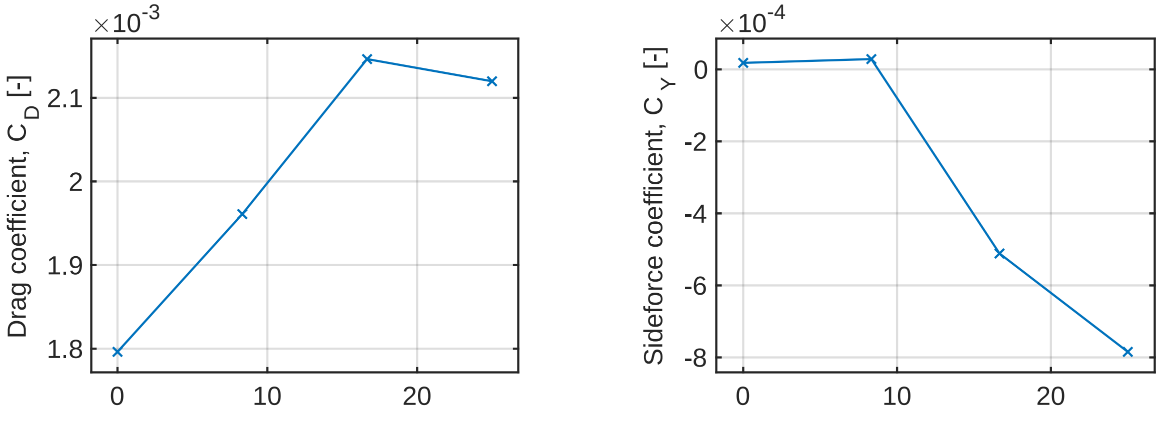

(a) Drag

(b) Sideforce

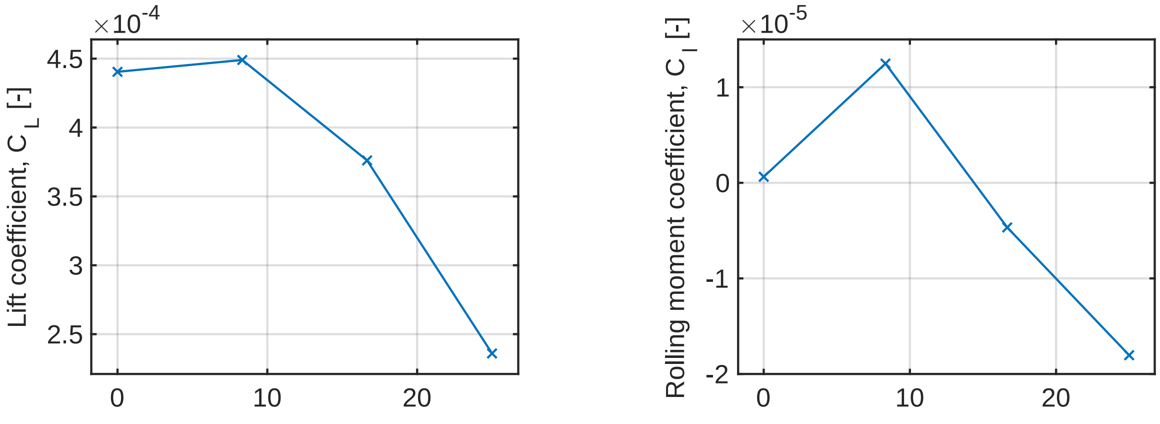

(c) Lift

(d) Rolling moment

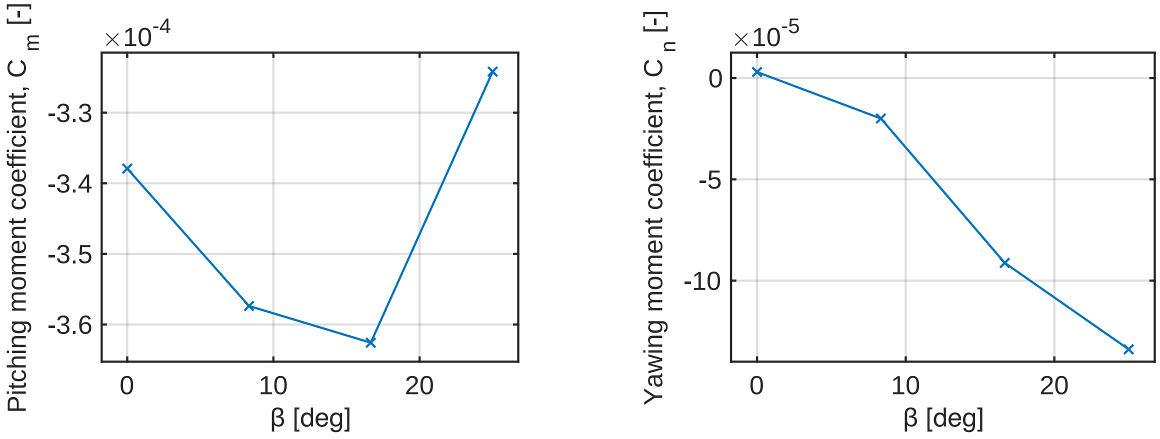

(e) Pitching moment

(f) Yawing moment

Figure 42. LTT strut force and moment coefficient polars

Table 6. Scaled Flying V interpolation validation data

Run	Interpolated coefficient					
	Drag	Sideforce	Lift	Rolling moment	Pitching moment	Yawing moment
1	0.2327	0.0080	0.6321	0.0133	-0.0179	-0.0130
2	0.0088	-0.0029	-0.0179	0.0003	0.0200	-0.0011
3	0.0735	0.0078	0.3650	0.0290	0.0200	-0.0138
4	0.0430	-0.0080	0.3414	0.0101	-0.0368	-0.0039

D. Thin-Plate Spline Coefficients

$$\mathbf{c}\left(\beta,\alpha\right)=\begin{bmatrix} 0^\circ & 0^\circ \\ 0^\circ & 10.66^\circ \\ 0^\circ & 21.33^\circ \\ 0^\circ & 32^\circ \\ 8.33^\circ & 0^\circ \\ 8.33^\circ & 10.66^\circ \\ 8.33^\circ & 21.33^\circ \\ 8.33^\circ & 32^\circ \\ 16.66^\circ & 0^\circ \\ 16.66^\circ & 10.66^\circ \\ 16.66^\circ & 21.33^\circ \\ 16.66^\circ & 32^\circ \\ 25^\circ & 0^\circ \\ 25^\circ & 10.66^\circ \\ 25^\circ & 21.33^\circ \\ 25^\circ & 32^\circ \end{bmatrix} \tag{11}$$

$$\begin{bmatrix} \mathbf{a}_{scaled} \\ \mathbf{a}_{wind\ tunnel} \\ \mathbf{a}_{full\text{-}scale} \end{bmatrix}^{\mathsf{T}}_{C_D}=\begin{bmatrix} 5.2944\times10^{-5} & 5.0290\times10^{-5} & 3.6956\times10^{-5} \\ -1.0637\times10^{-4} & -1.3080\times10^{-4} & -6.2490\times10^{-5} \\ -4.3421\times10^{-5} & -6.6652\times10^{-7} & -7.8447\times10^{-5} \\ 1.7333\times10^{-5} & 9.2261\times10^{-6} & 2.3648\times10^{-5} \\ 2.7131\times10^{-5} & 3.3990\times10^{-5} & 2.3242\times10^{-5} \\ -2.6936\times10^{-5} & -4.9669\times10^{-5} & 1.2130\times10^{-6} \\ 2.8613\times10^{-5} & 1.0740\times10^{-4} & -4.0007\times10^{-5} \\ 1.1102\times10^{-4} & 2.8045\times10^{-5} & 1.6885\times10^{-4} \\ 4.0157\times10^{-6} & 1.5067\times10^{-5} & 7.4955\times10^{-6} \\ -1.0885\times10^{-5} & -3.6594\times10^{-5} & -3.9519\times10^{-5} \\ -1.4765\times10^{-5} & -1.2169\times10^{-5} & 2.5033\times10^{-5} \\ -1.9501\times10^{-5} & 9.9937\times10^{-6} & -5.8623\times10^{-5} \\ 5.2188\times10^{-5} & 5.1843\times10^{-5} & 4.3261\times10^{-5} \\ -1.6012\times10^{-5} & -4.1470\times10^{-5} & -9.1178\times10^{-6} \\ -5.8726\times10^{-5} & -3.0920\times10^{-5} & -1.9508\times10^{-5} \\ 3.3730\times10^{-6} & -3.5623\times10^{-6} & -2.1991\times10^{-5} \\ -1.6029\times10^{-3} & -1.3001\times10^{-3} & -1.8576\times10^{-3} \\ 8.1568\times10^{-3} & 6.5849\times10^{-3} & 7.1378\times10^{-3} \\ -3.1933\times10^{-1} & -1.8520\times10^{-1} & -2.8673\times10^{-1} \end{bmatrix} \tag{12}$$

$$\begin{bmatrix} \mathbf{a}_{scaled} \\ \mathbf{a}_{wind\ tunnel} \\ \mathbf{a}_{full\text{-}scale} \end{bmatrix}^{\mathsf{T}}_{C_Y} = \begin{bmatrix}
1.0579 \times 10^{-5} & 2.2901 \times 10^{-5} & 3.3635 \times 10^{-5} \\
1.7823 \times 10^{-5} & 9.6539 \times 10^{-6} & 1.9944 \times 10^{-5} \\
1.2143 \times 10^{-6} & 1.5508 \times 10^{-5} & 3.9851 \times 10^{-5} \\
1.2832 \times 10^{-5} & -5.5646 \times 10^{-6} & -9.9037 \times 10^{-5} \\
1.1140 \times 10^{-6} & -1.9918 \times 10^{-5} & -1.4531 \times 10^{-5} \\
-2.8085 \times 10^{-5} & -2.1446 \times 10^{-5} & -3.0523 \times 10^{-5} \\
-1.3507 \times 10^{-5} & -3.6583 \times 10^{-5} & -1.2421 \times 10^{-5} \\
-3.3051 \times 10^{-5} & 2.5270 \times 10^{-5} & 5.9504 \times 10^{-5} \\
1.0733 \times 10^{-5} & 1.4466 \times 10^{-5} & 1.0806 \times 10^{-5} \\
-3.0291 \times 10^{-5} & -1.8995 \times 10^{-5} & 2.3176 \times 10^{-5} \\
8.5630 \times 10^{-5} & 7.6308 \times 10^{-5} & -3.1469 \times 10^{-5} \\
-4.6340 \times 10^{-5} & -9.3883 \times 10^{-5} & 1.0238 \times 10^{-5} \\
7.0439 \times 10^{-6} & 6.1690 \times 10^{-6} & -1.5472 \times 10^{-6} \\
-4.4551 \times 10^{-5} & -5.7869 \times 10^{-5} & -1.8343 \times 10^{-5} \\
8.4932 \times 10^{-6} & 5.1246 \times 10^{-5} & -6.9531 \times 10^{-5} \\
4.0365 \times 10^{-5} & 3.2736 \times 10^{-5} & 8.0247 \times 10^{-5} \\
4.0803 \times 10^{-4} & 3.2621 \times 10^{-5} & 2.5573 \times 10^{-3} \\
7.0007 \times 10^{-4} & 3.4995 \times 10^{-4} & 2.5966 \times 10^{-3} \\
-7.5802 \times 10^{-2} & -5.5565 \times 10^{-2} & -1.7439 \times 10^{-1}
\end{bmatrix} \tag{13}$$

$$\begin{bmatrix} \mathbf{a}_{scaled} \\ \mathbf{a}_{wind\ tunnel} \\ \mathbf{a}_{full\text{-}scale} \end{bmatrix}^{\mathsf{T}}_{C_L} = \begin{bmatrix}
-5.7081 \times 10^{-5} & -1.6920 \times 10^{-4} & -8.5425 \times 10^{-5} \\
-6.0031 \times 10^{-5} & 1.0423 \times 10^{-4} & 5.3275 \times 10^{-5} \\
1.3553 \times 10^{-4} & 1.5214 \times 10^{-4} & 9.2603 \times 10^{-5} \\
-1.2291 \times 10^{-4} & -1.7355 \times 10^{-4} & -1.6748 \times 10^{-4} \\
-3.0109 \times 10^{-6} & -7.7319 \times 10^{-5} & -2.9924 \times 10^{-5} \\
-2.3543 \times 10^{-5} & 5.3812 \times 10^{-5} & 5.5182 \times 10^{-5} \\
8.3721 \times 10^{-5} & 1.3298 \times 10^{-4} & -4.8393 \times 10^{-5} \\
1.7113 \times 10^{-4} & 7.8872 \times 10^{-5} & 2.4913 \times 10^{-4} \\
-4.1926 \times 10^{-5} & -5.9076 \times 10^{-5} & -4.3224 \times 10^{-5} \\
7.1271 \times 10^{-6} & 1.7086 \times 10^{-5} & -3.5337 \times 10^{-6} \\
6.7360 \times 10^{-5} & 6.8476 \times 10^{-5} & 5.1222 \times 10^{-5} \\
-1.7566 \times 10^{-4} & -1.4400 \times 10^{-4} & -1.3535 \times 10^{-4} \\
6.7792 \times 10^{-5} & 1.3951 \times 10^{-4} & 2.6137 \times 10^{-5} \\
-4.4438 \times 10^{-5} & -1.7880 \times 10^{-4} & 7.3989 \times 10^{-5} \\
5.7805 \times 10^{-5} & 1.5186 \times 10^{-4} & -5.6072 \times 10^{-5} \\
-6.1865 \times 10^{-5} & -9.7013 \times 10^{-5} & -3.2128 \times 10^{-5} \\
-4.1928 \times 10^{-3} & -3.3224 \times 10^{-3} & -2.5735 \times 10^{-3} \\
1.7830 \times 10^{-2} & 1.5918 \times 10^{-2} & 2.1515 \times 10^{-2} \\
5.7557 \times 10^{-1} & 1.0830 & 5.3757 \times 10^{-1}
\end{bmatrix} \tag{14}$$

$$\begin{bmatrix} \mathbf{a}_{scaled} \\ \mathbf{a}_{wind\ tunnel} \\ \mathbf{a}_{full\text{-}scale} \end{bmatrix}_{C_l}^{\mathsf{T}} = \begin{bmatrix} 1.4102\times10^{-5} & 1.4269\times10^{-5} & 2.7058\times10^{-5} \\ -1.0977\times10^{-5} & -2.3357\times10^{-5} & -2.1142\times10^{-5} \\ -3.0545\times10^{-6} & 7.1167\times10^{-6} & 7.9771\times10^{-6} \\ -1.1637\times10^{-5} & -1.2657\times10^{-5} & -2.7352\times10^{-5} \\ -8.1201\times10^{-6} & -5.8847\times10^{-6} & -1.5125\times10^{-5} \\ 1.3926\times10^{-5} & 3.6863\times10^{-5} & 2.4486\times10^{-5} \\ -1.9016\times10^{-5} & -3.8502\times10^{-5} & -2.2682\times10^{-5} \\ 3.6097\times10^{-5} & 4.9319\times10^{-5} & 3.3554\times10^{-5} \\ 4.5622\times10^{-6} & -7.9287\times10^{-6} & -7.9779\times10^{-7} \\ -1.2839\times10^{-5} & -7.9842\times10^{-6} & 8.4740\times10^{-6} \\ 2.5952\times10^{-5} & 2.0558\times10^{-5} & -1.3432\times10^{-5} \\ -2.8746\times10^{-5} & -4.4337\times10^{-5} & 5.6579\times10^{-6} \\ -2.2881\times10^{-5} & -1.8046\times10^{-5} & -3.3761\times10^{-5} \\ 1.7635\times10^{-5} & 1.4303\times10^{-5} & 3.0641\times10^{-5} \\ 1.7630\times10^{-5} & 2.3932\times10^{-5} & 1.1073\times10^{-5} \\ -1.2632\times10^{-5} & -7.6641\times10^{-6} & -1.4629\times10^{-5} \\ 3.8315\times10^{-4} & 5.7555\times10^{-4} & 9.8471\times10^{-4} \\ 1.7604\times10^{-4} & 1.9964\times10^{-4} & 8.5723\times10^{-4} \\ 6.5520\times10^{-2} & 5.9745\times10^{-2} & 5.7274\times10^{-2} \end{bmatrix} \tag{15}$$

$$\begin{bmatrix} \mathbf{a}_{scaled} \\ \mathbf{a}_{wind\ tunnel} \\ \mathbf{a}_{full\text{-}scale} \end{bmatrix}_{C_m}^{\mathsf{T}} = \begin{bmatrix} 3.9064\times10^{-5} & 7.4163\times10^{-5} & 8.3145\times10^{-5} \\ -3.2925\times10^{-5} & -1.1095\times10^{-4} & -8.8254\times10^{-5} \\ 2.3792\times10^{-5} & 7.9886\times10^{-5} & -2.3813\times10^{-6} \\ 1.2799\times10^{-5} & -7.1885\times10^{-6} & 7.4149\times10^{-5} \\ 1.7817\times10^{-5} & 3.0852\times10^{-5} & 3.0517\times10^{-5} \\ 1.8505\times10^{-5} & -2.4742\times10^{-5} & -6.4303\times10^{-5} \\ -1.0590\times10^{-4} & -8.1892\times10^{-5} & 3.8681\times10^{-5} \\ -1.1096\times10^{-5} & 2.1984\times10^{-6} & -1.2557\times10^{-4} \\ 4.7157\times10^{-5} & 6.1065\times10^{-5} & 4.2303\times10^{-5} \\ -8.8340\times10^{-5} & -1.4542\times10^{-4} & -2.1616\times10^{-5} \\ 3.2460\times10^{-5} & 9.3278\times10^{-5} & -3.2129\times10^{-5} \\ 4.1890\times10^{-5} & 3.0501\times10^{-5} & 5.2835\times10^{-5} \\ -4.1748\times10^{-5} & -6.1003\times10^{-5} & -4.0879\times10^{-5} \\ -6.4191\times10^{-6} & 3.3272\times10^{-5} & -4.1378\times10^{-5} \\ 8.1197\times10^{-5} & 8.9272\times10^{-5} & 8.1783\times10^{-5} \\ -2.8251\times10^{-5} & -6.3294\times10^{-5} & 1.3099\times10^{-5} \\ 1.7684\times10^{-3} & 1.3986\times10^{-3} & 2.2566\times10^{-3} \\ -4.6686\times10^{-4} & -2.0422\times10^{-3} & -9.1021\times10^{-4} \\ -1.9317\times10^{-1} & -1.4937\times10^{-1} & -3.3117\times10^{-1} \end{bmatrix} \tag{16}$$

$$\begin{bmatrix} \mathbf{a}_{scaled} \\ \mathbf{a}_{wind\ tunnel} \\ \mathbf{a}_{full\text{-}scale} \end{bmatrix}^{\mathsf{T}}_{C_n} = \begin{bmatrix} -2.4072\times10^{-6} & 3.9663\times10^{-6} & -2.5155\times10^{-6} \\ -2.5834\times10^{-6} & -5.1150\times10^{-6} & -1.6760\times10^{-7} \\ -1.4932\times10^{-7} & 3.4782\times10^{-6} & -1.6495\times10^{-5} \\ 2.0450\times10^{-5} & 1.7591\times10^{-5} & 3.2944\times10^{-5} \\ -5.1550\times10^{-7} & -8.1678\times10^{-6} & 4.5218\times10^{-7} \\ 3.9815\times10^{-6} & 3.4561\times10^{-6} & -4.7304\times10^{-6} \\ -2.5580\times10^{-6} & 3.7870\times10^{-6} & 3.2655\times10^{-5} \\ -2.9778\times10^{-5} & -3.9442\times10^{-5} & -4.8769\times10^{-5} \\ -7.0993\times10^{-6} & -7.8334\times10^{-6} & -4.2022\times10^{-6} \\ 6.0578\times10^{-9} & 6.1204\times10^{-6} & -7.0124\times10^{-6} \\ 1.8713\times10^{-6} & -1.1862\times10^{-5} & -4.9806\times10^{-6} \\ 1.7033\times10^{-5} & 3.4547\times10^{-5} & 1.5690\times10^{-5} \\ 2.1764\times10^{-6} & 2.1925\times10^{-6} & 1.6357\times10^{-6} \\ 1.3604\times10^{-5} & 2.0923\times10^{-5} & 1.3835\times10^{-5} \\ -5.6517\times10^{-6} & -1.6654\times10^{-5} & -1.1435\times10^{-6} \\ -8.3808\times10^{-6} & -6.9867\times10^{-6} & -7.1955\times10^{-6} \\ -8.2689\times10^{-4} & -9.0159\times10^{-4} & -8.2862\times10^{-4} \\ -2.6639\times10^{-4} & -1.4134\times10^{-4} & -3.9386\times10^{-4} \\ 2.1489\times10^{-3} & -1.0597\times10^{-2} & 5.4531\times10^{-3} \end{bmatrix} \tag{17}$$

E. Surrogate Model for Corrections

$$\begin{bmatrix}\mathbf{a}_{walls}\\ \mathbf{a}_{Re}\end{bmatrix}^{\mathsf{T}}_{\Delta C_D} = \begin{bmatrix} 2.6544\times10^{-6} & -1.5988\times10^{-5}\\ 2.4430\times10^{-5} & 4.3880\times10^{-5}\\ -4.2755\times10^{-5} & -3.5026\times10^{-5}\\ 8.1071\times10^{-6} & 6.3151\times10^{-6}\\ -6.8588\times10^{-6} & -3.8892\times10^{-6}\\ 2.2733\times10^{-5} & 2.8149\times10^{-5}\\ -7.8784\times10^{-5} & -6.8620\times10^{-5}\\ 8.2975\times10^{-5} & 5.7835\times10^{-5}\\ -1.1051\times10^{-5} & 3.4798\times10^{-6}\\ 2.5708\times10^{-5} & -2.8634\times10^{-5}\\ -2.5961\times10^{-6} & 3.9798\times10^{-5}\\ -2.9495\times10^{-5} & -3.9121\times10^{-5}\\ 3.4526\times10^{-7} & -8.9268\times10^{-6}\\ 2.5458\times10^{-5} & 6.8944\times10^{-6}\\ -2.7806\times10^{-5} & 3.9218\times10^{-5}\\ 6.9353\times10^{-6} & -2.5364\times10^{-5}\\ -3.0286\times10^{-4} & -2.5470\times10^{-4}\\ 1.5719\times10^{-3} & -1.0190\times10^{-3}\\ -1.3413\times10^{-1} & 3.2608\times10^{-2} \end{bmatrix} \tag{18}$$

$$\begin{bmatrix}\mathbf{a}_{walls}\\ \mathbf{a}_{Re}\end{bmatrix}^{\mathsf{T}}_{\Delta C_Y} = \begin{bmatrix}
-1.2322\times10^{-5} & 2.3056\times10^{-5}\\
8.1688\times10^{-6} & 2.1217\times10^{-6}\\
-1.4294\times10^{-5} & 3.8637\times10^{-5}\\
1.8396\times10^{-5} & -1.1187\times10^{-4}\\
2.1032\times10^{-5} & -1.5645\times10^{-5}\\
-6.6390\times10^{-6} & -2.4378\times10^{-6}\\
2.3076\times10^{-5} & 1.0862\times10^{-6}\\
-5.8321\times10^{-5} & 9.2555\times10^{-5}\\
-3.7339\times10^{-6} & 7.3751\times10^{-8}\\
-1.1297\times10^{-5} & 5.3467\times10^{-5}\\
9.3215\times10^{-6} & -1.1710\times10^{-4}\\
4.7543\times10^{-5} & 5.6578\times10^{-5}\\
8.7496\times10^{-7} & -8.5911\times10^{-6}\\
1.3318\times10^{-5} & 2.6208\times10^{-5}\\
-4.2753\times10^{-5} & -7.8024\times10^{-5}\\
7.6295\times10^{-6} & 3.9882\times10^{-5}\\
3.7541\times10^{-4} & 2.1493\times10^{-3}\\
3.5012\times10^{-4} & 1.8965\times10^{-3}\\
-2.0237\times10^{-2} & -9.8585\times10^{-2}
\end{bmatrix} \tag{19}$$

$$\begin{bmatrix}\mathbf{a}_{walls}\\ \mathbf{a}_{Re}\end{bmatrix}^{\mathsf{T}}_{\Delta C_L} = \begin{bmatrix}
1.1212\times10^{-4} & -2.8344\times10^{-5}\\
-1.6426\times10^{-4} & 1.1331\times10^{-4}\\
-1.6608\times10^{-5} & -4.2924\times10^{-5}\\
5.0649\times10^{-5} & -4.4574\times10^{-5}\\
7.4308\times10^{-5} & -2.6913\times10^{-5}\\
-7.7355\times10^{-5} & 7.8725\times10^{-5}\\
-4.9256\times10^{-5} & -1.3211\times10^{-4}\\
9.2257\times10^{-5} & 7.7997\times10^{-5}\\
1.7150\times10^{-5} & -1.2983\times10^{-6}\\
-9.9590\times10^{-6} & -1.0661\times10^{-5}\\
-1.1154\times10^{-6} & -1.6138\times10^{-5}\\
-3.1665\times10^{-5} & 4.0307\times10^{-5}\\
-7.1714\times10^{-5} & -4.1655\times10^{-5}\\
1.3437\times10^{-4} & 1.1843\times10^{-4}\\
-9.4060\times10^{-5} & -1.1388\times10^{-4}\\
3.5148\times10^{-5} & 2.9737\times10^{-5}\\
-8.7036\times10^{-4} & 1.6193\times10^{-3}\\
1.9117\times10^{-3} & 3.6856\times10^{-3}\\
-5.0742\times10^{-1} & -3.8004\times10^{-2}
\end{bmatrix} \tag{20}$$

$$\begin{bmatrix} \mathbf{a}_{walls} \\ \mathbf{a}_{Re} \end{bmatrix}_{\Delta C_l}^{\mathsf{T}} = \begin{bmatrix} -1.6751\times10^{-7} & 1.2957\times10^{-5} \\ 1.2379\times10^{-5} & -1.0164\times10^{-5} \\ -1.0171\times10^{-5} & 1.1032\times10^{-5} \\ 1.0198\times10^{-6} & -1.5715\times10^{-5} \\ -2.2353\times10^{-6} & -7.0047\times10^{-6} \\ -2.2937\times10^{-5} & 1.0560\times10^{-5} \\ 1.9486\times10^{-5} & -3.6655\times10^{-6} \\ -1.3222\times10^{-5} & -2.5434\times10^{-6} \\ 1.2491\times10^{-5} & -5.3600\times10^{-6} \\ -4.8545\times10^{-6} & 2.1313\times10^{-5} \\ 5.3932\times10^{-6} & -3.9384\times10^{-5} \\ 1.5592\times10^{-5} & 3.4404\times10^{-5} \\ -4.8341\times10^{-6} & -1.0880\times10^{-5} \\ 3.3311\times10^{-6} & 1.3007\times10^{-5} \\ -6.3021\times10^{-6} & -6.5569\times10^{-6} \\ -4.9677\times10^{-6} & -1.9976\times10^{-6} \\ -1.9240\times10^{-4} & 6.0156\times10^{-4} \\ -2.3604\times10^{-5} & 6.8119\times10^{-4} \\ 5.7749\times10^{-3} & -8.2463\times10^{-3} \end{bmatrix} \tag{21}$$

$$\begin{bmatrix} \mathbf{a}_{walls} \\ \mathbf{a}_{Re} \end{bmatrix}_{\Delta C_m}^{\mathsf{T}} = \begin{bmatrix} -3.5100\times10^{-5} & 4.4081\times10^{-5} \\ 7.8022\times10^{-5} & -5.5329\times10^{-5} \\ -5.6094\times10^{-5} & -2.6173\times10^{-5} \\ 1.9988\times10^{-5} & 6.1350\times10^{-5} \\ -1.3035\times10^{-5} & 1.2699\times10^{-5} \\ 4.3247\times10^{-5} & -8.2808\times10^{-5} \\ -2.4010\times10^{-5} & 1.4458\times10^{-4} \\ -1.3295\times10^{-5} & -1.1447\times10^{-4} \\ -1.3908\times10^{-5} & -4.8546\times10^{-6} \\ 5.7084\times10^{-5} & 6.6724\times10^{-5} \\ -6.0817\times10^{-5} & -6.4589\times10^{-5} \\ 1.1389\times10^{-5} & 1.0945\times10^{-5} \\ 1.9254\times10^{-5} & 8.6979\times10^{-7} \\ -3.9691\times10^{-5} & -3.4959\times10^{-5} \\ -8.0756\times10^{-6} & 5.8617\times10^{-7} \\ 3.5043\times10^{-5} & 4.1350\times10^{-5} \\ 3.6975\times10^{-4} & 4.8822\times10^{-4} \\ 1.5753\times10^{-3} & -4.4335\times10^{-4} \\ -4.3793\times10^{-2} & -1.3800\times10^{-1} \end{bmatrix} \tag{22}$$

$$\begin{bmatrix} \mathbf{a}_{walls} \\ \mathbf{a}_{Re} \end{bmatrix}^{\mathsf{T}}_{\Delta C_n} = \begin{bmatrix} -6.3735 \times 10^{-6} & -1.0830 \times 10^{-7} \\ 2.5316 \times 10^{-6} & 2.4158 \times 10^{-6} \\ -3.6275 \times 10^{-6} & -1.6345 \times 10^{-5} \\ 2.8593 \times 10^{-6} & 1.2494 \times 10^{-5} \\ 7.6523 \times 10^{-6} & 9.6768 \times 10^{-7} \\ 5.2538 \times 10^{-7} & -8.7119 \times 10^{-6} \\ -6.3450 \times 10^{-6} & 3.5213 \times 10^{-5} \\ 9.6640 \times 10^{-6} & -1.8991 \times 10^{-5} \\ 7.3405 \times 10^{-7} & 2.8971 \times 10^{-6} \\ -6.1144 \times 10^{-6} & -7.0185 \times 10^{-6} \\ 1.3733 \times 10^{-5} & -6.8519 \times 10^{-6} \\ -1.7513 \times 10^{-5} & -1.3434 \times 10^{-6} \\ -1.6142 \times 10^{-8} & -5.4068 \times 10^{-7} \\ -7.3185 \times 10^{-6} & 2.3022 \times 10^{-7} \\ 1.1003 \times 10^{-5} & 4.5082 \times 10^{-6} \\ -1.3942 \times 10^{-6} & 1.1853 \times 10^{-6} \\ 7.4706 \times 10^{-5} & -1.7317 \times 10^{-6} \\ -1.2505 \times 10^{-4} & -1.2747 \times 10^{-4} \\ 1.2746 \times 10^{-2} & 3.3042 \times 10^{-3} \end{bmatrix} \tag{23}$$

F. Pressure Coefficient Contours and Streamlines

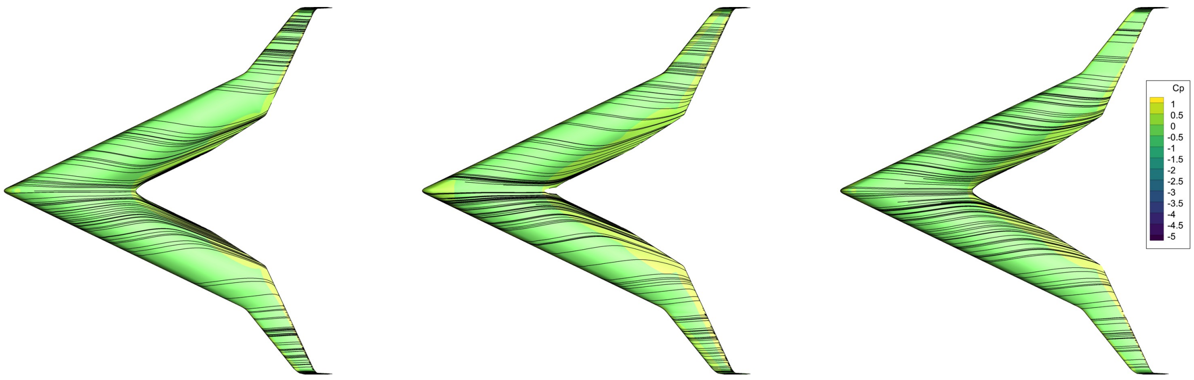

(a) Scaled **(b) Wind tunnel** **(c) Full-scale**

Figure 43. Flying V pressure coefficient contours and surface streamlines $(\alpha = 0°, \beta = 0°)$

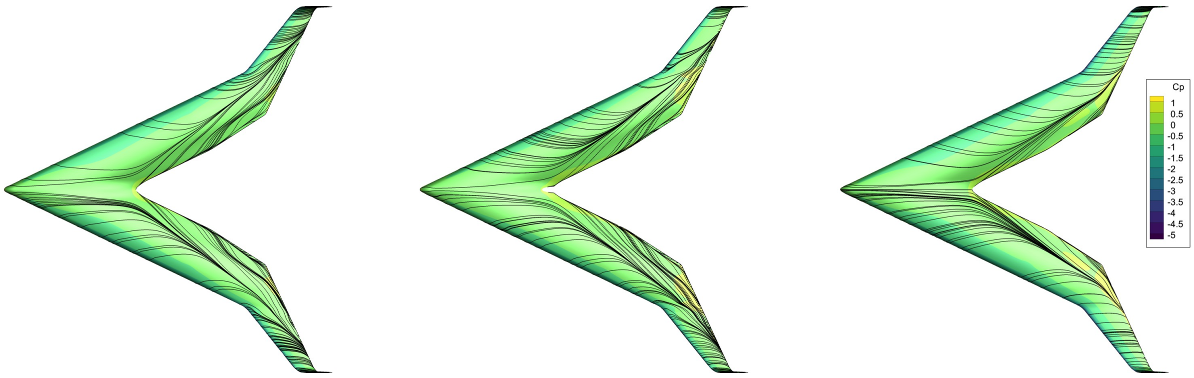

(a) Scaled **(b) Wind tunnel** **(c) Full-scale**

Figure 44. Flying V pressure coefficient contours and surface streamlines $(\alpha = 10.66°, \beta = 0°)$

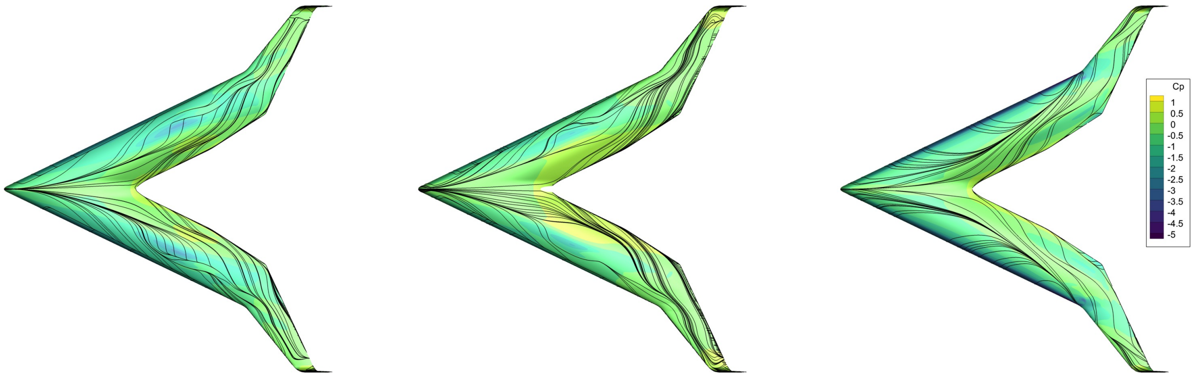

(a) Scaled **(b) Wind tunnel** **(c) Full-scale**

Figure 45. Flying V pressure coefficient contours and surface streamlines $(\alpha = 21.33°, \beta = 0°)$

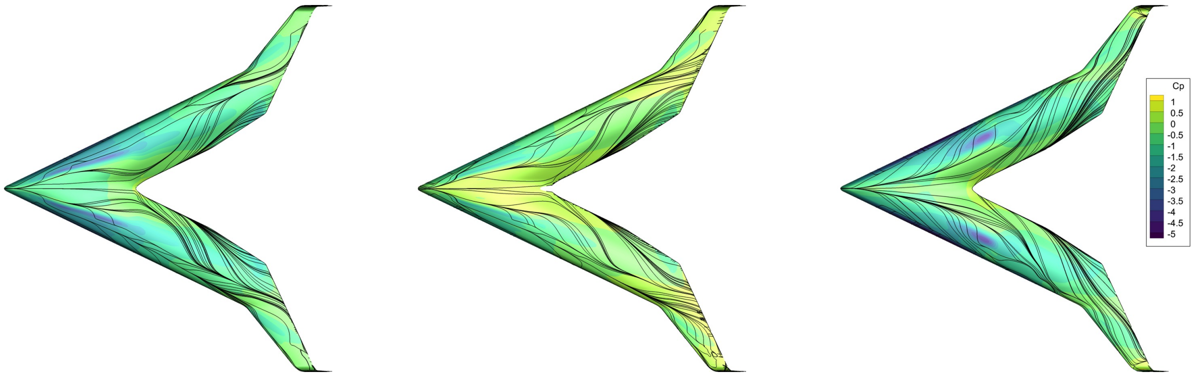

(a) Scaled **(b) Wind tunnel** **(c) Full-scale**

Figure 46. Flying V pressure coefficient contours and surface streamlines $(\alpha = 32°, \beta = 0°)$

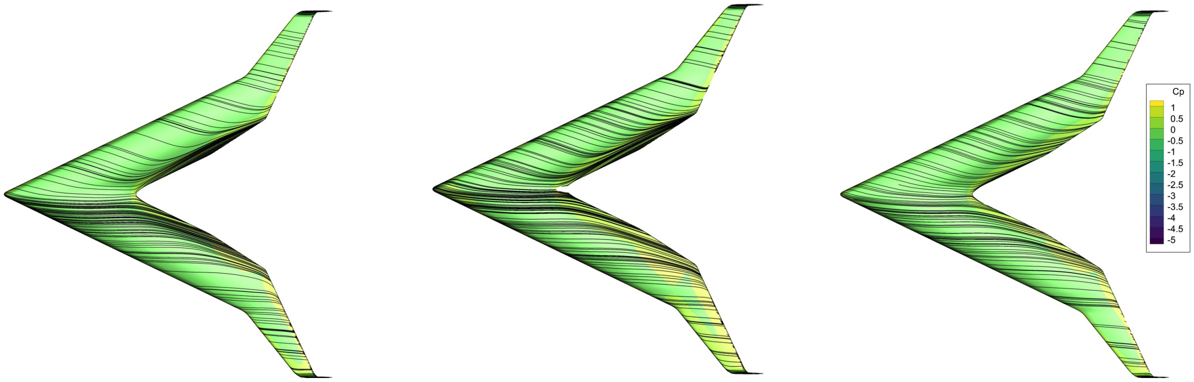

(a) Scaled **(b) Wind tunnel** **(c) Full-scale**

Figure 47. Flying V pressure coefficient contours and surface streamlines $(\alpha = 0°, \beta = 8.33°)$

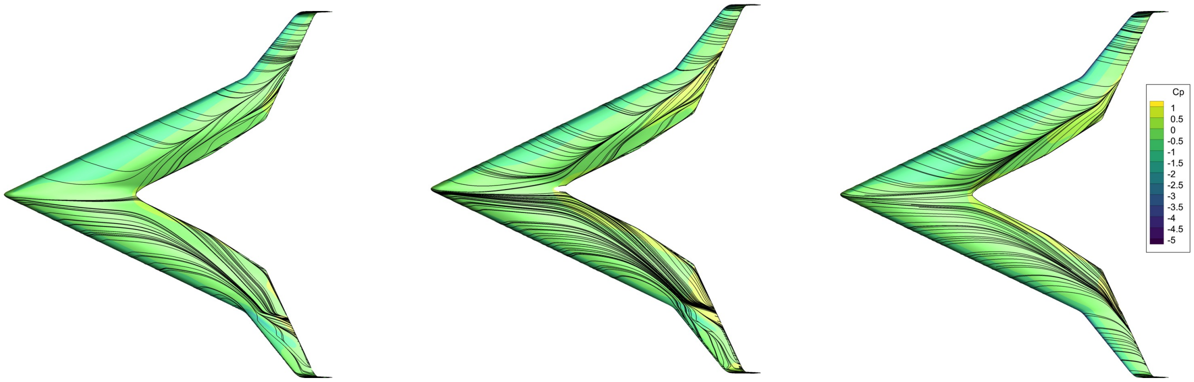

(a) Scaled **(b) Wind tunnel** **(c) Full-scale**

Figure 48. Flying V pressure coefficient contours and surface streamlines $(\alpha = 10.66°, \beta = 8.33°)$

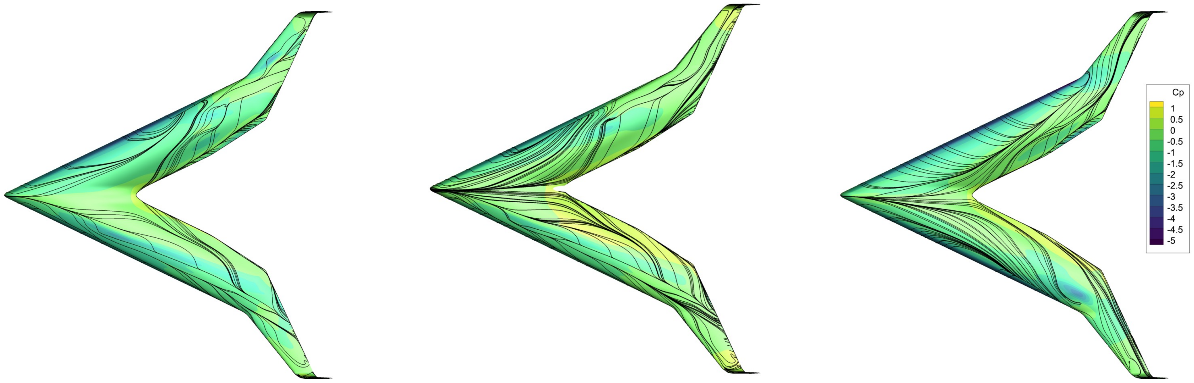

(a) Scaled **(b) Wind tunnel** **(c) Full-scale**

Figure 49. Flying V pressure coefficient contours and surface streamlines ($\alpha = 21.33°, \beta = 8.33°$)

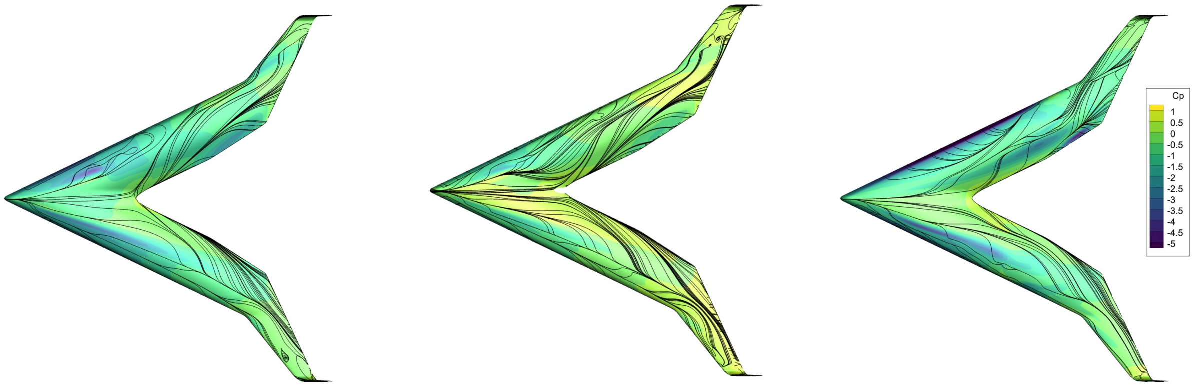

(a) Scaled **(b) Wind tunnel** **(c) Full-scale**

Figure 50. Flying V pressure coefficient contours and surface streamlines ($\alpha = 32°, \beta = 8.33°$)

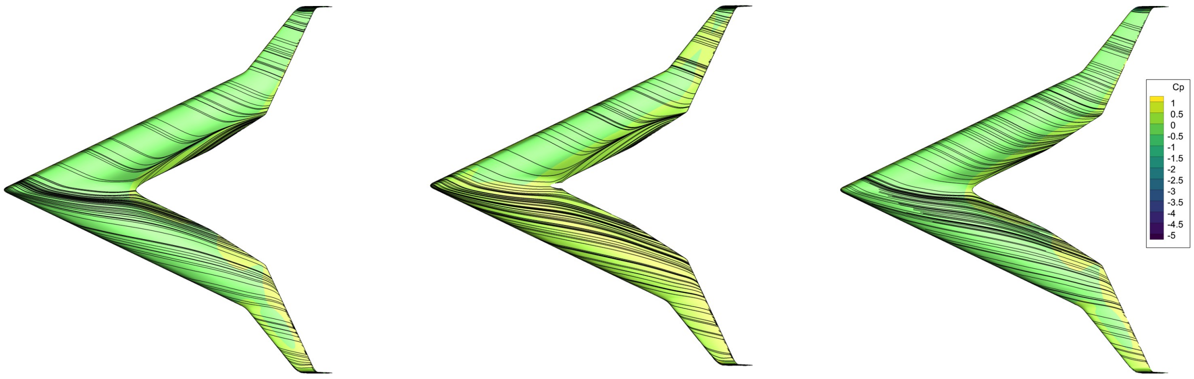

(a) Scaled **(b) Wind tunnel** **(c) Full-scale**

Figure 51. Flying V pressure coefficient contours and surface streamlines ($\alpha = 0°, \beta = 16.66°$)

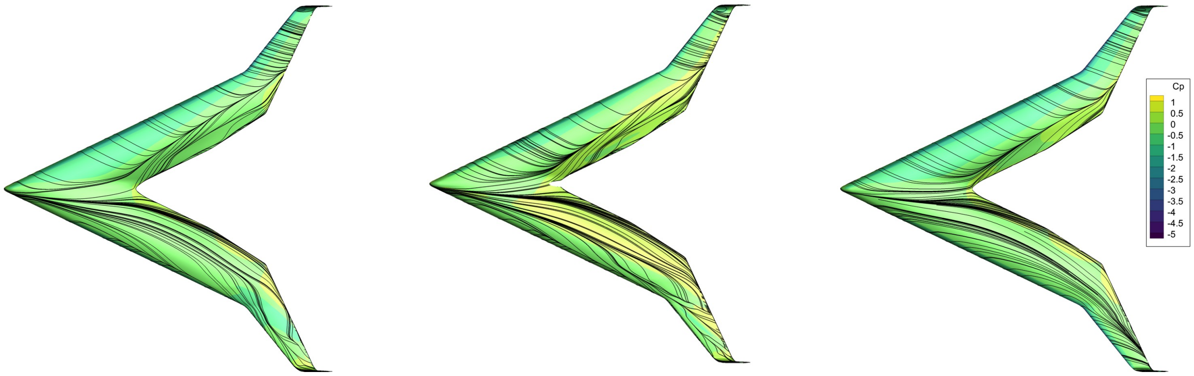

(a) Scaled **(b) Wind tunnel** **(c) Full-scale**

Figure 52. Flying V pressure coefficient contours and surface streamlines ($\alpha = 10.66°, \beta = 16.66°$)

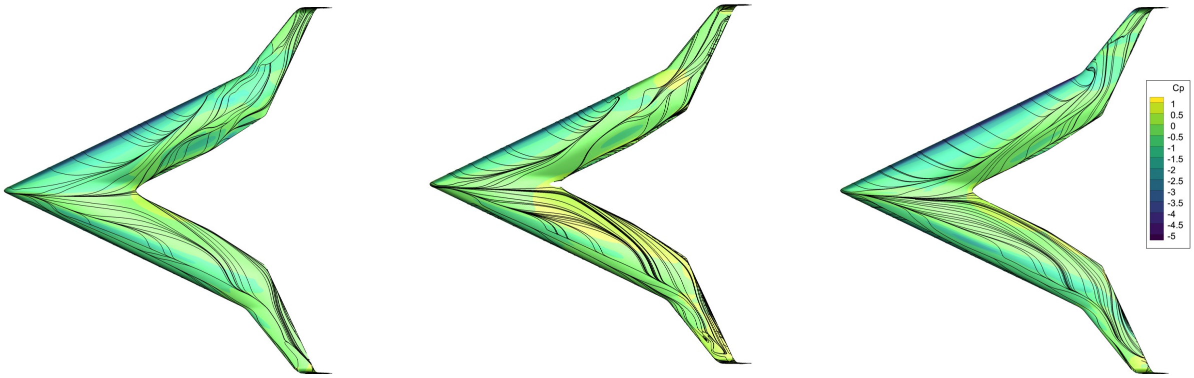

(a) Scaled **(b) Wind tunnel** **(c) Full-scale**

Figure 53. Flying V pressure coefficient contours and surface streamlines ($\alpha = 21.33°, \beta = 16.66°$)

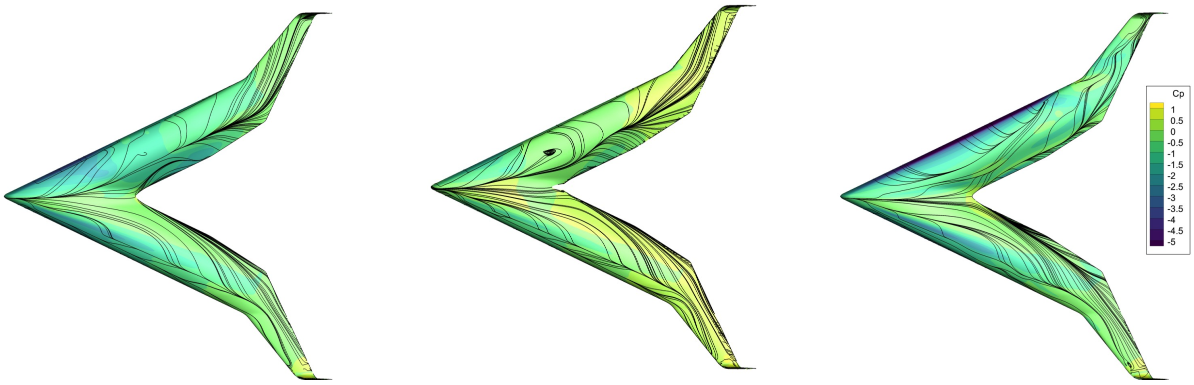

(a) Scaled **(b) Wind tunnel** **(c) Full-scale**

Figure 54. Flying V pressure coefficient contours and surface streamlines ($\alpha = 32°, \beta = 16.66°$)

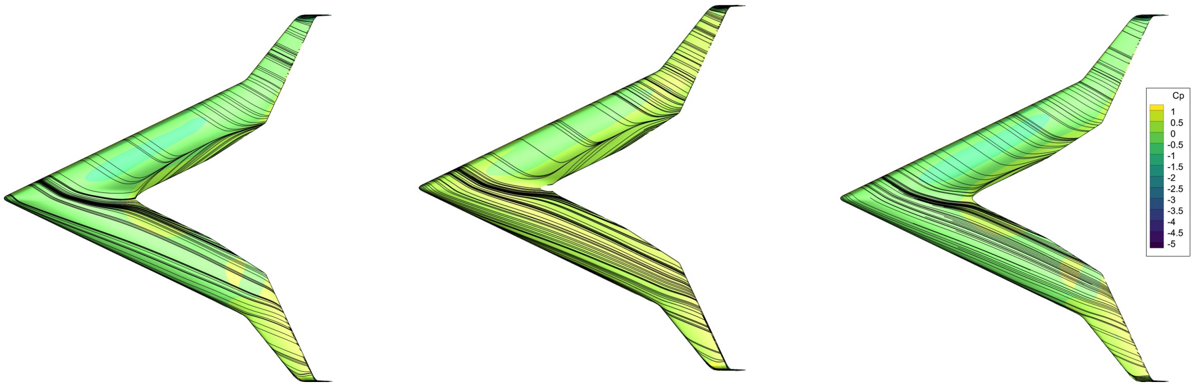

(a) Scaled **(b) Wind tunnel** **(c) Full-scale**

Figure 55. Flying V pressure coefficient contours and surface streamlines $(\alpha = 0°, \beta = 25°)$

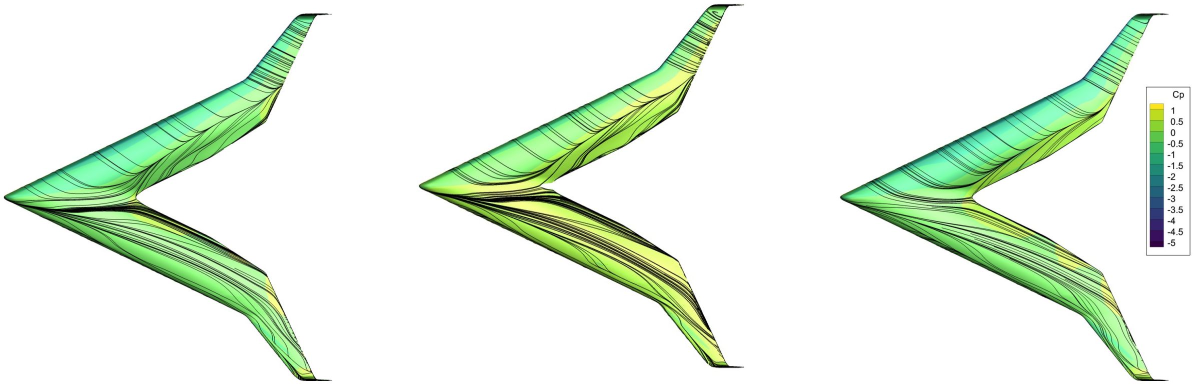

(a) Scaled **(b) Wind tunnel** **(c) Full-scale**

Figure 56. Flying V pressure coefficient contours and surface streamlines $(\alpha = 10.66°, \beta = 25°)$

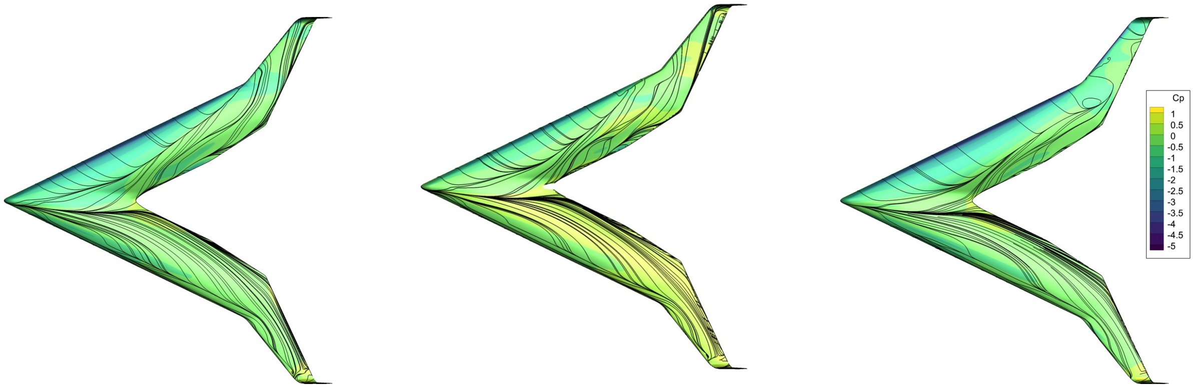

(a) Scaled **(b) Wind tunnel** **(c) Full-scale**

Figure 57. Flying V pressure coefficient contours and surface streamlines $(\alpha = 21.33°, \beta = 25°)$

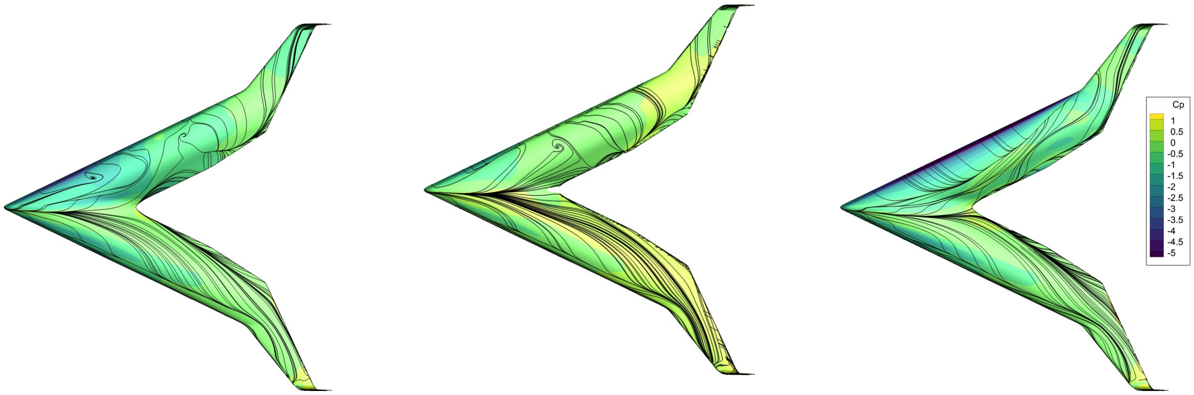

(a) Scaled **(b) Wind tunnel** **(c) Full-scale**

Figure 58. Flying V pressure coefficient contours and surface streamlines ($\alpha = 32°, \beta = 25°$)

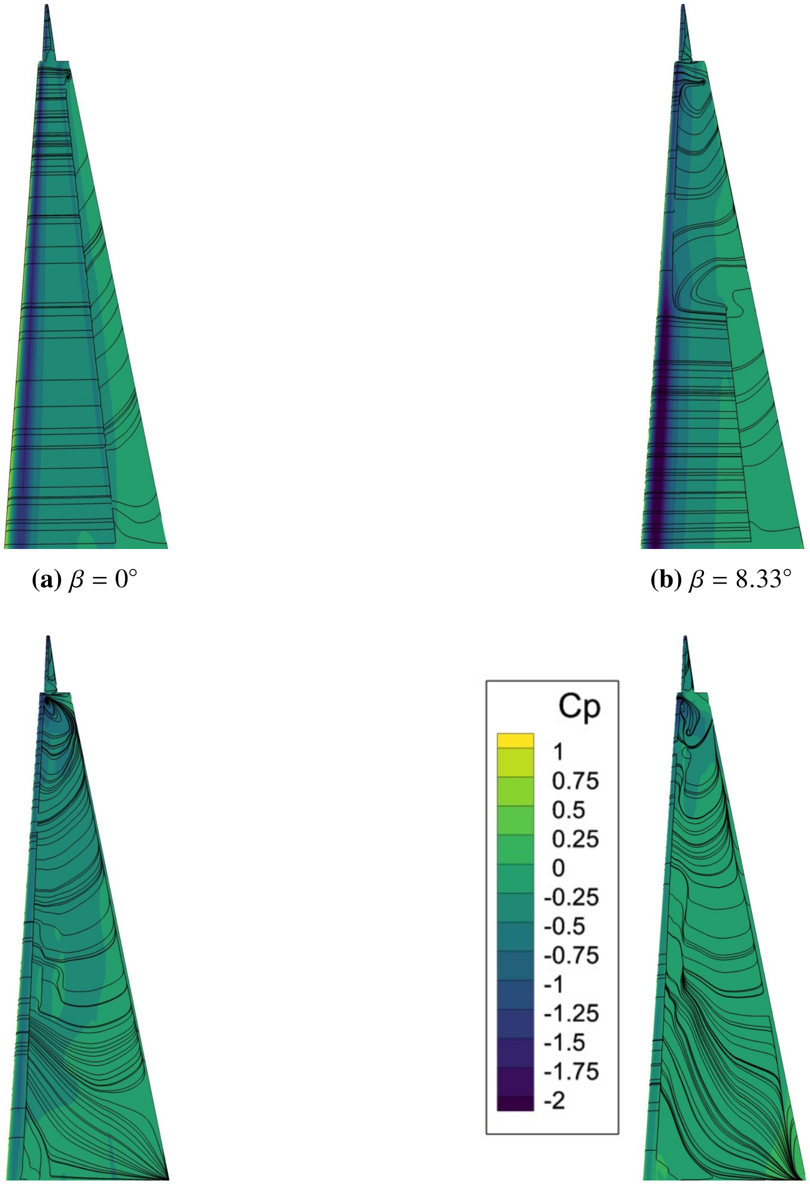

(a) β = 0°

(b) β = 8.33°

(c) β = 16.66°

(d) β = 25°

Figure 59. LTT strut pressure coefficient contours and surface streamlines

G. Pressure Loss Slices

(a) Scaled **(b) Wind tunnel** **(c) Full-scale**

Figure 60. Flying V total pressure loss at slices of constant x $(\alpha = 0°, \beta = 0°)$

(a) Scaled **(b) Wind tunnel** **(c) Full-scale**

Figure 61. Flying V total pressure loss at slices of constant x $(\alpha = 10.66°, \beta = 0°)$

(a) Scaled **(b) Wind tunnel** **(c) Full-scale**

Figure 62. Flying V total pressure loss at slices of constant x $(\alpha = 21.33°, \beta = 0°)$

(a) Scaled **(b) Wind tunnel** **(c) Full-scale**

Figure 63. Flying V total pressure loss at slices of constant x $(\alpha = 32°, \beta = 0°)$

(a) Scaled **(b) Wind tunnel** **(c) Full-scale**

Figure 64. Flying V total pressure loss at slices of constant x $(\alpha = 0°, \beta = 8.33°)$

(a) Scaled **(b) Wind tunnel** **(c) Full-scale**

Figure 65. Flying V total pressure loss at slices of constant x $(\alpha = 10.66°, \beta = 8.33°)$

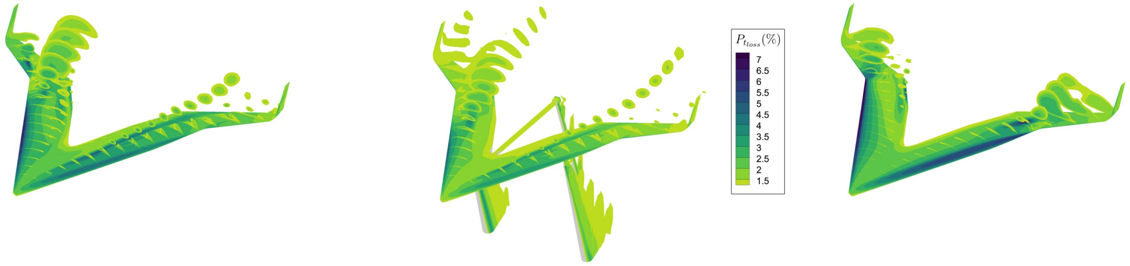

(a) Scaled **(b) Wind tunnel** **(c) Full-scale**

Figure 66. Flying V total pressure loss at slices of constant x $(\alpha = 21.33°, \beta = 8.33°)$

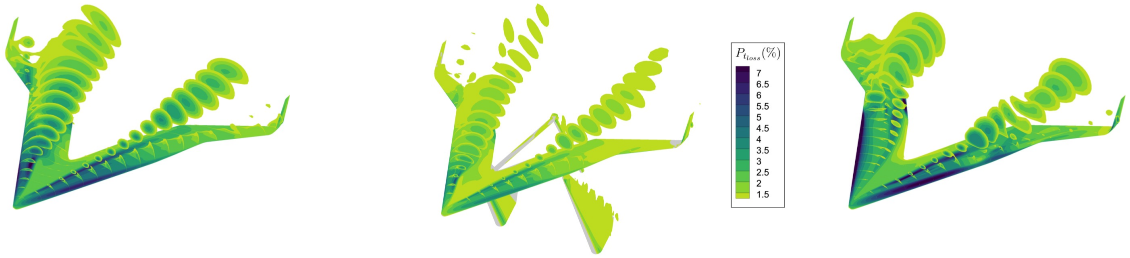

(a) Scaled **(b) Wind tunnel** **(c) Full-scale**

Figure 67. Flying V total pressure loss at slices of constant x $(\alpha = 32°, \beta = 8.33°)$

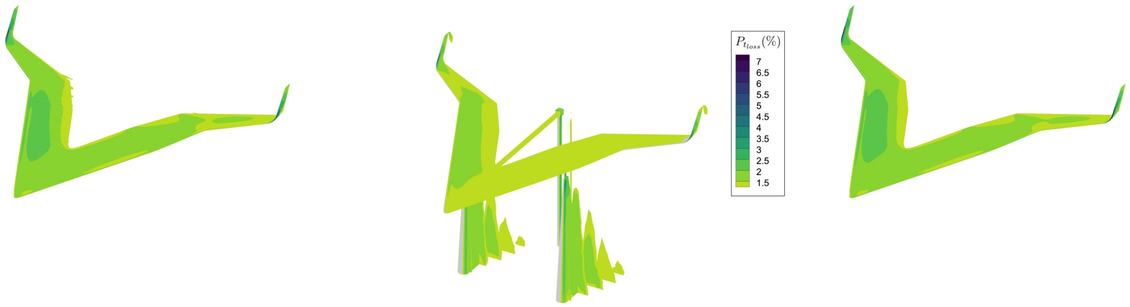

(a) Scaled **(b) Wind tunnel** **(c) Full-scale**

Figure 68. Flying V total pressure loss at slices of constant x $(\alpha = 0°, \beta = 16.66°)$

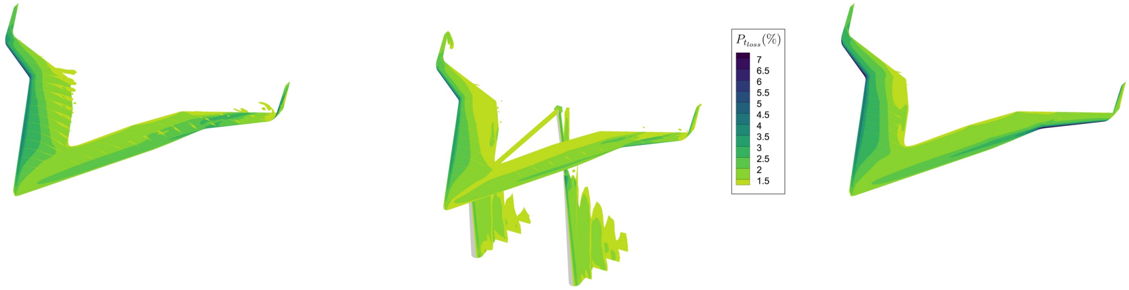

(a) Scaled **(b) Wind tunnel** **(c) Full-scale**

Figure 69. Flying V total pressure loss at slices of constant x $(\alpha = 10.66°, \beta = 16.66°)$

(a) Scaled **(b) Wind tunnel** **(c) Full-scale**

Figure 70. Flying V total pressure loss at slices of constant x $(\alpha = 21.33°, \beta = 16.66°)$

(a) Scaled **(b) Wind tunnel** **(c) Full-scale**

Figure 71. Flying V total pressure loss at slices of constant x $(\alpha = 32°, \beta = 16.66°)$

(a) Scaled **(b) Wind tunnel** **(c) Full-scale**

Figure 72. Flying V total pressure loss at slices of constant x $(\alpha = 0°, \beta = 25°)$

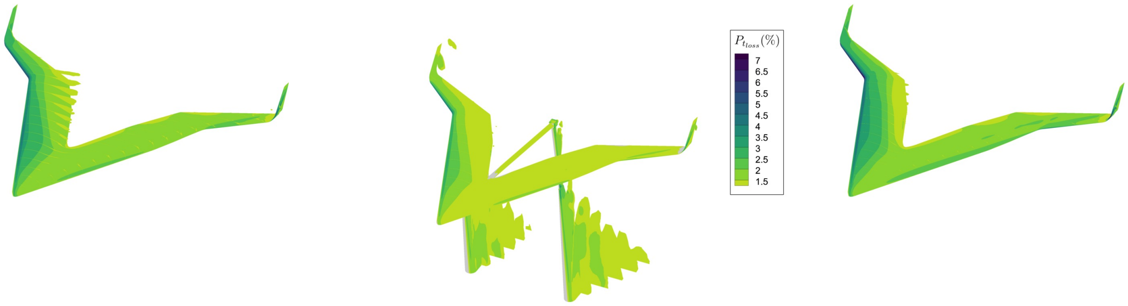

(a) Scaled **(b) Wind tunnel** **(c) Full-scale**

Figure 73. Flying V total pressure loss at slices of constant x $(\alpha = 10.66°, \beta = 25°)$

(a) Scaled **(b) Wind tunnel** **(c) Full-scale**

Figure 74. Flying V total pressure loss at slices of constant x $(\alpha = 21.33°, \beta = 25°)$

(a) Scaled **(b) Wind tunnel** **(c) Full-scale**

Figure 75. Flying V total pressure loss at slices of constant x ($\alpha = 32°, \beta = 25°$)

(a) β = 0° **(b)** β = 8.33°

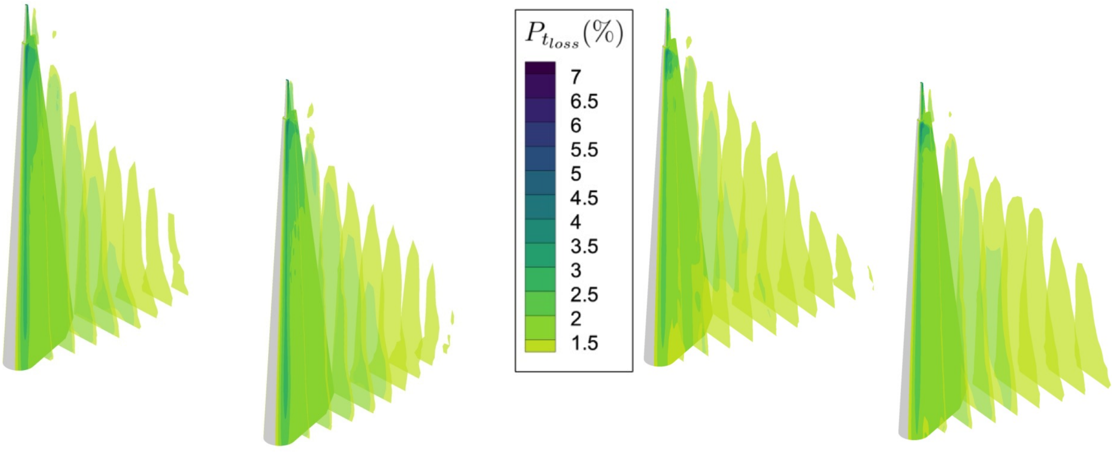

(c) β = 16.66° **(d)** β = 25°

Figure 76. LTT strut total pressure loss at slices of constant x

H. Dimensionless Wall Distance Contours

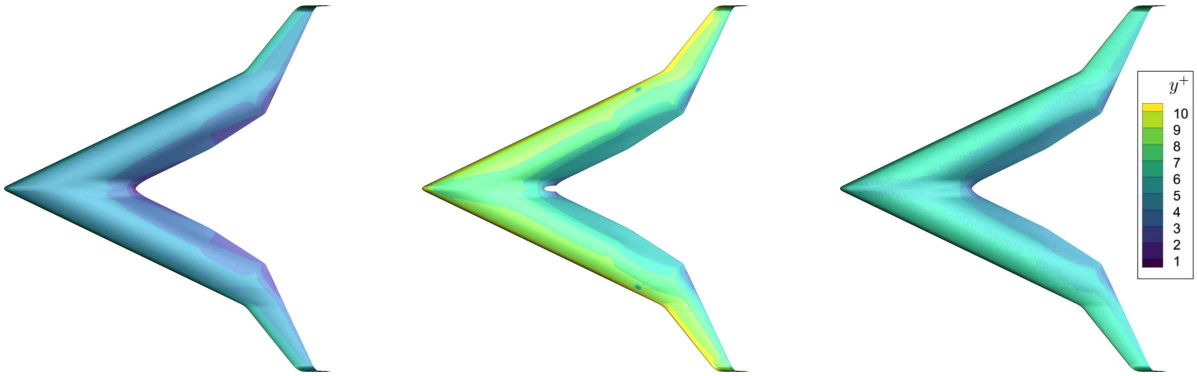

(a) Scaled **(b) Wind tunnel** **(c) Full-scale**

Figure 77. Flying V y^+ value over surface ($\alpha = 0°, \beta = 0°$)

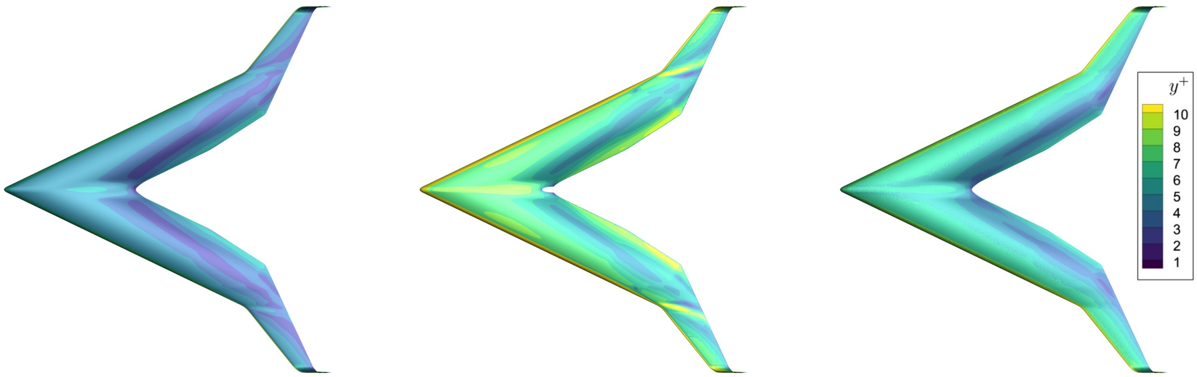

(a) Scaled **(b) Wind tunnel** **(c) Full-scale**

Figure 78. Flying V y^+ value over surface ($\alpha = 10.66°, \beta = 0°$)

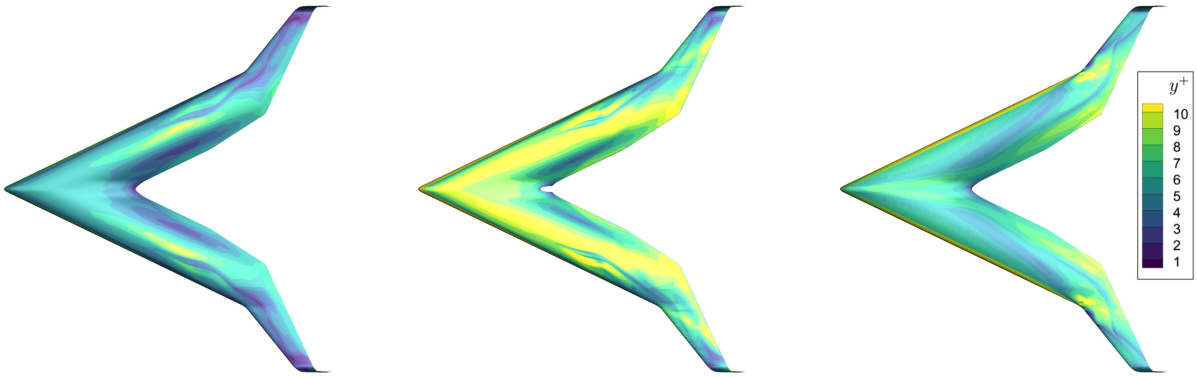

(a) Scaled **(b) Wind tunnel** **(c) Full-scale**

Figure 79. Flying V y^+ value over surface ($\alpha = 21.33°, \beta = 0°$)

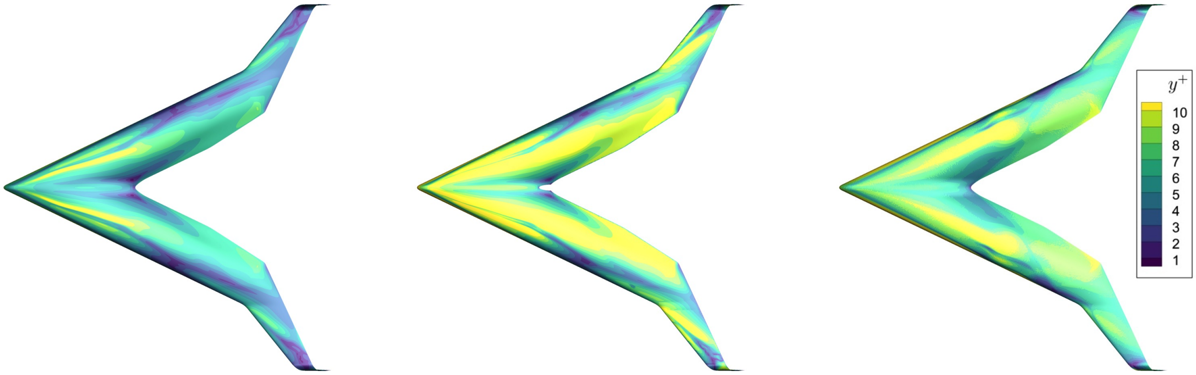

(a) Scaled **(b) Wind tunnel** **(c) Full-scale**

Figure 80. Flying V y^+ value over surface $(\alpha = 32°, \beta = 0°)$

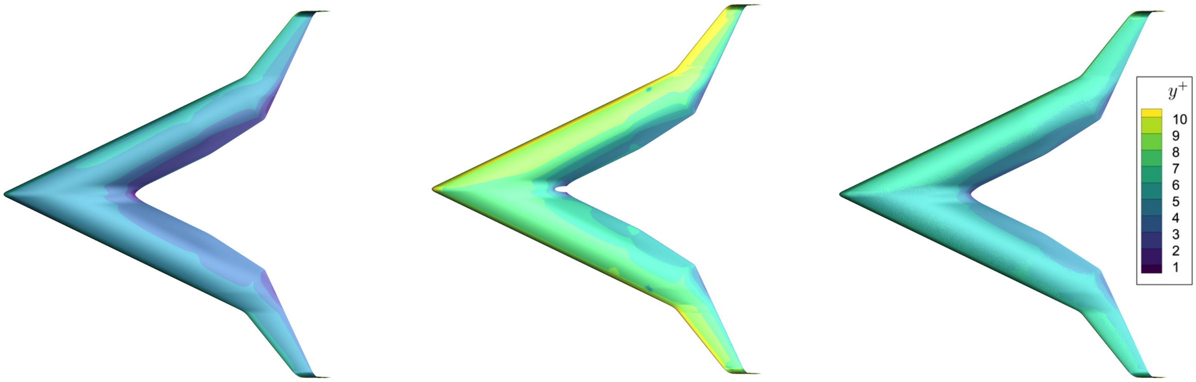

(a) Scaled **(b) Wind tunnel** **(c) Full-scale**

Figure 81. Flying V y^+ value over surface $(\alpha = 0°, \beta = 8.33°)$

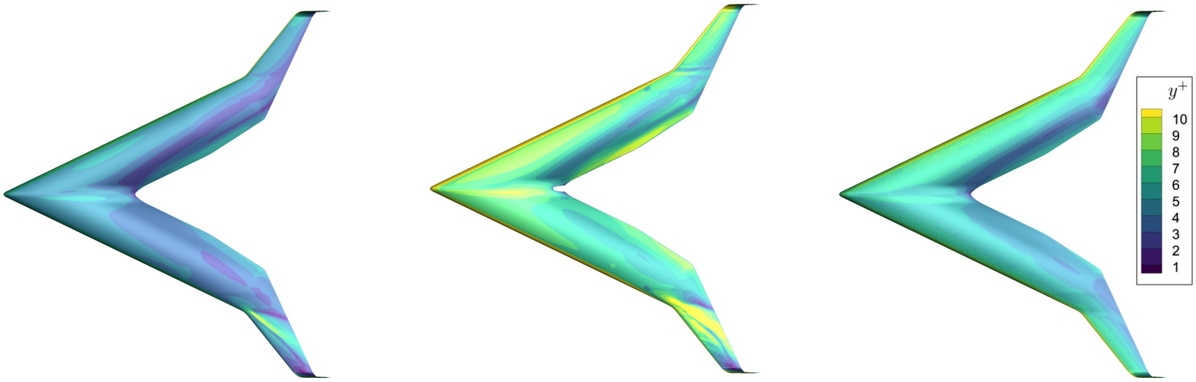

(a) Scaled **(b) Wind tunnel** **(c) Full-scale**

Figure 82. Flying V y^+ value over surface $(\alpha = 10.66°, \beta = 8.33°)$

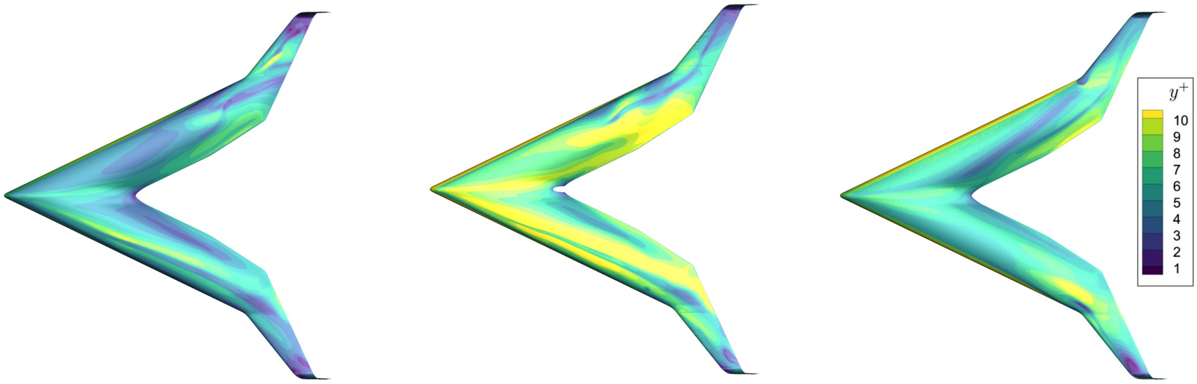

(a) Scaled **(b) Wind tunnel** **(c) Full-scale**

Figure 83. Flying V y^+ value over surface ($\alpha = 21.33°, \beta = 8.33°$)

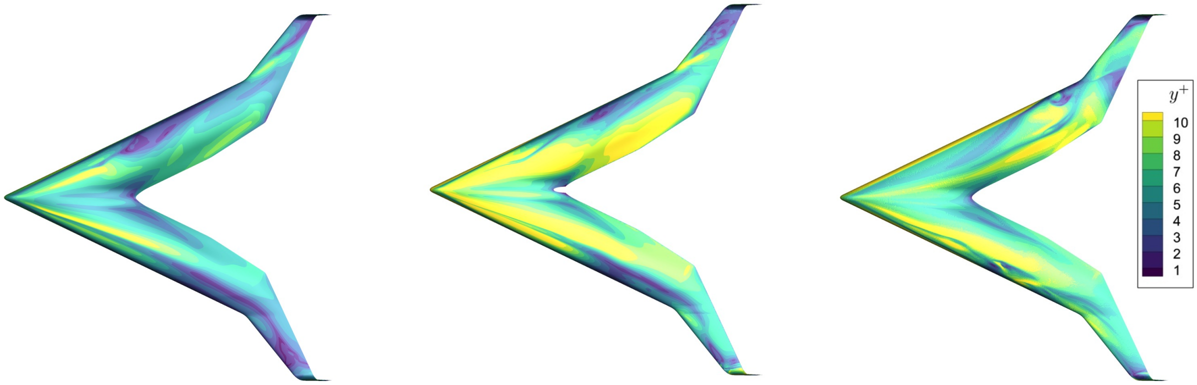

(a) Scaled **(b) Wind tunnel** **(c) Full-scale**

Figure 84. Flying V y^+ value over surface ($\alpha = 32°, \beta = 8.33°$)

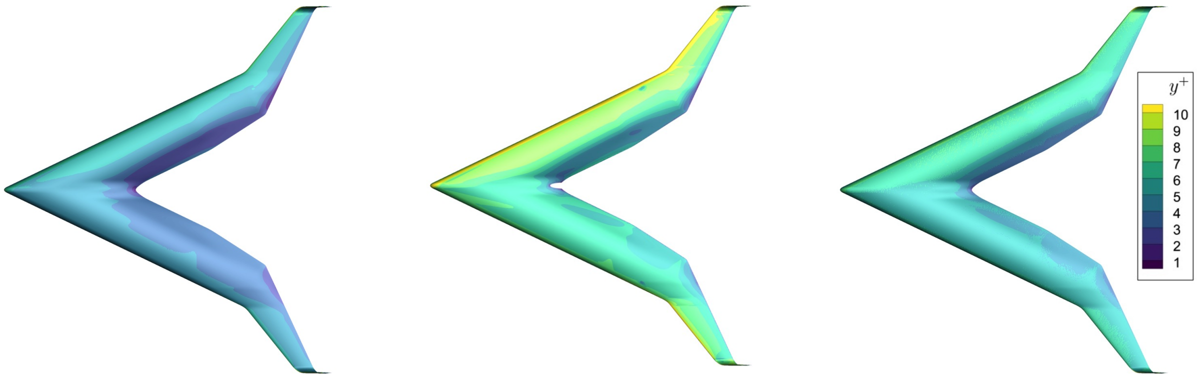

(a) Scaled **(b) Wind tunnel** **(c) Full-scale**

Figure 85. Flying V y^+ value over surface ($\alpha = 0°, \beta = 16.66°$)

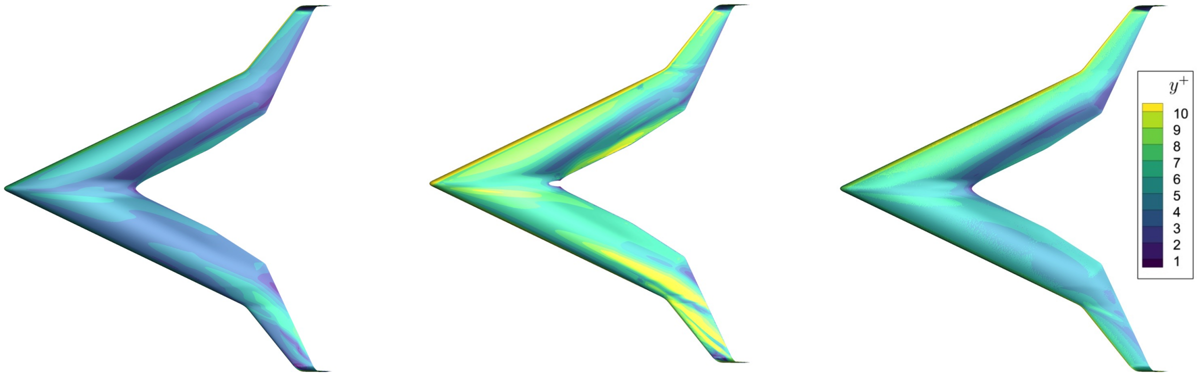

(a) Scaled **(b) Wind tunnel** **(c) Full-scale**

Figure 86. Flying V y^+ value over surface ($\alpha = 10.66°, \beta = 16.66°$)

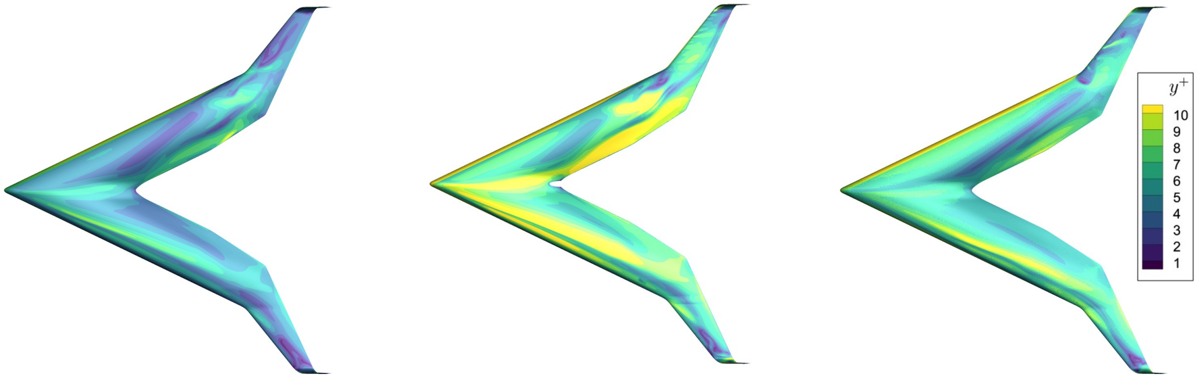

(a) Scaled **(b) Wind tunnel** **(c) Full-scale**

Figure 87. Flying V y^+ value over surface ($\alpha = 21.33°, \beta = 16.66°$)

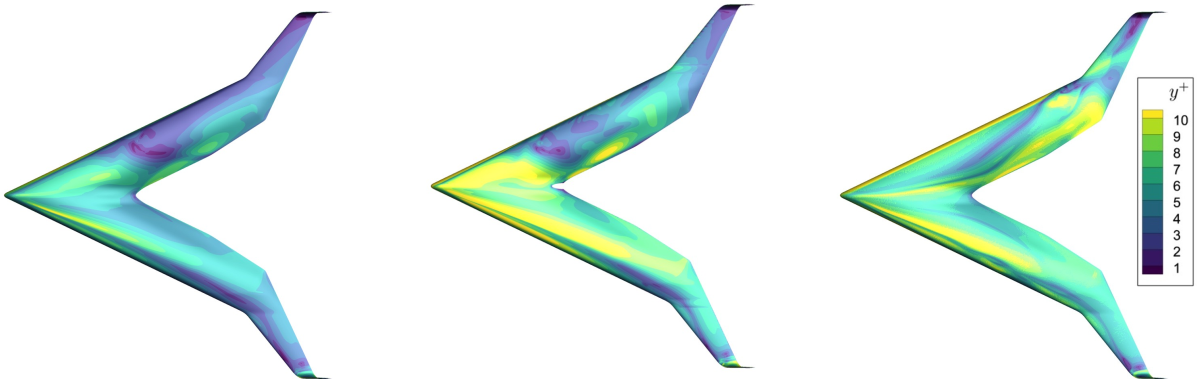

(a) Scaled **(b) Wind tunnel** **(c) Full-scale**

Figure 88. Flying V y^+ value over surface ($\alpha = 32°, \beta = 16.66°$)

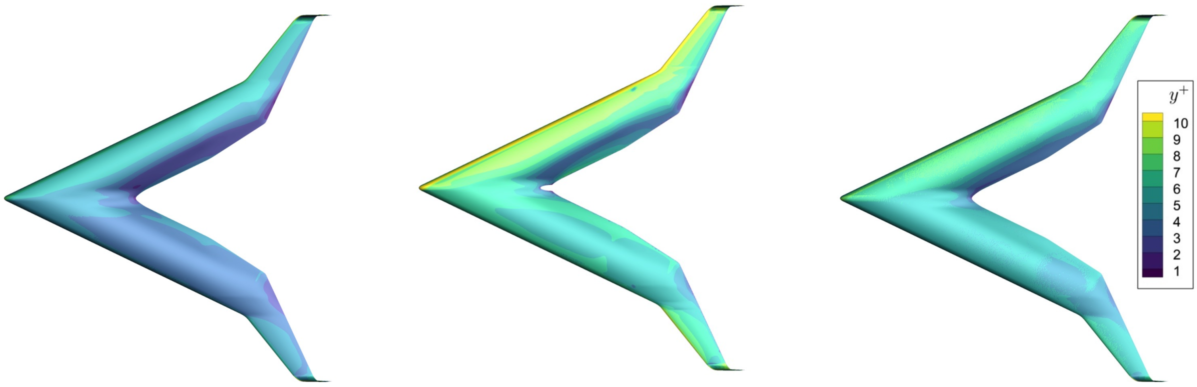

(a) Scaled **(b) Wind tunnel** **(c) Full-scale**

Figure 89. Flying V y^+ value over surface ($\alpha = 0°, \beta = 25°$)

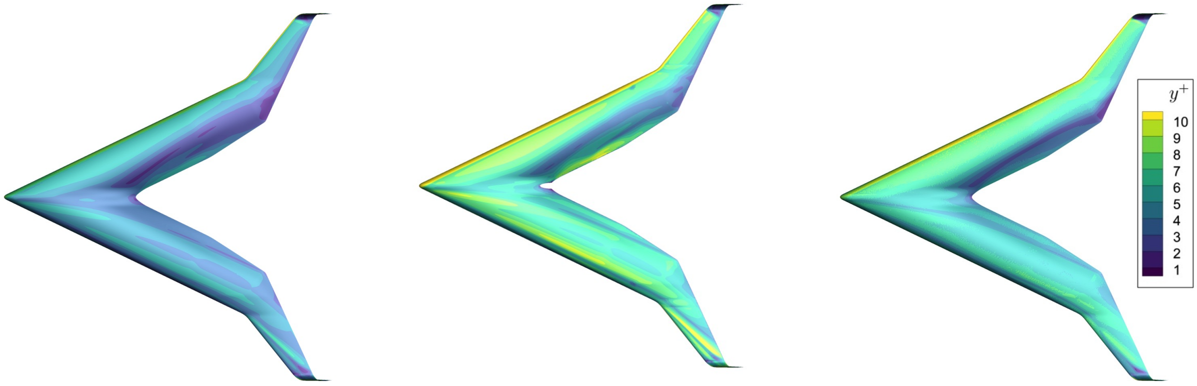

(a) Scaled **(b) Wind tunnel** **(c) Full-scale**

Figure 90. Flying V y^+ value over surface ($\alpha = 10.66°, \beta = 25°$)

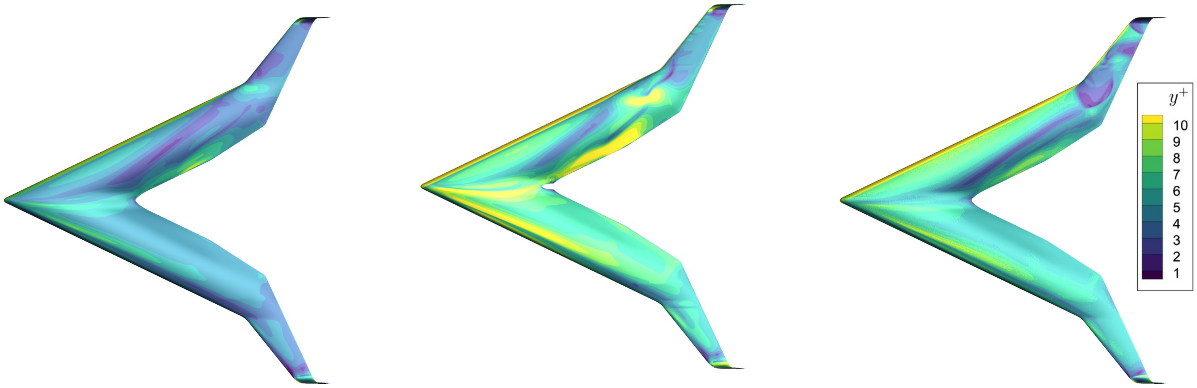

(a) Scaled **(b) Wind tunnel** **(c) Full-scale**

Figure 91. Flying V y^+ value over surface ($\alpha = 21.33°, \beta = 25°$)

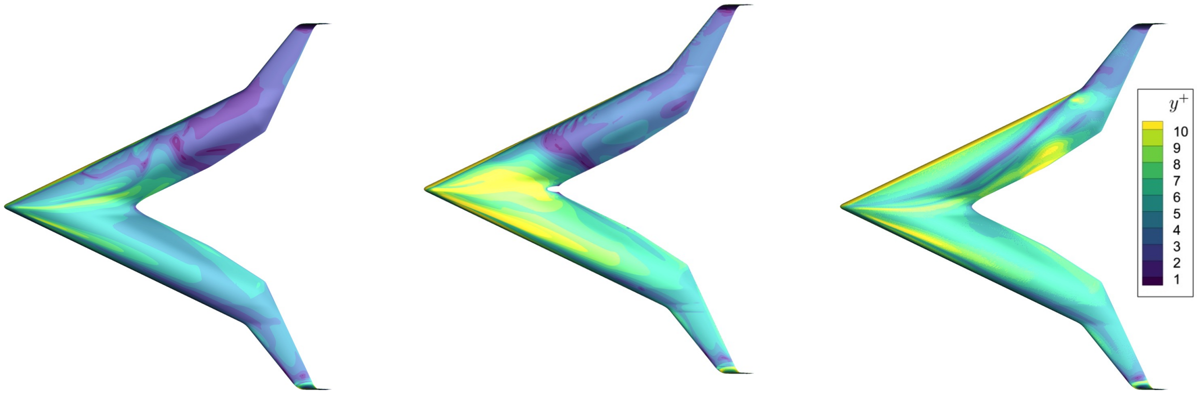

(a) Scaled **(b) Wind tunnel** **(c) Full-scale**

Figure 92. Flying V y^+ value over surface ($\alpha = 32°, \beta = 25°$)

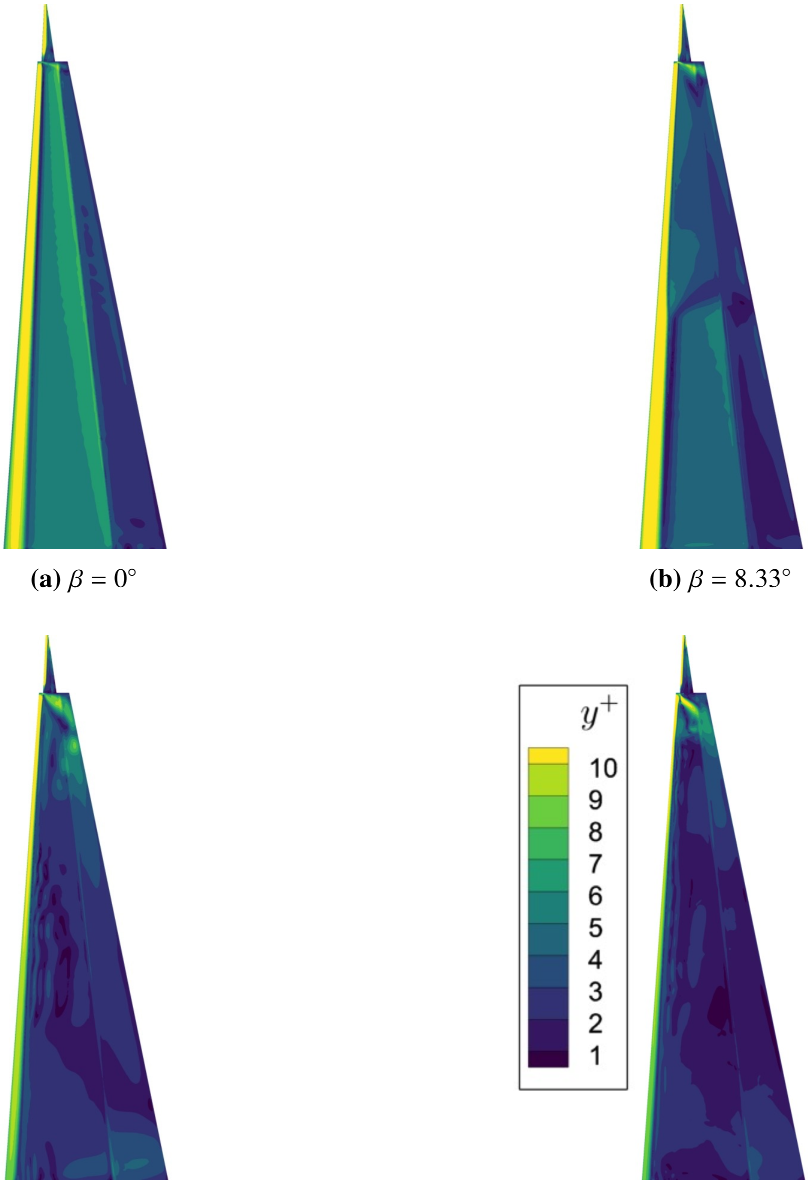

(a) β = 0°

(b) β = 8.33°

(c) β = 16.66°

(d) β = 25°

Figure 93. LTT strut y^+ value over surface

I. Interpolation Validation

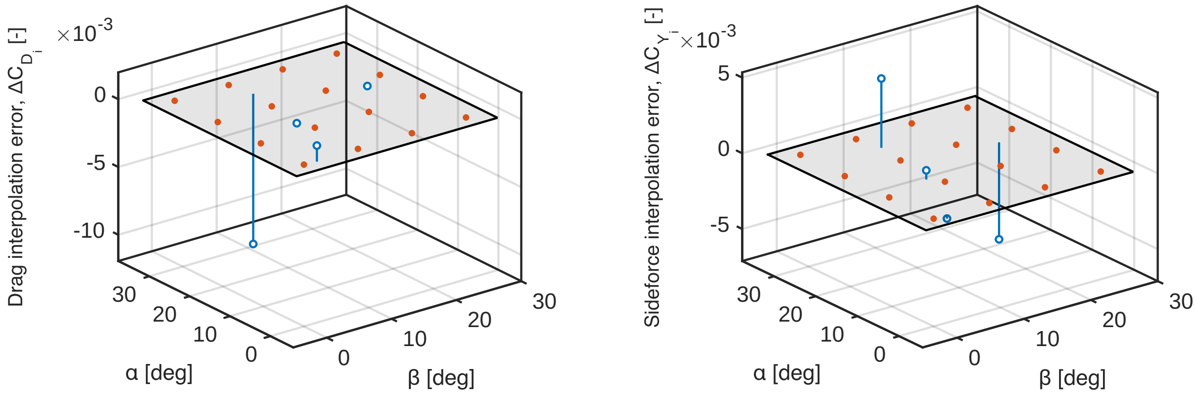

(a) Drag

(b) Sideforce

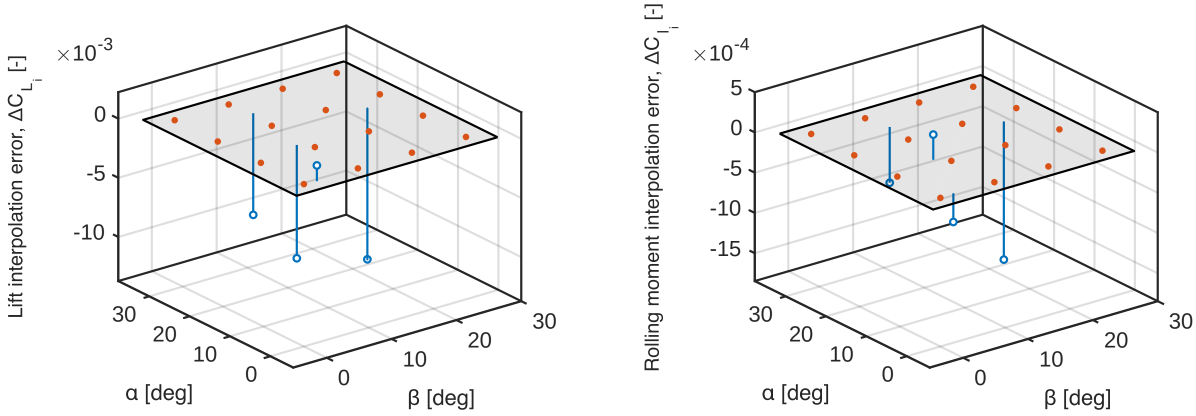

(c) Lift

(d) Rolling moment

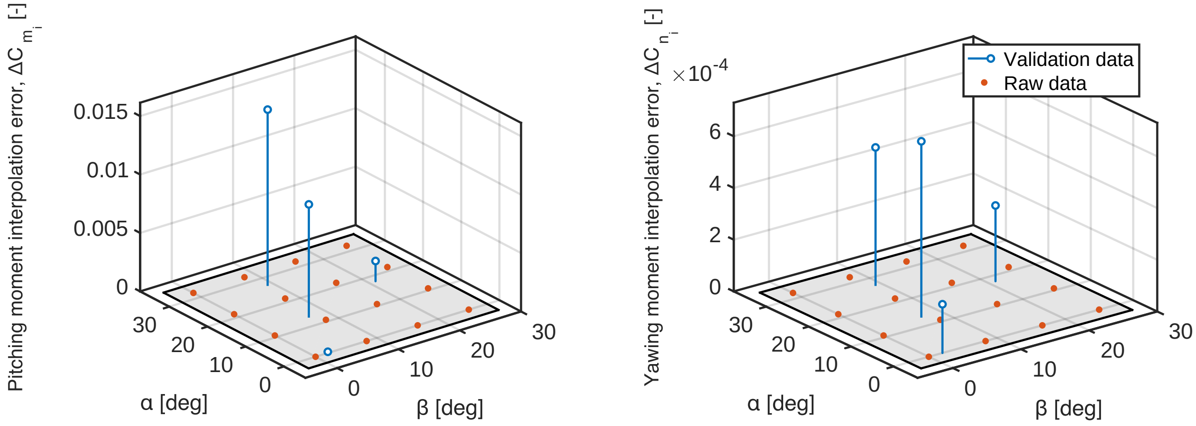

(e) Pitching moment

(f) Yawing moment

Figure 94. Interpolation errors of scaled Flying V interpolation validation runs

J. Residuals

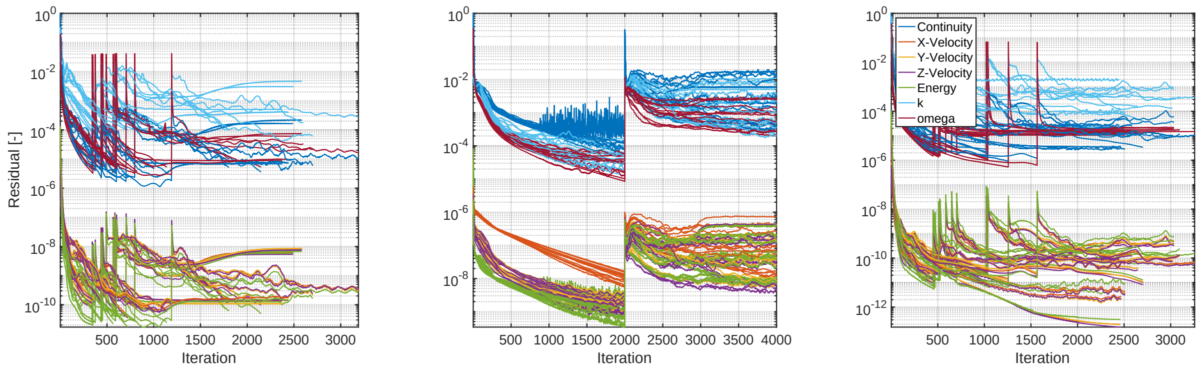

(a) Scaled **(b) Wind tunnel** **(c) Full-scale**

Figure 95. Convergence of Flying V simulation residuals

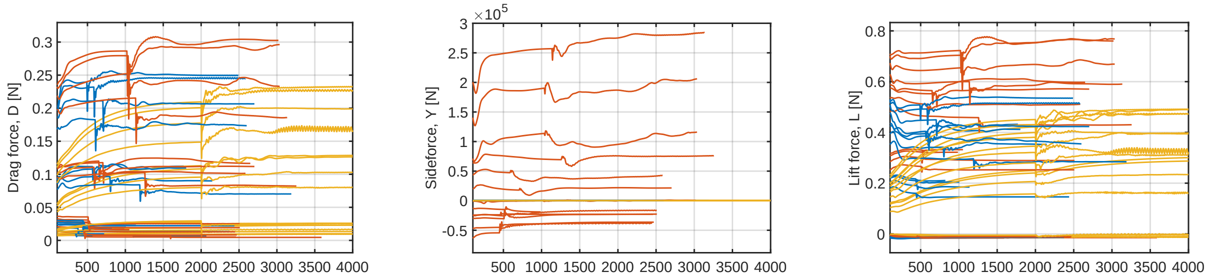

(a) Drag - total **(b) Sideforce - total** **(c) Lift - total**

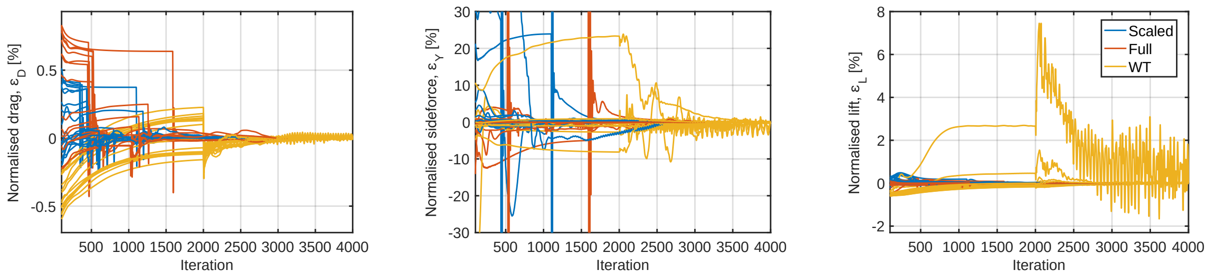

(d) Drag - normalised **(e) Sideforce - normalised** **(f) Lift - normalised**

Figure 96. Convergence of Flying V body forces

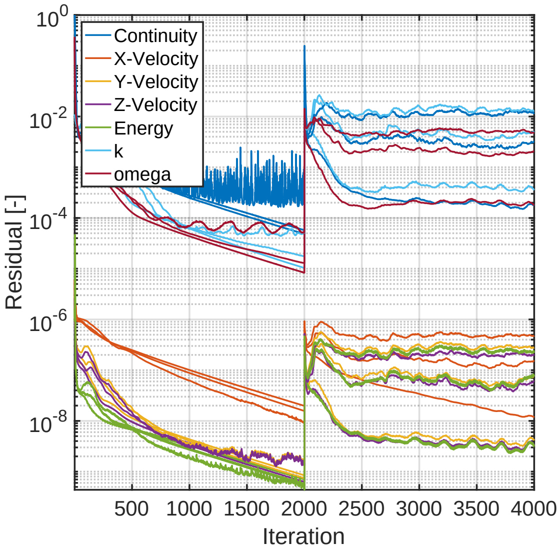

Figure 97. Convergence of LTT strut simulation residuals

K. Combined Wind Tunnel Corrections

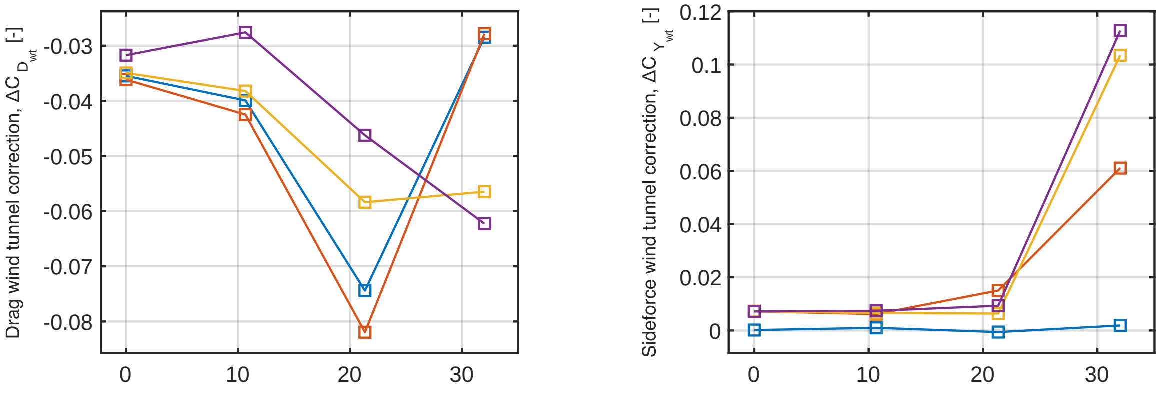

(a) Drag **(b) Sideforce**

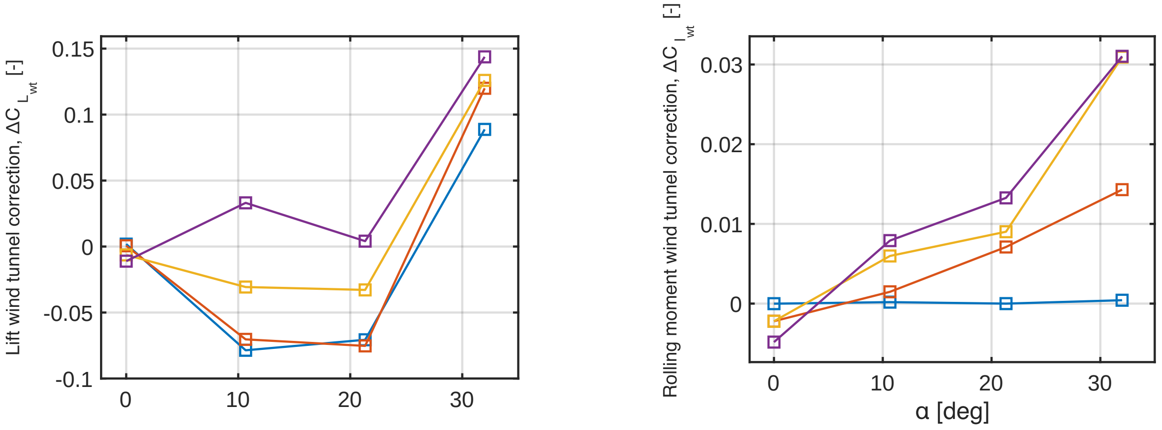

(c) Lift **(d) Rolling moment**

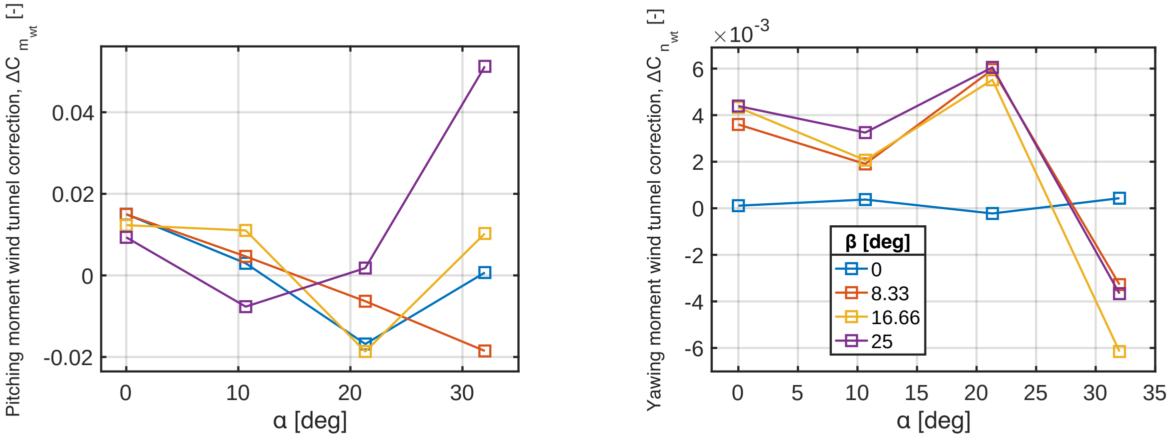

(e) Pitching moment **(f) Yawing moment**

Figure 98. Deltas between wind tunnel and full-scale simulation data